

# Modelling and Experimental Investigation of Strain Localization in Discontinuous Plastic Flow at Cryogenic Temperatures

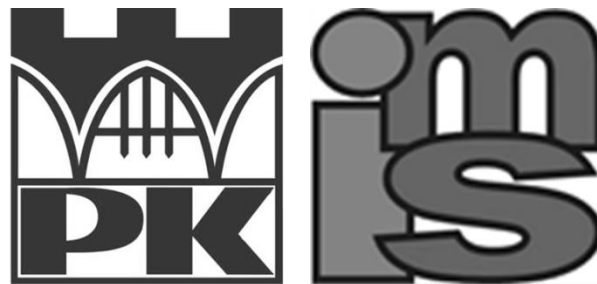
Modelowanie i Badanie Lokalizacji Odkształceń w Nieciągłym  
Płynięciu Plastycznym w Kriogenicznym Zakresie Temperatury

Doctoral Thesis

**mgr inż. Jakub Tabin**

Supervisor:

prof. dr hab. inż. Błażej Skoczeń



Institute of Applied Mechanics  
Cracow University of Technology  
av. John Paul II 37, 31-864 Cracow

Cracow 2017

# Acknowledgements

First and foremost, I would like to express my gratitude to my doctoral promoter, Professor Błażej Skoczeń, for his constructive support, experience, and the time devoted to me while preparing this Thesis. I am grateful for his faith in me and for inspiring me to achieve the scientific objectives.

My thanks also go to Michał Prącik, PhD, for his help in preparing the experimental part of my dissertation. Thank you for your time, our conversations, and friendly support in difficult moments.

I wish to acknowledge the help provided by the university colleagues from the Mechanical Department, with special thanks to Maciej Ryś, MSc, for our endless discussions on science and ‘life’, which made me understand a lot.

I am also grateful to Aneta Ustrzycka, PhD, Rafał Ortwein, PhD, and Dawid Marcinek, PhD, for their unfailing support during my work on this Thesis.

My special thanks are extended to my Parents, Sister and Brother – for their boundless support and faith in my success. Thanks to you I have been pursuing my career goals.

I want to thank my friends, especially Bartek Kruczek and Mirosław Panek, for their “concern about maintenance of moderation in my devotion to Science”.

My thanks would be incomplete if I forgot to thank Sandra Bunk for her support and inspiration in achieving my objectives.

This work has been supported by the Małopolski Fundusz Stypendialny – DOCTUS through the Grant No ZS.4112-110/12.

# Podziękowania

Wyrażam wdzięczność promotorowi niniejszej rozprawy, panu prof. dr hab. inż. Błażejowi Skoczeniowi za nieocenione wsparcie merytoryczne, za doświadczenie oraz za poświęcony czas na przygotowanie tej pracy. Dziękuję za wiarę we mnie oraz za inspirowanie w dążeniu do realizacji wyznaczonych celów naukowych.

Składam wyrazy podziękowania panu dr. inż. Michałowi Prącikowi za pomoc w przygotowaniu części eksperymentalnej niniejszej pracy. Dziękuję za poświęcony czas, za wartościowe rozmowy oraz za przyjacielskie wsparcie w trudnych sytuacjach.

Serdecznie dziękuję koleżankom i kolegom z Wydziału Mechanicznego, w szczególności mgr. inż. Maciejowi Rysiowi za niekończące się dyskusje o nauce i o „życiu”, dzięki którym zrozumiałem wiele.

Dziękuję dr Anecie Ustrzyckiej, dr. inż. Rafałowi Ortweinowi oraz dr. inż. Dawidowi Marcinkowi za wsparcie, którego udzielali mi w czasie przygotowywania tej rozprawy.

Dziękuję Rodzicom, Siostrze i Bratu, za wiarę w mój sukces. To dzięki Wam w trudnych chwilach mogłem swobodnie realizować zawodowe plany.

Dziękuję Przyjaciołom, w szczególności Bartkowi Kruczkowi i Mirosławowi Pankowi, za „troskę o mój umiar w poświęcaniu się Nauce”.

Podziękowanie to byłoby niepełne, gdybym nie wyraził wdzięczności Sandrze Bunk za wsparcie i za inspiracje w dążeniu do celu.

Dziękuję również za otrzymane wsparcie finansowe ze środków Małopolskiego Funduszu Stypendialnego w ramach grantu Doctus ZS.4112-110/12.

# Abstract

The experimental investigation and modelling of strain localization in the course of discontinuous plastic flow (DPF) at extremely low temperature is a subject of the Thesis. DPF is observed during plastic deformation in face centered cubic (fcc) materials. An austenitic stainless steel is a good example of such material, which also undergoes in the cryogenic conditions the plastic strain induced  $\gamma-\alpha'$  phase transformation. The plastic flow instability is manifested by the stress oscillation as a function of strain (the so-called serrations on a stress-strain curve). DPF is attributed to the mechanism of local catastrophic failure of lattice barriers (including Lomer–Cottrell locks), under the stress fields related to the accumulating edge dislocations. Failure of lattice barrier leads to massive motion of released dislocations, accompanied by step-wise increase of the strain rate (macroscopic slip), drastic drop of stress and heat generation.

Uniaxial tensile test results indicate strain localization in the form of shear bands propagating along the specimen. The plastic power dissipated in the shear band is partially converted to heat, which results in a local drastic increase of temperature promoted by the so-called thermodynamic instability. Thus, the Dirac-like temperature function is measured by thermometers located in the gage length of the sample. Spatio-temporal correlation indicates smooth (regular) shear band propagation, as long as the process of phase transformation remains on hold and random pattern of propagation when the transformation occurs.

A physically based constitutive model, presented in the Thesis, describes DPF coexisting with phase transformation. The main idea is based on the assumption, that the evolution of new martensitic phase in the austenite affects the strain hardening modulus during each serration. Also, the strain localisation reflected by the temperature distribution has been implemented. The experimentally measured profile of temperature spikes has been explained by building a model of “travelling” slip band, carrying the representative volume element (RVE), and a fixed thermometer located in the middle of the sample. Thus, based on the Green-like solution and the initial conditions of the test, as well as the experimentally identified test parameters, it is possible to obtain numerically, the time response of the thermometer during the uniaxial tensile test at liquid helium temperature (4.2 K).

A comparison of the experimental stress-strain curve and the time response of the thermometer with the numerical results, indicates correct behaviour of the constitutive model of DPF including the effect of phase transformation, as well as the thermodynamic description of “travelling” slip bands, in austenitic stainless steels.

# Streszczenie

Tematem niniejszej rozprawy doktorskiej jest modelowanie zjawiska lokalizacji odkształceń podczas nieciągłego płynięcia plastycznego (NPP), w oparciu o wyniki testów jednoosiowego rozciągania w temperaturach kriogenicznych. Zjawisko NPP zaobserwowano w materiałach krystalicznych o strukturze regularnej ściennie centrowanej (RSC). Do tej grupy materiałów należy stal austenityczna, w której podczas deformacji dochodzi do indukowanej odkształceniowo przemiany typu  $\gamma-\alpha'$ . Nieciągłe płynięcie plastyczne charakteryzuje się oscylacją naprężenia w funkcji odkształcenia (występowanie tzw. serracji na krzywej naprężenie-odkształcenie). Efekt ten związany jest z mechanizmem ścicia barier (np. barier Lomera-Cottrela) w płaszczyźnie łatwego poślizgu, pod wpływem pola naprężeń, jakie generowane jest przez spiętrzające się na barierze dyslokacje krawędziowe. Zniesienie bariery uruchamia masowy i kolektywny ruch dyslokacji, co powoduje skokowy wzrost prędkości odkształcenia (poślizg makroskopowy), nagły spadek naprężenia, oraz dysypację ciepła.

W oparciu o przeprowadzone testy jednoosiowego rozciągania próbki wykonanej ze stali austenitycznej, zidentyfikowano efekt lokalizacji odkształceń w postaci pasma poślizgu propagującego wzdłuż części pomiarowej próbki. Energia dysypowana przez pasmo poślizgu jest częściowo zamieniana na ciepło, które powoduje lokalny wzrost temperatury. Efekt ten, związany jest z niestabilnością termodynamiczną, charakterystyczną dla materiałów krystalicznych, gdy temperatura otoczenia zmierza do 0 K. Czujnik pomiarowy zamontowany na próbce, rejestruje podczas testu sekwencję pików temperatury, które mają charakter funkcji Diraca. Na podstawie zarejestrowanego sygnału, można stwierdzić, że dla zakresu odkształceń plastycznych bez przemiany martenzytycznej, propagacja pasma poślizgu ma charakter regularny (uporządkowany). Przemiana martenzytyczna sprawia, że pasmo poślizgu „wędruje” w sposób nieregularny.

Przedstawiony w pracy model konstytutywny opisuje efekt NPP, na który oddziałuje przemiana martenzytyczna. Model zakłada, że nowa faza martenzytu wpływa na moduł wzmocnienia odkształceniowego podczas każdej serracji. W pracy przedstawiono również opis konstytutywny efektu lokalizacji odkształceń w oparciu o rozkład zarejestrowanej podczas testu temperatury. W tym celu, zaproponowano model „wędrującego” pasma poślizgu wraz z reprezentatywnym elementem objętościowym (REO), względem przestrzennie określonego czujnika temperatury. W oparciu o funkcję Greena rozwiązano równanie różniczkowe przewodnictwa cieplnego z warunkami początkowymi oraz parametrami termo-mechanicznymi zidentyfikowanymi doświadczalnie. Na podstawie przeprowadzonej analizy numerycznej, możliwe jest otrzymanie odpowiedzi czasowej czujnika temperatury podczas jednoosiowego rozciągania próbki w temperaturze ciekłego helu (4.2 K).

Wyniki analizy numerycznej przedstawionych modeli wykazują zgodność z wynikami eksperymentalnymi otrzymanymi podczas testu jednoosiowego rozciągania.

# Contents

<b>Acknowledgements .....</b>	<b>I</b>
<b>Abstract .....</b>	<b>III</b>
<b>Notation .....</b>	<b>VII</b>
<b>1. Introduction .....</b>	<b>1</b>
<b>2. State of the Art.....</b>	<b>9</b>
2.1. Materials applied at low temperatures .....	9
2.2. Near 0 K thermodynamic instability in metals and metallic materials.....	12
2.3. Strain localisation during discontinuous plastic flow (DPF).....	13
2.3.1 Low-temperature DPF versus other types of plastic flow instability .....	13
2.3.2 Nucleation and evolution of phase transformation at low temperatures .....	17
<b>3. The aim and the scope of the Thesis .....</b>	<b>20</b>
<b>4. Experimental evidence of strain localisation during DPF.....</b>	<b>22</b>
4.1. Experimental techniques to observe slip band evolution .....	23
4.2. Cryogenic set-up for tensile tests.....	28
4.3. Test results.....	31
4.3.1 Verification of the DPF nature .....	33
4.3.2 Strain rate effect .....	36
4.3.3 Strain localisation effect during DPF .....	39
4.3.4 Experimental set-up to identify parameters of slip band propagation.....	41
4.3.5 Dynamic behaviour of extensometer-specimen structure during DPF.....	45

<b>5.</b>	<b>Modelling of strain localisation during the DPF .....</b>	<b>48</b>
5.1.	Constitutive Model of discontinuous plastic flow .....	49
5.1.1.	Kinetics of DPF.....	49
5.1.2.	RVE based constitutive description of DPF .....	53
5.2.	Constitutive model of $\gamma$ - $\alpha'$ phase transformation .....	61
5.2.1.	Plastic strain induced phase transformation.....	61
5.2.1.1	Phase transformation affected DPF .....	64
5.2.1.2	Kinetics of the strain induced martensitic transformation.....	65
5.2.1.3	RVE based constitutive description of $\gamma$ - $\alpha'$ phase transformation .....	71
5.2.2.	The constitutive model.....	73
5.2.3.	The stress-strain relation .....	75
5.2.4.	The yield surface.....	78
5.2.5.	The associated flow rule .....	79
5.2.6.	Evolution of the hardening variables .....	83
5.2.6.1	Kinematic hardening .....	84
5.2.6.2	Isotropic hardening.....	95
5.2.6.3	Mixed hardening.....	95
5.3.	Thermodynamic model of strain localisation in DPF.....	97
5.3.1.	Solution of heat diffusion equation.....	98
<b>6.</b>	<b>Numerical model .....</b>	<b>102</b>
6.1.	Computational aspects of DPF coexisting with phase transformation .....	102
6.2.	Numerical model of strain localisation during DPF .....	110
6.3.	Numerical results .....	112
<b>7.</b>	<b>Discussion.....</b>	<b>121</b>
<b>8.</b>	<b>Conclusion.....</b>	<b>125</b>
<b>9.</b>	<b>Bibliography .....</b>	<b>127</b>

# Notation

## Acronyms

bcc	body centered cubic
CERN	European Organization for Nuclear Research
DPF	discontinuous plastic flow
DSA	dynamic strain ageing
fcc	face centered cubic
hcp	hexagonal close packed
HSFE	high stacking fault energy
L-C	Lomer-Cottrell
LHe	liquid helium
LHC	Large Hadron Collider
LSFE	low stacking fault energy
MRI	magnetic resonance imaging
PLC	Portevin–Le Chatelier (effect)
RT	room temperature
RVE	representative volume element
SEM	scanning electron microscope
SRS	strain rate sensitivity
ss	stainless steel

## General Notation

$A$	scalar
$\dot{A}, A_{,t}$	time derivative
$\underline{A}, A_i$	1 <sup>st</sup> order tensor (vector)
$\underline{\underline{A}}, A_{ij}$	2 <sup>nd</sup> order tensor
$\underline{\underline{\underline{A}}}, A_{ijkl}$	4 <sup>th</sup> order tensor

## Greek Symbols

$\beta$	Bauschinger parameter
$\underline{\underline{\varepsilon}}$	strain tensor
$\underline{\underline{\varepsilon}}^{bs}$	free deformation tensor (Bain strain tensor)
$\underline{\underline{\varepsilon}}^p$	plastic strain tensor
$\underline{\underline{\varepsilon}}^{th}$	thermal strain tensor
$\lambda$	thermal conductivity
$\dot{\lambda}$	plastic strain multiplier
$\bar{\lambda}$	mean free path of dislocation
$\mu$	shear modulus
$\mu^*$	shear modulus of the Hill influence tensor
$\mu_m$	shear modulus of martensite
$\mu_{MT}$	shear modulus of two-phase continuum
$\mu_{ta}$	tangential shear modulus of austenite
$\nu$	Poisson's ratio
$\nu_a$	Poisson's ratio of austenite
$\nu_m$	Poisson's ratio of martensite
$\xi$	volume fraction of martensite
$\rho$	dislocations density
$\rho_m$	mass density
$\underline{\underline{\sigma}}$	stress tensor
$\sigma_0$	yield stress
$\tau$	average resolved shear stress
$\tau_e$	stress at the head of dislocation pile-up
$\tau_0$	intrinsic lattice strength (Peierls stress)

## Latina Symbols

$B$	surface density of lattice barriers
$b$	Burgers vector
$C_{a0}$	tangential stiffness modulus of pure austenite
$C_{a+m}$	homogenised tangent stiffness modulus of phase continuum
$C_X$	kinematic hardening modulus
$C_V$	specific heat
$d$	average grain size
$\underline{\underline{E}}, \underline{\underline{E}}_{ijkl}$	tensor of elasticity
$\underline{\underline{E}}_H, \underline{\underline{E}}_{MT}$	tangent stiffness tensor of two-phase continuum
$\underline{\underline{E}}_m$	elasticity tensor of martensite
$\underline{\underline{E}}_{ta}$	linearized tangential stiffness operator of austenite
$E^*$	Hill's influence tensor
$F_{LC}^+$	function of lattice barriers density
$H$	Heaviside function
$\underline{\underline{I}}, \underline{\underline{I}}_{ijkl}$	identity tensor
$\underline{\underline{J}}, \underline{\underline{J}}_{ijkl}$	volumetric part of identity tensor (4 <sup>th</sup> order projector)
$J_2$	2 <sup>nd</sup> invariant of the stress deviator
$\underline{\underline{K}}, \underline{\underline{K}}_{ijkl}$	deviatoric part of identity tensor (4 <sup>th</sup> order projector)
$k$	bulk modulus
$k^*$	bulk modulus of the Hill influence tensor
$k_a$	dislocation annihilation constant
$k_i$	coefficients of dislocations evolution
$k_m$	bulk modulus of martensite
$k_{MT}$	bulk modulus of two-phase continuum
$k_{ta}$	tangential bulk modulus of austenite
$M$	Taylor's factor
$M_d$	transient temperature for phase transformation
$p$	accumulated plastic strain

$R$	isotropic hardening
$\underline{s}$	deviatoric stress tensor
$T_0$	transition temperature for HSFE materials
$T_1$	transition temperature for LSFE materials
$\underline{X}, \underline{X}_a$	back stress tensor
$\underline{X}_{a0}$	back stress of pure austenite
$\underline{X}_{a\xi}$	back stress related to the Orowan mechanism
$Q$	intensity of internal heat source

# Chapter 1

## Introduction

Modern science needs very sophisticated and complex tools in order to explore the Universe. Large Hadron Collider (LHC) in the European Organization for Nuclear Research is the world largest and the most powerful particle accelerator. The aim of the LHC is exploration of the world of elementary particles constituting the matter, for instance, investigation of quark-gluon plasma, that existed in the early universe. In order to perform such investigations, the cryogenic technology chosen for the LHC uses superfluid helium (1.9 K). On the other hand, space agencies promote missions of space probes (e.g. New Horizon) to explore our solar system. When space probes leave the Earth's orbit, they experience extremely low temperatures in the Universe.

There is a large variety of materials suitable for applications at extremely low temperatures: from the austenitic stainless steels to the glass fibre-epoxy composites. Investigation of materials behaviour, and their physical and mechanical properties, at the temperatures near 0 K is crucial to ensure proper work of such sophisticated research instruments like the LHC or the space probes.

Quick research through the bibliographic databases (e.g. "Web of Knowledge") shows that since 1976, more than 200 articles related to cryogenic temperatures and metallic materials such as steel (Fig. 1a) were published. It can be explained by the fact, that currently most sophisticated research instruments with cryogenic technology, such as particles accelerators (e.g. Large Hadron Collider at CERN, SuperKEKB at The High Energy Accelerator Research Organization or Relativistic Heavy Ion Collider at BNL), space probes (e.g. Voyager 1 and 2, New Horizons, Dawn, Juno, etc.), ultra-high-field magnetic resonance or nuclear magnetic

resonance (NMR) instruments, consist of elements made of metallic materials such as steel, copper, aluminium, etc. In Fig. 1b a fraction of over 200 articles in different research fields is presented. It can be concluded, that materials science, engineering, metallurgical engineering and physics represent the research fields where exploitation of metallic materials at cryogenic temperatures is widely considered. Moreover, the interest in metallic materials at cryogenic temperatures rapidly increases (Fig. 1a).

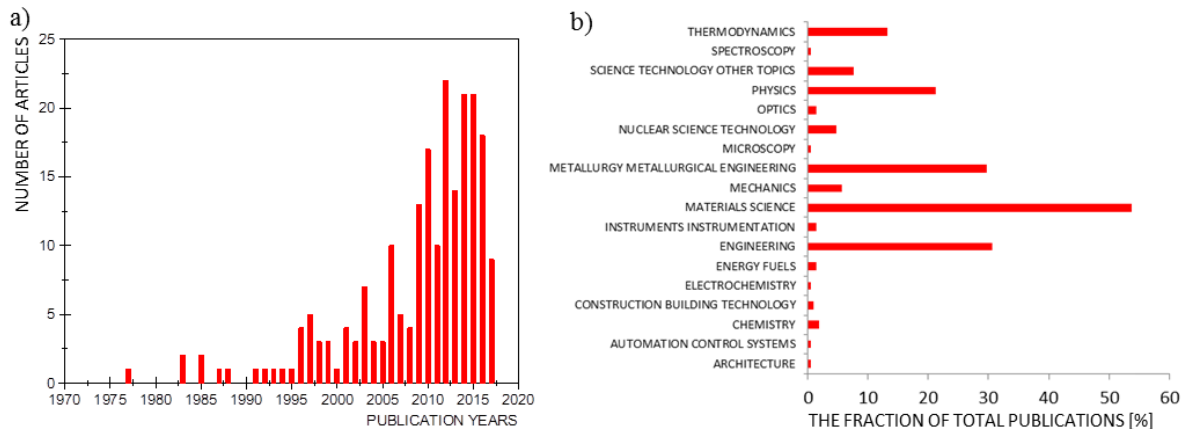


Fig. 1 Number of articles per year including the notions "cryogenic temperatures" and "steel" either in their title, their abstract, or in their keywords; b) the division into the scientific fields

Fcc metals and alloys are commonly applied in modern cryogenic installations within the whole range of temperatures, from near 0 K to the ambient temperature. Such materials, like copper and its alloys, aluminium alloys or stainless steel, show excellent physical and mechanical properties including high ductility and durability at extremely low temperatures. It is worth pointing out, that during plastic deformation at such extreme conditions, the metallic materials may undergo the plastic flow instability (the so-called discontinuous plastic flow), the strain induced phase transformation or the damage evolution (Tabin et al., 2017). To illustrate the strain induced phenomena that occur at extremely low temperatures, the stress-strain curves of selected alloys (Ni-Ti6Al4V, 304 stainless steel), used for structural applications at cryogenic temperatures, are shown in Fig. 2.

In regard to temperature, three domains of the response of specimen during the tensile test are distinguished: below  $T_0$  or  $T_1$ , where the discontinuous plastic flow (DPF) occurs, below  $M_d$  where the diffusionless plastic strain induced  $\gamma - \alpha'$  phase transformation occurs, and above  $M_d$  where the smooth plastic flow is observed (Fig. 2).

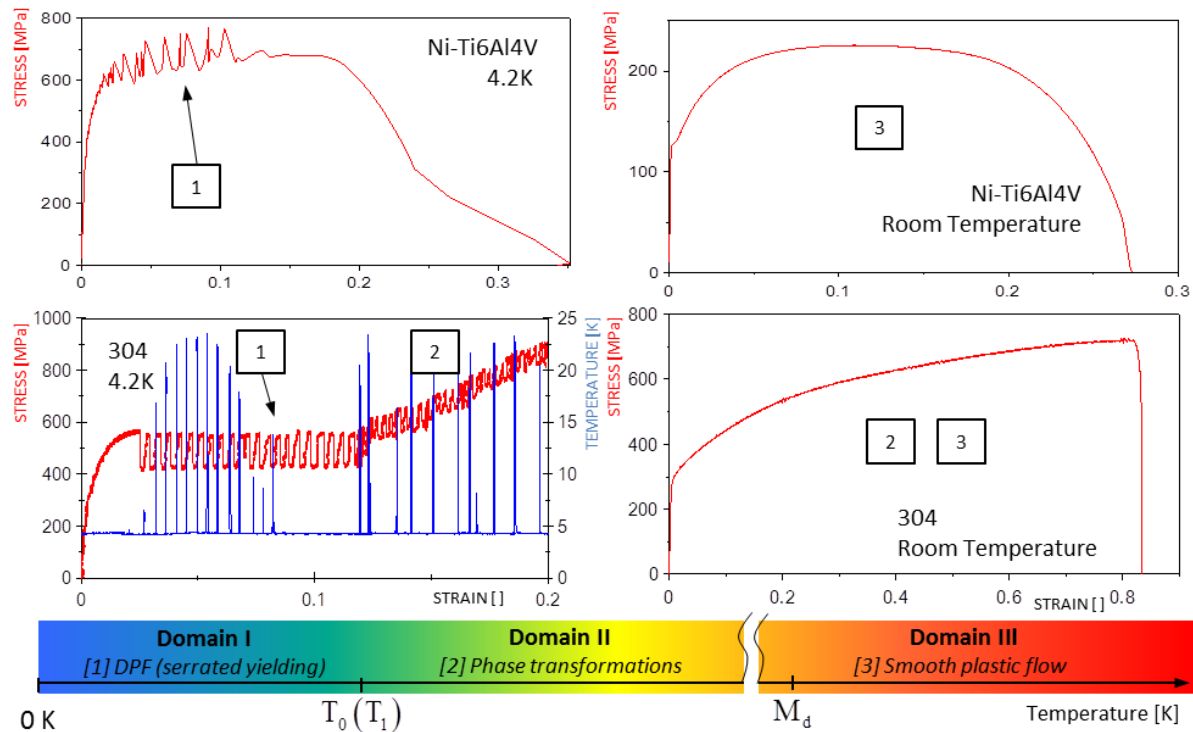


Fig. 2 Strain induced phenomena as a function of temperature: discontinuous plastic flow (DPF) [1], phase transformation [2], smooth plastic flow [3] (engineering stress-strain curves) (Tabin et al., 2016)

The DPF is observed in many low (LSFE) and high (HSFE) stacking fault energy materials strained at extremely low temperatures (Obst and Nyilas, 1991). Macroscopically, DPF is reflected in the stress-strain curve by the stress oscillations as a function of strain or time (the so-called serrations), (Fig. 2). The DPF takes place below a thermal threshold, characteristic of given material:  $T_1$  for LSFE materials and  $T_0$  for HSFE materials (both transition temperatures are material dependent). Thus, the temperature has an influence on the DPF, as well as the chemical composition, the stress state and the strain rate. Serrated yielding occurs within a wide range of strain rates (Komnik et al., 1985; Reed et al., 1988; Reed and Walsh, 1988; Pustovalov, 2008). Transition from the DPF to the smooth plastic flow occurs when the strain rate exceeds a critical value, and nearly adiabatic accumulation of heat takes place, causing fast increase of temperature of the sample to the level above  $T_1$  or  $T_0$ . It appears, that the lower limits of the strain rate do not play an important role. As soon as the critical temperature level is reached, a transition from serrated to smooth plastic flow is observed and the DPF temporarily disappears (cf. stress-strain curve of Ni-Ti6Al4V at 4.2 K, Fig. 2). The material is back to the oscillatory mode of plastic flow when the temperature decreases below  $T_1$  or  $T_0$  (Tabin et al., 2016). It is

worth pointing out, that a thermodynamic instability is observed in the materials at the temperatures approaching 0 K. It results in strong oscillations of temperature due to heat accumulation in shear bands (strain localisation effect) during plastic deformation (Fig. 2, 304ss, 4.2 K, blue curve). Such a thermodynamic effect results from the vanishing specific heat and thermal conductivity when the temperature approaches absolute zero.

During the plastic deformation in the austenitic stainless steel, below temperature  $M_d$  (normally higher than  $T_1$ ), the  $\gamma - \alpha'$  phase transformation occurs (Garion and Skoczen, 2002; Skoczeń, 2007). The face centered cubic microstructure of the austenitic stainless steel is metastable. Thus, the plastic deformation, as well as the applied stress, may induce a diffusionless martensitic phase transformation, by which the  $\gamma$  austenite phase (fcc) is transformed to the  $\alpha'$  martensite phase (bcc). It appears that the hardening effect observed in Fig. 2 (304ss, 4.2 K, blue curve) has for obvious reasons the strain induced background, related to the phase transformation.

It is well-established, that the intersections of the shear bands can form very effective plastic strain induced nucleation sites of martensitic embryos. It appears, that the growth of the  $\alpha'$  martensite phase occurs through the continuous nucleation and the coalescence of  $\alpha'$  martensite embryos during plastic deformation. New phase significantly affects sequential spreading (“travelling”) of slip bands during the test. It is quite probable, that the slip bands are pinned by the martensitic phase. Then, the place where a new slip band occurs depends on the materials imperfections. Such a strain localisation effect is reflected by the temperature distribution during the tensile test of stainless steel specimen at LHe temperature. “Travelling” slip band generates certain amount of heat (during serration), recorded by the thermometer in the form of temperature peaks. Distribution of temperatures spikes in the range without phase transformation has a regular comb-like form. It means that the slip band propagates from one extremity of the specimen to the other and from serration to serration, whereas, the distribution of temperature spikes within the hardening range is random (Fig. 2, 304, 4.2 K, blue curve).

In addition to the above phenomena, the evolution of micro-damage at extremely low temperatures is observed in the materials (e.g. austenitic stainless steels). Evolution of micro-damage in the course of discontinuous plastic flow (DPF) has been discussed in Tabin et al. (2017). In the Thesis, the influence of micro-damage evolution on DPF is omitted. However, the

model of DPF coupled with the phase transformation and the micro-damage evolution is under consideration.

Cryogenics has many applications nowadays (Fig. 3). The knowledge about the material behaviour, mechanical and physical properties is crucial for development and investigation of elements and structures which work at cryogenic temperatures. For example, austenitic stainless steel, because of its excellent combination of mechanical and physical properties was chosen for load-bearing structures of large superconducting magnets in the Large Hadron Collider at the European Organization for Nuclear Research (CERN). CERN builds particle accelerators and colliders. It can generate beams of different types of particles (electrons, positrons, protons, antiprotons and "heavy ions"). The structure of circular accelerator consists of accelerating cavities, bending main dipoles (MB) to keep the beam on its circular orbit, and quadrupole magnets to focus and defocus the beam. In the LHC, two-in-one beam transport system accelerates the protons to 6.5 TeV (since 20 May 2015), in the opposite directions, and then the collision takes place. It is well-known that the high magnetic bending field is required for high-energy beams. In order to bend 6.5 TeV protons around the ring, 1232 dipoles (MB) must be able to produce nominal magnetic field of 8.36 T (Garion, 2003). Main dipole consists of 2 coils per aperture clamped around the cold bore by a common set of austenitic steel collars, surrounded by an iron yoke and a shrinking cylinder, for a total mass of about 23.8 tons. The cross section of a standard dipole magnet for the LHC is presented in Fig. 4b. The coils and the collars are cooled to the temperature of 1.9 K, using large quantities of superfluid liquid helium.



Fig. 3 Cryogenic technologies and applications: a) Large Hadron Collider at CERN; b) person undergoing a magnetoencephalography<sup>1</sup>; c) power grid in the Long Island (USA), LIPA project; d) space shuttle during take-off<sup>2</sup>; e) high-speed monorail train using magnetic levitation (MagLev)<sup>3</sup>

<sup>1</sup> [https://images.nih.gov/public\\_il/image\\_details.cfm?id=80](https://images.nih.gov/public_il/image_details.cfm?id=80)

<sup>2</sup> <https://www.flickr.com/photos/nasacommons>

<sup>3</sup> <https://en.wikipedia.org/wiki/Maglev#/media/File:Transrapid.jpg>

During initial cool-down of 31000 tons of material, 700000 litres of liquid helium is required. After cool-down, the integrated thermal contraction is about 70 m. The compensation systems consist of bellows expansion joints (made of austenitic stainless steel), that are installed between the magnets. They have usually a form of thin-walled, corrugated, axisymmetric shells, located in the interconnections between the “rigid” portions of the system. These compensation elements provide continuity of the cryogenic or vacuum channels, compensate for the thermal expansion/contraction and provide a transverse flexibility in the case of misalignment of the rigid portions (Skoczeń, 2004). The austenitic stainless steels are used for such cryogenic applications because of their ductility at low temperatures, and their magnetic and vacuum properties (Garion, 2003).

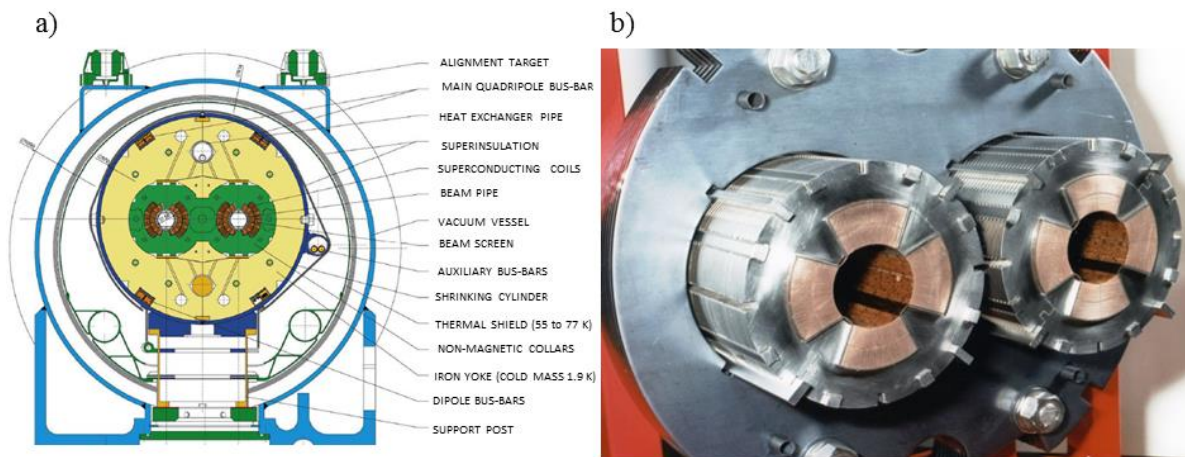


Fig. 4 Cross section of dipole magnets in the LHC (CDS CERN<sup>4</sup>)

The electrical resistance of most metals decreases with temperature. Below the threshold temperature, as a result of phase transition, certain metals lose all electrical resistance and become superconductors. A superconducting magnet, built by using a wire made of commercially available superconductor, can produce extremely high magnetic fields. For instance, niobium-titanium alloys cooled to 4.2 K, are used to build the magnets for magnetic resonance imaging (MRI) instruments<sup>5</sup>. In the field of such a magnet, the natural resonance of atoms in the investigated object is used to obtain images of object structure (e.g. human tissue). The interest in the magnetic resonance imaging (MRI) began with discoveries related to nuclear magnetic resonance (NMR) in the early 1900s<sup>6</sup>. Conventional MRI instruments use strong magnetic fields.

<sup>4</sup> <http://cds.cern.ch/>

<sup>5</sup> <http://cryogenics.nist.gov/AboutCryogenics/about%20cryogenics.htm>

<sup>6</sup> <http://www.madehow.com/Volume-3/Magnetic-Resonance-Imaging-MRI.html>

On the other hand, a SQUID (superconducting quantum interference device) is a very sensitive magnetometer used to measure extremely low (subtle) magnetic fields. Thus, the extreme sensitivity of SQUIDs makes them ideal for studies in biology, medicine, etc. Magnetoencephalography (MEG), for example, uses measurements from an array of SQUIDs to make inferences about neural activity inside brains. Modern MEG systems, equipped with the cryogenic systems, have hundreds of SQUID detectors and operate inside large magnetically shielded rooms (Fig. 3b).

Maglev is another example of technology where the cryogenic system is used. It is a public transport technology that uses magnetic levitation to move vehicles (Fig. 3e). In Maglev, superconducting magnets suspend a train car above a U-shaped concrete guideway. In this case, the superconducting magnets with load-bearing structure work at cryogenic temperatures. The first commercially operated high-speed superconducting Maglev train opened in Shanghai in 2004, while others are in operation in Japan and South Korea.

Space shuttles and space probes are exposed to extremely low temperatures during spaceflight into or through outer space (Fig. 3d). The superconducting magnets are also used in space probes detector. For instance the Alpha Magnetic Spectrometer (AMS-02) was mounted in the International Space Station (ISS). One of the AMS-02 detectors measures antimatter in the cosmic rays (on 13 August 2017, some 104 580 054 845 cosmic rays measured by AMS-02). This information allows to understand the formation of the universe. These detectors include superconducting magnets which at 1.8 K generate a required central field of 0.87 T (Tesla).

It is worth pointing out, about LIPA Project (Long Island Power Authority's Project), where the high temperature superconducting (HTS) power cables are used in the Long Island power grid. The cable represents the world's first installation of a superconducting cable in the electrical power transmission network. HTS cables conduct electricity with no electrical losses. It is possible when the cables are cooled down below a critical temperature. In this case, HTS power cables work at liquid nitrogen temperature (77 K).

In view of the foregoing, knowledge about the materials behaviour, the mechanical and the physical properties, is crucial for development and investigation of elements and structures that operate at cryogenic temperatures.

## Chapter 2

# State of the Art

### 2.1. Materials applied at low temperatures

Nowadays, materials investigations include studies of the properties of materials at extremely low temperatures, including proximity of absolute zero (for instance 0.001 K). There are many parameters which define suitable material for cryogenic applications, among them: mechanical parameters (yield and ultimate strength, elastic modulus, strain to rupture, etc.), physical properties (specific heat, magnetic permeability, outgassing rate, etc.), thermal properties (thermal conduction, surface emissivity, etc.), weldability and obviously cost of fabrication and accessibility on the market (Skoczeń, 2004). Ductile materials, such as the austenitic stainless steels, the copper alloys, and the aluminium alloys are the most often used construction materials for the cryogenic applications (see Table 1).

Table 1 Materials for cryogenic systems (Skoczeń, 2004)

Material	Grade	Application
austenitic stainless steel	304, 304L	tubes, cylinders, braiding wires (metal hoses)
	316L	thin-walled shells (bellows exp. joints, corrugated tubes), sheets, piping
	316LN	massive parts, high strength expansion loops, vacuum barriers
carbon steels		cryostats, vacuum vessels
copper and copper alloys	OFHC	heat exchangers, heat transfer applications, bus bars, thermalisation straps
aluminium alloys	series 1000 and 3000	thermal shields
	series 5000 and 6000	extrusions and piping, aluminium/st. steel transitions

titanium	Ti-6Al-4V Ti-5Al-2.5Sn	supports and high strength components
special alloys	Hastelloy	dewar components
Invar		low shrinkage components, tubes
composition	glass fibre/epoxy: G10, G11	fixed and sliding supports, spacers, cold feet, vacuum barriers
	carbon-carbon	small spacers
Peek	polyetheretherketone	spacers
Kevlar		filament winding
Mylar		super-insulation
Kapton		insulating strips
resins	polyetherimide resins	filling resins, glues
	epoxy resins	filling resins, glues

At such extreme conditions, most of them preserve ductility. It is worth pointing out, that at a temperature near 0 K the mechanical properties, such as elastic modulus, yield stress or ultimate strength, become higher than at room temperature. The most often used austenitic stainless steel grades at cryogenic temperature are: 304, 304L, 316L and 316LN (Table 1) (Skoczeń, 2004). Typical mechanical properties of stainless steels at liquid helium (4.2 K), at liquid nitrogen (77 K) and at room temperature (293 K) are presented in Table 2, Table 3.

For what concerns non-metallic materials used in the cryogenic conditions, glass fibre-epoxy composites (Skoczeń, 2004) are worth mentioning. The main advantage of the composites is their small thermal conductivity at cryogenic temperatures (compared to metallic materials). Table 2 shows the thermal parameters for the austenitic stainless steels and the glass-fibre epoxy composites at 4.2 K, 77 K, and at 293 K. It is worth pointing out, that an appropriate balance between thermal and mechanical properties of materials is crucial for the design of cryogenic systems. For instance, the stiffness of cryostat columns should be as high as possible, whereas the small thermal conductivity is required to reduce liquid helium evaporation ratio. Therefore, such cryostat columns are often made of G10, G11 composite rather than austenitic stainless steel, unless higher stiffness is required.

Table 2 Thermo-mechanical properties of typical materials used for cryostat building

Temp. [K]	Elastic modulus GPa			Thermal conductivity W/mK			Stiffness of single cryostat column N/mm		
	4.2	77	300	4.2	77	293	4.2	77	293
G10 (warp)	35,9 <sup>(1)</sup>	33,7 <sup>(1)</sup>	28 <sup>(1)</sup>	0,08 <sup>(4)</sup>	0,28 <sup>(4)</sup>	0,61 <sup>(4)</sup>	1076	1010	840
G11 (warp)	39,4 <sup>(1)</sup>	37,3 <sup>(1)</sup>	32 <sup>(1)</sup>	-	-	-	1181	1118	960
304	200 <sup>(2)</sup>	-	193 <sup>(2)</sup>	0,3 <sup>(4)</sup>	7,9 <sup>(4)</sup>	15,3 <sup>(4)</sup>	5997	-	4168
316LN	213 <sup>(3)</sup>	-	184 <sup>(3)</sup>	-	-	-	6387	-	5517

1. Superconducting Accelerator Magnets, An Introduction to Mechanical Design and Construction Methods, Carl L. Goodzeit (Retired BNL),
2. Brookhaven National Laboratory, Selected Cryogenic Data Notebook, Rev. 8/80, BNL 10200-R,
3. Structural Materials for Superconducting Magnets, Prepared by Simon and Reed, National Bureau of Standards, 1982,
4. Marquardt, E. et al.. 2000. Cryogenic material properties database. The 11th International Cryocooler Conference. Keystone, Co.

Typical mechanical properties of different materials at room and at cryogenic temperatures are shown in Table 3. It is worth pointing out, that the mechanical properties of the composite materials depend on two principal components: matrix (epoxy resin) and the fibres (glass or Kevlar fibres etc.).

Table 3 Mechanical properties of materials used in cryogenics

Temp. K	OFHC Copper			316 ss			G10	
	298	20	300	77	4	300	77	4
Yield stress MPa	69	86	216	314	431	-	-	-
Tensile strength MPa	172	455	529	1235	1441	260-460	460-830	500-870
Elastic modulus MPa	1.31·10 <sup>5</sup>	1.45·10 <sup>5</sup>	1.9·10 <sup>5</sup>	2.06·10 <sup>5</sup>	2.06·10 <sup>5</sup>	0.22·10 <sup>5</sup> 0.35·10 <sup>5</sup>	0.27·10 <sup>5</sup> 0.37·10 <sup>5</sup>	0.29·10 <sup>5</sup> 0.39·10 <sup>5</sup>

Brookhaven National Laboratory, Selected Cryogenic Data Notebook, Rev. 8/80, BNL 10200-R

## 2.2. Near 0 K thermodynamic instability in metals and metallic materials

Thermal conductivity, thermal contraction coefficient, or the state functions like specific heat tend to zero with temperature. It remains consistent with the third law of thermodynamics: the entropy of a perfect crystal at absolute zero is equal to zero. Such effect significantly influences the behaviour of metallic materials and metals at extremely low temperatures. Two mechanisms of heat transport occur in the lattice, namely: the phonon mechanism and the free electrons. The contribution of quantum lattice vibrations (phonons) is limited at extremely low temperatures to the acoustic modes. Based on the Debye theory, the lattice energy corresponding to the phonon states is derived (Kosevič et al., 2000):

$$E_{ph} \sim N \left( \frac{T}{\Theta} \right)^3 T \quad (1)$$

where  $N$  is the number of atoms in the lattice, and  $\Theta$  denotes Debye reference temperature. Thus, the specific heat under constant volume can be derived based on the internal energy of lattice, associated with the phonon excitations:

$$C_V = \left( \frac{\partial E_{ph}}{\partial T} \right)_V \sim N \left( \frac{T}{\Theta} \right)^3 \quad (2)$$

Hence, the specific heat is a nonlinear function of normalised temperature and tends to 0 with temperature  $T$ . Similar result can be obtained for the thermal conductivity. The specific heat and the thermal conductivity of 316L stainless steel as a function of temperature are presented in Fig. 5 (Skoczeń, 2004).

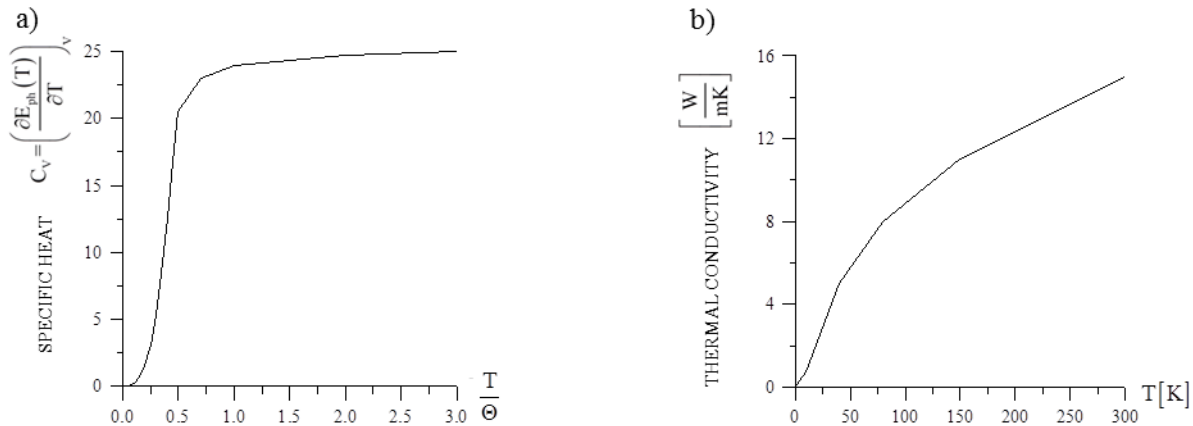


Fig. 5 a) Specific heat under constant volume (strain) as a function of temperature; b) thermal conductivity as a function of temperature for 316L stainless steel (Skoczeń, 2004)

The contribution of free electrons to the specific heat at low temperatures is expressed by:

$$(C_{el})_V \sim \frac{T}{T_F} \quad (3)$$

where  $T_F$  denotes the Fermi reference temperature. Thus, the specific heat has the following additive form:

$$C_V = (C_{el})_V + (C_{ph})_V \sim aT + bT^3 \quad (4)$$

Heat increment is related to the temperature increment by the following relation:

$$dQ = mC_V dT \quad (5)$$

where  $m$  is the mass of specimen. After simple rearrangements one obtains:

$$\frac{dT}{dQ} = \frac{1}{mC_V} \quad (6)$$

Thus, accepting that  $C_V \rightarrow 0$  when  $T \rightarrow 0$ , one obtains:

$$\frac{dT}{dQ} \rightarrow \infty \Big|_{T \rightarrow 0} \quad (7)$$

It means that significant increase of temperature is produced by an arbitrary small dissipation of energy in the lattice when the temperature tends to 0 K. Such energy dissipation can be induced by a plastic deformation consisting in the motion of dislocations in the lattice. The plastic work will be partially converted to heat (Taylor-Quinney coefficient), contributing to strong temperature oscillations. It is worth pointing out, that the above thermodynamic instability has fundamental meaning for the conditions of DPF coupled with phase transformation (Skoczeń et al., 2014).

## 2.3. Strain localisation during discontinuous plastic flow (DPF)

### 2.3.1 Low-temperature DPF versus other types of plastic flow instability

The occurrence of plastic flow oscillations during tensile test is related to qualitative change in deformation behavior, and is reflected by a transition from smooth to oscillatory mode of plastic deformation. Conditions under which such changes occur are closely related to strain localisation.

The Portevin–Le Chatelier (PLC) effect and the Lüders bands propagation are well-known plastic oscillation phenomena. At extremely low temperatures the plastic flow instability

has also been identified, and is called discontinuous plastic flow (DPF). The appearance of DPF is quite similar to the appearance of the Portevin–Le Chatelier (PLC) effect, i.e. the stress oscillations as a function of time or strain during a displacement controlled traction test. Zaiser and Hähner (1997) attribute discontinuous nature of plastic flow at cryogenic temperatures to the strain rate softening instabilities, and point out a similarity between the low-temperature DPF and the ambient temperature PLC. The strain rate sensitivity (SRS) consists, in their view, of the positive instantaneous response of the flow stress to a sudden increase in the strain rate. It is followed by the stress relaxation to a steady state asymptotic value. Nevertheless, the physical mechanisms of DPF and PLC are rather different, and their origins seem not to be the same (c.f. Obst, Nyilas, 1991). Judging by the appearances, the interaction of dislocations with the barriers at extremely low temperatures can be qualified as analogical response to the PLC. Both in the case of PLC and DPF, dislocations meet obstacles and are temporarily arrested/locked. However, in the course of PLC, solutes diffuse around the dislocations (Fig. 6a), and further strengthening of the obstacles is observed (Bross et al., 2003), whereas, in the case of DPF the obstacles remain stable because of weakly excited lattice and lack of thermal energy. Eventually, these dislocations will in both cases overcome the obstacles reaching sufficient level of local resolved shear stress, and will move to the next obstacle where they are stopped again. The difference between both mechanisms consists in the fact, that in the case of PLC the obstacles are created by diffusion, whereas, in the case of DPF the obstacles are “diffusionless”. Therefore, the PLC effect is qualified as a form of dynamic strain ageing (DSA)- the diffusive mechanism, which causes that a gliding dislocation segment may be subjected to an additional pinning due to the solute atoms migrating towards the dislocation core (Fig. 6a).

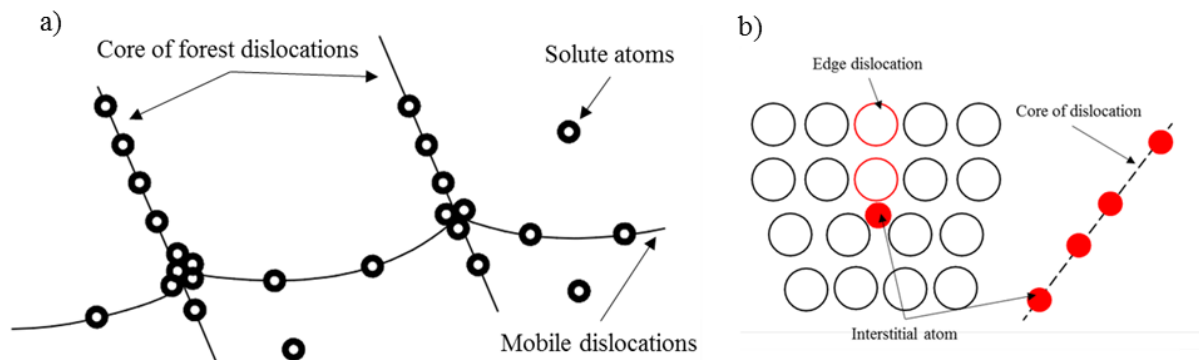


Fig. 6 Schemes of dynamic strain aging (DSA) causing PLC instability and b) Cottrell atmospheres formation during Lüders bands propagation

Lüders band propagation has a diffusive nature. From the phenomenological point of view, the Lüders phenomenon means the strain softening instability. On the other hand, in terms of the dislocation process, it is a complex phenomenon that involves the irreversible changes of the microstructure of the material (Zaiser and Hähner, 1997). Formation and propagation of the Lüders bands, e.g. in the mild steels under monotonic tension, are attributed to strong interactions of interstitial atoms with dislocations, known as the Cottrell atmospheres (Cottrell and Bilby, 1949). In the Cottrell atmospheres, the interstitial atoms segregate to dislocations and pin them in the position of lower lattice distortion energy (Fig. 6b). At the upper yield stress, the dislocations are unpinned from the Cottrell atmospheres and become free dislocations. These free dislocations can move at the lower yield stress and lead to a multiplication of new dislocations. Thus, the upper yield stress is regarded as the nucleation stress, and the lower yield stress is the growth stress of the Lüders bands (Zhang and Jiang, 2005).

It is worth pointing out, that during the Lüders phenomenon as well as during the DPF, the slip bands propagation occurs. In the kinematically controlled tests, the Lüders slip bands “travel” along the specimen. Typically, in the mild steels, the front makes a well-defined angle 45–55° to the specimen axis. The band nucleation, usually occurring at one grip due to the stress concentration, is associated with the elastic relaxation of the rest of the sample following the drop of stress from the upper yield stress to the lower yield stress. A slip band sequentially propagates through the specimen in the range of the so-called Lüders strain (Bućko et al., 2014). Similar effect has been discovered in the austenitic stainless steels during the kinematically controlled tensile test at 4.2 K (Tabin et al., 2016), and it is discussed in detail in this Thesis. Moreover, the phase transformation is observed during the plastic deformation accompanying the slip band propagation.

It is worth pointing out, that the DPF has not been sufficiently investigated when compared to the PLC effect, and to the Lüders phenomenon (Zaiser and Hähner, 1997). In particular, studies of spatio-temporal dynamics of the low-temperature plastic oscillations are greatly insufficient, at the experimental, the constitutive as well as at the numerical levels. Therefore, experimental identification of the strain localisation during DPF within near 0 K temperature range has been carried out. Then, based on the experimental results, the validation of the numerical model has been performed. A comprehensive analysis of the experimental and the numerical result is presented in the Thesis.

The first study of DPF was performed by Basinski in 1957 for a single crystal of Al-2%Mg. During the tensile test, the serrated flow appeared between two portions of smooth plastic flow. The temperature distribution was measured by means of niobium wire coils. It was shown, that the coil transitioned to the normal state during a jump of stress. First serrations were observed below 12 K and consistent serrated flow started below 5 K. Based on the experimental results, Basinski concluded, that the instability of plastic flow was caused by localised heating of the specimen. He assumed, that any sufficiently fast dissipative process at extremely low temperatures leads to the increase of local temperature (the plastic work is converted to heat) and, consequently, to a drastic decrease of the flow stress. This early stage hypothesis did not take into account the behaviour of stress (load), measured directly on the sample. The adiabatic hypothesis of DPF was also promoted by Estrin and Kubin (1980), (1988), Estrin and Tangri (1981), Shibata (1988), and Burns (1994).

Another explanation of DPF has been formulated by Seeger (1957) and Obst and Nyilas, (1991), (1998). According to their opinion, DPF is related to creation of lattice barriers during dislocations motion. The Authors point out, that the pile-ups of dislocations on the internal barriers (Lomer-Cottrell locks, Cottrell atmospheres, Suzuki locks, groups of interstitial atoms, dislocation forest, non-metallic inclusions etc.) in the lattice give rise to the stress concentrations. In their view, the load drops are due to a catastrophic process consisting in spontaneous creation of dislocations as soon as the internal barriers are broken. According to Obst and Nyilas, the plastic flow instability at cryogenic temperatures is mechanical in nature.

Both, the adiabatic heating hypothesis derived by Basinski (1957), and the mechanical approach developed by Seeger (1957), Obst and Nyilas (1991), reflect very complex nature of the flow instabilities that occur at extremely low temperatures. A combined approach to the discontinuous plastic flow (DPF), with the accompanying thermodynamic aspects of the phenomenon, were developed by Skoczeń et al. (2010, 2014), and Tabin et al. (2016, 2017).

Thus, the mechanism of discontinuous yielding is related to formation of dislocation pile-ups at strong lattice obstacles (e.g. the Lomer-Cottrell locks) during the plastic deformation at the temperatures below  $T_0$  or  $T_1$  (Obst and Nyilas, 1991; Obst and Nyilas, 1998; Pustovalov, 2008). During the plastic deformation at the temperatures near 0 K, in the fcc metals and alloys, it happens often, that the edge dislocations are dissociated in the slip plane into two Shockley partial dislocations, bounding the stacking fault ribbon. It happens, that the dislocations meet at

the line of intersection of the two planes, and the leading partials repel or attract each other. It is also called a “stair-rod” dislocation, by analogy with a carpet on a stair. The stair-rod partial therefore exerts a repulsive force on the two Shockley partials and these three partial dislocations form a stable, sessile arrangement. It acts as a barrier to the glide of further dislocations on two planes, and is known as the Lomer-Cottrell lock (Hull and Bacon, 2011a). The back stresses of the piled-up groups are supposed to block the movement of newly generated dislocations. The local shear stress at the head of the dislocation pile-up, proportional to the number of dislocation in the pile-up, can reach the level of cohesive strength and the Lomer-Cottrell barrier may collapse by becoming a glissile dislocation. It is a local catastrophic event, which can trigger similar effect in the other groups of dislocations. Thus, the final result is massive and has a collective character. It is followed by a spontaneous generation of dislocations by rapid increasing number of dislocation sources.

It is worth pointing out, that the mechanical background of DPF is coupled with the thermodynamic effects. Thus, the temperature increases rapidly due to the local catastrophic failure of lattice barriers. Such a thermodynamic effect results from vanishing specific heat and thermal conductivity, when the temperature tends to 0 K (see Section 2.2). Therefore, a constitutive model of DPF presented in the Thesis takes into account the mechanical background of the phenomenon, and the thermodynamic processes related to mechanisms of heat transport in a weakly excited lattice at very low temperatures. Moreover, during tensile tests at cryogenic temperatures the avalanche-like barrier crossing by dislocation pile-ups is manifested by acoustic effects of “dry” sounds, emitted by the specimen, that can be easily recorded. From the macroscopic point of view, the response of the specimen during the kinematically controlled uniaxial tensile test at cryogenic temperatures consists of oscillations of stress versus strain (the so-called serrations). Each serration has similar pattern: after the initial elastic process (1) smooth plastic flow takes place (2), until the abrupt drop of stress (3) and possible relaxation (4) occur (Skoczeń et al., 2010).

### **2.3.2 Nucleation and evolution of phase transformation at low temperatures**

During plastic deformation of austenitic stainless steel below temperature  $M_d$ , the strain induced phase transformation occurs (Garion and Skoczen, 2002; Skoczeń, 2007). Based on the experimental results, one concludes that the martensitic phase transformation significantly

influences macroscopic slip band propagation during DPF (see Fig. 2). It is worth recalling research papers by Suzuki et al. (1977) and Brooks et al. (1979a, b). The Authors have suggested, that the  $\alpha'$  martensite nucleation is associated with the piling-up of the Shockley partial dislocations (such partial dislocations generate the Lomer–Cottrell locks). Thus, as the dislocations are forced closer to each other in the pile-up, the atomic structure starts to resemble bcc stacking. As the pile-up reaches the critical size, a rapid growth of  $\alpha'$  martensite embryo occurs with the aid of the chemical driving force. It appears that the growth of the  $\alpha'$  martensite phase occurs during plastic deformation through the continuous nucleation and coalescence of the  $\alpha'$  martensite embryos (Murr et al., 1982). It is worth pointing out, that the volume of a unit cell of the martensite is greater than the primary volume of the austenite unit cell. This difference reaches some 3-5% of the primary volume (Garion, 2003).

The kinetics of the strain induced martensitic transformation has been experimentally investigated by Olson and Cohen (1975), Murr (1982), Staudhamer (1983), Shrinivas (1995), Iwamoto (1998), Ferreira (2004), Ortwein et al. (2016), etc. Based on the investigations and own experiments presented in these papers, it can be concluded that the chemical composition, the temperature, the plastic strain, the stress state and the strain rate may have significant influence on  $\alpha'$  phase transformation.

It is well-known that the  $\gamma - \alpha'$  phase transformation is reduced when the test temperature increases (Olson and Cohen, 1975). Such behaviour is attributed to the decrease in chemical driving force with temperature increase. Rate of the transformation is much higher at lower temperatures.

Murr et al. (1982) found that the biaxial tension generates higher number of shear band intersections (hence, martensitic phase), than a uniaxial tensile test. The reason is that more active slip systems occur under combined loading. More martensitic phase is also generated during cold rolling, than during a uniaxial tensile test (Shrinivas et al., 1995).

The next factor affecting the strain induced  $\gamma - \alpha'$  martensitic transformation is the strain rate effect. The experimental results indicate that the transformation is reduced with the increasing strain rate. Formation of  $\alpha'$  martensite is reduced due to the adiabatic heating, generated during the higher deformation rates. Such a process decreases the chemical driving force for the transformation (Ferreira et al., 2004). A different point of view is presented by Staudhamer (1983), who suggested that high strain rate may promote more irregular structure of

the shear bands. Thus, it can lead to reduction of the probability of formation of  $\alpha'$  martensite embryos. On the other hand, Hecker et al. (1982) and Murr et al. (1982), believe that high strain rate promotes shear band formation in the austenitic stainless steel. It leads to increase of the volume fraction of martensitic phase, but only at the early stages of tensile deformation. Generally, for higher strain rate, when the plastic deformation is advanced, the martensitic transformation is reduced due to the adiabatic heating (Ferreira et al., 2004).

It can be concluded that during the loading test at near 0 K temperature, the plastic deformation related to DPF takes place within the slip bands. The massive and collective collapse of lattice barriers in the slip bands is macroscopically reflected by the stress oscillations as a function of strain (the so-called “serrations” are observed). When the strain induced transformation occurs, the slip band is pinned by the martensitic phase. Then, the place where a new slip band is observed depends on the material imperfections.

## Chapter 3

# The aim and the scope of the Thesis

The strain localisation effect in the course of discontinuous plastic flow (DPF) at extremely low temperatures is investigated. fcc metals and alloys, strained in cryogenic conditions, undergo at low temperatures the discontinuous plastic flow (DPF), manifested by the so-called “serrated yielding”. The mechanism of DPF is related to the local catastrophic failure of lattice barriers (including Lomer–Cottrell locks), under the stress fields resulting from the accumulating edge dislocations. Failure of lattice locks leads to a massive motion of released dislocations, accompanied by step-wise increase of the strain rate (macroscopic slip) and abrupt drop of stress. Macroscopically, this effect is strongly localised (slip band propagation), and related to rapid increase of temperature due to the thermodynamic instability. Moreover, for austenitic stainless steels, the DPF is coupled with the strain induced phase transformation. It is well-established that the intersections of shear bands can be very effective nucleation sites of martensitic embryos. During plastic deformation, the “travelling” shear band is pinned by the martensitic phase. The place, where a new slip band would be observed depends on the materials imperfections.

Physically based constitutive model presented in the Thesis describes the DPF coexisting with the strain induced phase transformation. The strain localisation effect, reflected by temperature distribution, is described using the Green-like solution of heat diffusion equation.

The study consists of uniaxial tensile tests performed on austenitic stainless steel samples (grades: 304, 316L) at 4.2 K (liquid helium). During the tests, time response of the force and temperature transducers as well as the extensometers were recorded. Based on the time response, the stress-strain and the temperature-strain curves were plotted. The experimental set-up, with

two thermometers mounted on the specimen, allowed to determine the spatio-temporal characteristics of “travelling” slip bands (the slip band velocity, the frequency of serrations, etc.).

The scope of the Thesis has been summarised below in two categories: the experimental and the theoretical research:

#### Experimental research

- Determination of mechanical properties of fcc materials (austenitic stainless steels). During the kinematically controlled uniaxial tensile tests at liquid helium (4.2 K), the time response of the force transducer, the extensometers and the thermometers are recorded. Based on the time response of transducers, the stress-strain and temperature-strain characteristics are determined.
- Experimental verification of DPF origin (thermal or mechanical approach). Based on the uniaxial tensile test results the mechanically triggered drop of stress is confirmed.
- Experimental evidence of coupling between the DPF and the strain induced phase transformation in the austenitic stainless steels at 4.2 K.
- The spatio-temporal characteristics of slip band propagation during DPF is identified. Based on the time response of two thermometers mounted on the specimen during tensile test at 4.2 K, the parameters of “travelling” slip band are identified.
- Performing SEM analysis of ductile fracture of the material under consideration (304ss).

#### Theoretical research

- Developing thermodynamic model of “travelling” slip bands during DPF, coexisting with the phase transformation. Temperature distribution in this model is represented by Green-like solution of heat diffusion equation.
- Extending the DPF model to include the strain induced phase transformation.
- Developing evolution equations for dislocations density and for lattice barriers density during DPF, based on the experimental results.

The following thesis will be demonstrated in the course of the work: plastic flow at extremely low temperatures in the fcc materials is localized in the shear bands. The shear band can be spatially identified by means of temperature distributions resulting from the thermodynamic instability at near 0 K temperatures. The phase transformation process determines the kinetics of the shear band propagation and the DPF mode.

## Chapter 4

# Experimental evidence of strain localisation during DPF

Successful and responsible use of engineering materials at near 0 K temperatures requires basic knowledge about material properties at such extreme conditions. Tensile testing is the most common method to identify the mechanical properties. Moreover, tensile tests allow to find out the fundamental mechanical and metallurgical behaviour of the material during the deformation. The discontinuous plastic flow (DPF), the strain induced  $\gamma - \alpha'$  phase transformation and the damage evolution represent the most common phenomena that occur in ductile materials during deformation at cryogenic temperatures. These phenomena have not been studied extensively in the literature. The reason for such a lack of information on the behaviour of materials at extremely low temperatures is related to testing conditions and significant difficulties in the interpretation of the experimental data. It is worth pointing out, that the experiments are carried out inside a double-wall cryostat, which is not transparent and usually tightly equipped with all necessary instruments. Thus, there is practically no possibility to scan the surface of the sample using such instruments like the thermographic camera, with the view to detecting possible effects of strain localisation. In order to do so, specific deduction methods have to be used. They will be explained in the course of the present chapter.

It is well known, that the specimen clamping system, the shape and the dimensions of the specimen, the rigidity of the testing machine, the parameters of the test (crosshead speed, etc.), and the properties of tested materials can influence the accuracy of measurements. However, the researchers do not pay sufficient attention to the complex interactions between the specimen and the measuring apparatus. This can easily lead to erroneous interpretation of the tensile test results.

Dynamic behaviour of the clip-on extensometer during plastic flow instability (DPF) is a good example of such situation (Tabin and Prącik, 2015). In the present chapter, the analysis of extensometer – specimen structure behaviour during the strain localisation in the course of DPF is presented. The results of this analysis were applied during the development of new helium cryostat in the Engineering Department of the European Organization for Nuclear Research.

#### **4.1. Experimental techniques to observe slip band evolution**

During the plastic flow in the ductile materials, the process of strain localisation takes usually place (cf. Portevin–Le Chatelier effect, Lüders band propagation, or discontinuous plastic flow). Plastic flow is localized within a shear band that “travels” during the uniaxial tensile test from one extremity of the sample to the other. Different techniques have been developed and implemented to observe the nature of slip bands under plastic deformation at wide range of temperatures.

The experimental research of the PLC effect was focused mostly on recording the temporal and the spatial characteristics of slip bands. Such well known techniques like: the shadowgraph technique (Chihab et al., 1987), acoustic emission (Cáceres and Rodriguez, 1987; Vinogradov and Lazarev, 2012), use of a multi-zone laser extensometer (Ziegenbein et al., 2001), infrared thermography (Louche et al., 2005; Hu et al., 2012), electronic/digital speckle pattern interferometry (ESPI or DSPI) (Jiang et al., 2007; Labergere et al., 2014; Petit et al., 2014), digital speckle correlation (DSC) (Zhang et al., 2005), or digital image correlation (DIC) (Ait-Amokhtar et al., 2006; Nielsen et al., 2010) were used.

The slip band propagation in the aluminium alloy A2017 (nominal alloy composition: Al–4 wt.%Cu) during the kinematically-controlled test was recorded by Jiang et al. (2007). By employing the dynamic digital speckle pattern interferometry (DSPI), the spatial kinematic features of the Portevin–Le Chatelier (PLC) effect was investigated. The Authors have analysed the influence of strain and the applied strain rates on the amplitudes of serrations. Also, they experimentally analysed different types of serrated flow in the stress–time curves, combining with the position – the time plots for the propagating PLC bands (Fig. 7).

Similar methods were developed to observe the propagation of the Lüders bands, and to evaluate the strain profile near the Lüders front. Additionally, Lüders bands tracking and identification of local deformation can be carried out by means of the following methods: recording surface scratches (Hall, 1951; Iricibar et al., 1977), using optical “Toppler Schlieren”

method (Hall, 1951; Sylwestrowicz and Hall, 1951), applying critical macro-illumination (Boxall and Hundy, 1955), imposing stress-coat (Fisher and Rogers, 1956), applying clip-extensometer (Moon, 1971), using grid-reflection (Verel and Sleswyk, 1973), imposing surface grid (Lloyd and Morris, 1977), applying contrast interferometer (Iricibar et al., 1977), using high speed camera (Fujita and Miyazaki, 1978) and infrared camera (Louche and Chrysochoos, 2001), applying strain gauges (Zhang and Jiang, 2005), and applying optical interference (Bućko et al., 2014). The latter method has been used to investigate the plastic zones formation in thin (3.51 mm) shields made of steel C45, with the holes of 4 mm, 10 mm and 20 mm in diameter. The method of identifying plastic macro-strains is based on the optical interference phenomenon. The Lüders band propagation during the kinematically controlled tensile test is presented in Fig. 8.

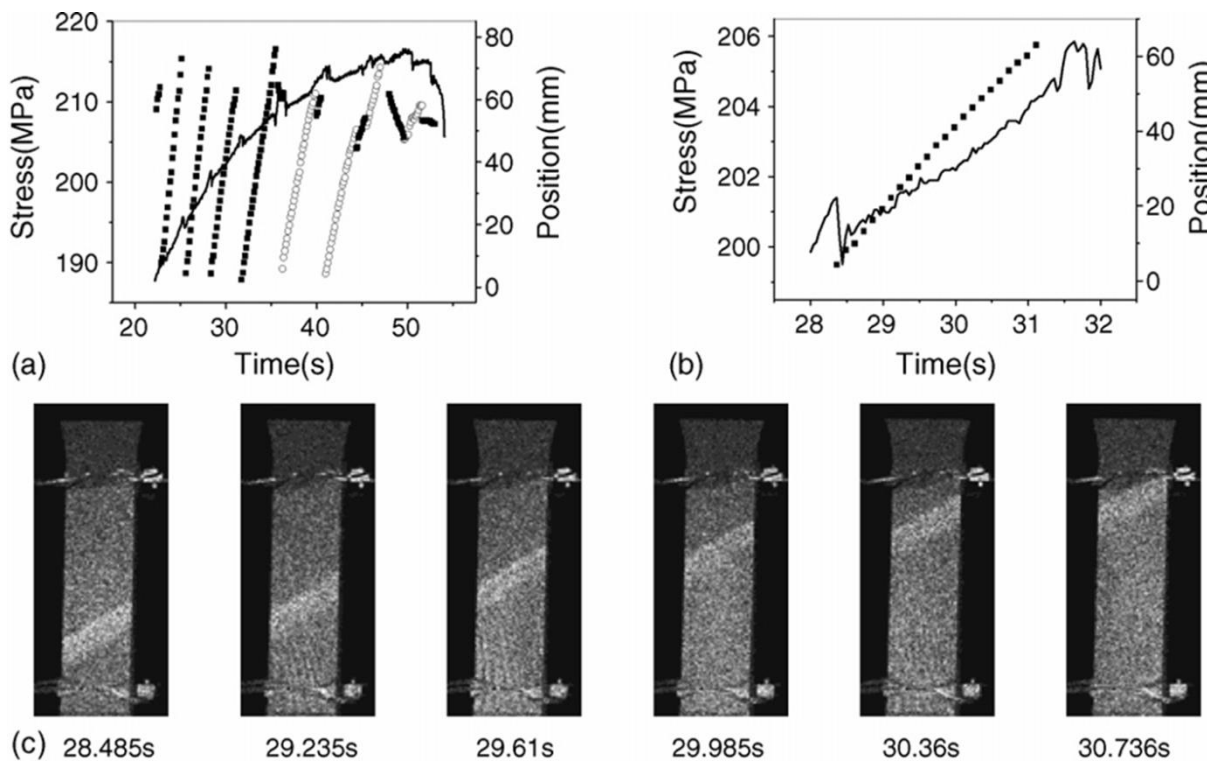


Fig. 7 Characteristics of PLC effect (type A) during kinematically controlled tensile test at room temperature: a); b) the time response of the force transducer and the position of the slip band in time; c) slip band propagation (DSPI technology) (Jiang et al., 2007)

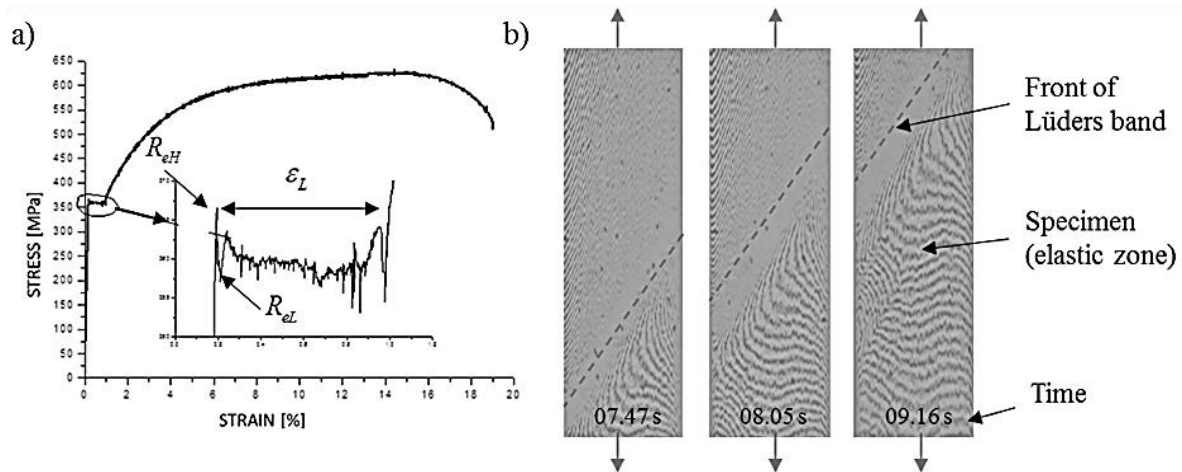


Fig. 8 Uniaxial tensile test results for C45: a) stress-strain curve (Bućko et al., 2014); b) visualisation of the slip band propagation (optical interference method) during the kinematically controlled test

Recently, in order to better understand the mechanism of nucleation of slip bands, the following techniques have been used: the AFM topographic measurement, the HR-DIC (high resolution digital image correlation) measurement together with the HR-EBSD (high-resolution electron backscatter diffraction) analysis (Jiang et al., 2015; Zhang et al., 2015; Jiang et al., 2016; Guan et al., 2017). It is worth pointing out, that after the test, the SEM (scanning electron microscope) or the TEM (transmission electron microscopy) observation is carried out.

DPF was experimentally investigated by many authors (Basinski, 1957; Reed and Mikesell, 1967; Reed and Walsh, 1988; Ogata et al., 1990; Obst and Nyilas, 1991; Reed et al., 1991; Ishikawa et al., 1993; Obst and Nyilas, 1998; Skoczeń et al., 2010; Skoczeń et al., 2014; Tabin et al., 2016, 2017). Since the discovery of DPF, a great deal of experimental data occurred, showing that this phenomenon is common and typical of plastic deformation at the temperatures near 0 K. Selected information about tensile tests of fcc materials at liquid helium (LHe) temperature (4.2 K) is presented in Table 4.

It is worth pointing out, that the strain localisation effect at extremely low temperatures was studied only by Erdman and Jahoda (1968) and Tabin et al. (2016). The experimental methods to observe slip bands during loading are limited by specific “rough” conditions. The experiments are carried out inside a double-wall cryostat, which is not transparent and usually tightly equipped with all necessary instruments. There is practically no possibility to scan the surface of the sample in the course of test. Therefore, special set-up of thermometers can be used to track the energy dissipation effect related to the evolution of a slip band. A polycrystalline copper-nickel (Cu72-Ni28) specimen was tested during a kinematically controlled tensile test by

Erdman and Jahoda (1968). The holders of the specimen were connected to heat sinks which were thermalised to 4.2 K, and which allow to transmit the mechanical load. The specimen was surrounded by low vacuum ( $1.33 \times 10^{-6}$  mbar). Its temperature was measured by means of the germanium resistance thermometers, soldered to the middle part of the specimen. A sequential propagation of slip band is traced by this method. It has been concluded, that this type of slip band can propagate through the specimen similarly to a Lüders band, and the “intermittent plastic flow” (or discontinuous plastic flow) has been referred to the adiabatic heating hypothesis developed by Basiński (1957). Erdmann and Jahoda (1964) also investigated energy dissipation during the plastic deformation. The expended mechanical work around the slip band is not entirely converted into heat, but partially stored in newly generated lattice defects. Thus, such approach can clarify the sequential propagation of slip band in the course of plastic deformation in the copper alloy (fcc material). Similar method was used independently by Tabin et al. (2016) to trace the slip band evolution during tensile test of austenitic stainless steel (304) at LHe temperature (4.2 K). The method is presented in detail in this chapter.

Table 4 Tensile tests of fcc materials at liquid helium temperature (4.2 K)

	<b>Material</b>	<b>Reference</b>	<b>Type of test</b>
Austenitic stainless steels	304L, 310L, 316LN	(Reed, Walsh, 1988)	kinematically controlled tensile test
	310S, 316LN	(Obst, Nyilas, 1991)	kinematically controlled tensile test
	304L, 316L	(Shibata et al., 2006)	kinematically controlled tensile test
	A286, 316LN, 310S, 347	(Umezawa et al., 1994)	fatigue test
	304L, 316L	(Fujii et al., 2006)	kinematically controlled tensile test
	316LN	(Skoczeń et al., 2010)	kinematically controlled tensile test
	304, 316L	(Skoczeń et al., 2014; Egner et al., 2015; Tabin et al., 2015; Tabin et al., 2017)	kinematically controlled tensile test, loading-unloading tensile test
High-Mn steels	25Mn-5Cr, 32Mn-7Cr	(Umezawa et al., 1994)	Fatigue test

High Cr-Ni steels	JN1, YUS170	(Umezawa et al., 1994)	fatigue test
	YUS170, 316LN	(Ogata et al., 1994)	tensile and fracture-toughness test
Copper, copper alloy	OFE-Cu, Cu-DHP, Cu-15Zn, Cu-3Si, Cu-5Sn, Cu-7Al-2Fe	(Reed and Mikesell, 1967)	kinematically controlled tensile test, impact test
	OFE-Cu, C-15100 (0.1% Zirconium)	(Skoczeń et al., 2010; Skoczeń et al., 2014)	kinematically controlled tensile test
	Cu+14% Al	(Dolgin and Natsik, 1991)	kinematically controlled tensile test

It is well established that the intersecting shear systems in a slip band can form very effective strain-induced nucleation places of martensitic phase in the austenitic stainless steels (Venables, 1964; Mangonon and Thomas, 1970; Suzuki et al., 1977; Brooks et al., 1979a; Fujita and Katayama, 1992; Roth et al., 2010). The mechanism by which these shear-band intersections can produce the martensitic phase has been described by Lacroisey, (1972) as well as Olson and Cohen (1975). The volume fraction of martensite induced by plastic deformation in the austenitic metals and alloys, depends on the chemical composition, the temperature and the stress state (Garion et al., 2006). In order to identify the martensite content after plastic deformation, some advanced methods were developed. Since the magnetic permeability is proportional to the volume fraction of martensite, Baudry and Pineau (1977) applied magnetic measurements and X-ray technique in order to detect and identify the martensitic phase. The magnetic permeability was also measured as a function of the tensile strain, during the kinematically controlled monotonic and cyclic tests (Suzuki et al., 1988). Moreover, formation of martensite was detected by using the transmission electron microscopy (Bayerlein et al., 1992) as well as the neutron diffraction technique (NDT) (Grosse et al., 2001). Ortwein et al., (2014, 2016) applied a feritscope to measure the martensite content in the austenitic stainless steel rods after plastic deformation in liquid nitrogen (77 K). In this case, the measurement idea is based on the fact that the martensite constitutes a ferromagnetic phase. The feritscope measures essentially the ferrite

content in the austenitic stainless steel according to the magnetic induction method, and then it is recalculated to the volume fraction of martensite. The results are presented in Fig. 9 (after Ortwein, 2015).

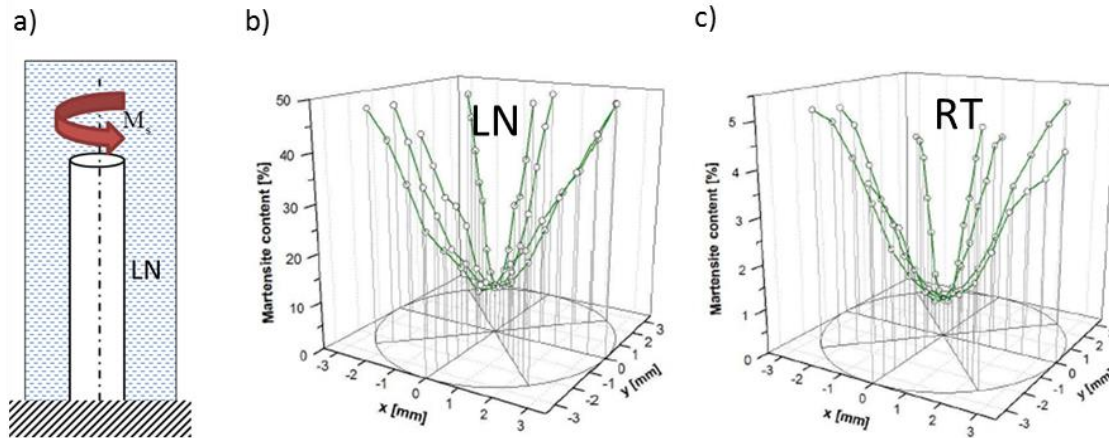


Fig. 9 a) Illustration of experimental set-up for torsion of circular cross section bars; b) martensite content for 304ss samples loaded at 77 K and c) 293 K and twisted to 870° (Ortwein, 2015)

#### 4.2. Cryogenic set-up for tensile tests

Kinematically controlled uniaxial tensile tests were carried out for 304 stainless steel plate specimens, immersed in liquid helium (4.2 K). Uniform gauge section of 304ss specimen had the length of 30 mm, and the cross section of the gauge section was of 1.5 mm × 1 mm (Fig. 10). The chemical composition of the specimen is listed in Table 5.

	Element	C	Si	Mn	P	S	Cr	Ni	Mo
304	Wt%	≤ 0.07	≤ 0.80	≤ 2.00	0.045	0.03	17.0-19.0	9.0-11.0	-

Table 5 Chemical composition of 304 austenitic stainless steel

The cryostat with the specimen and the transducers was mounted between the test machine grips. The cryogen (liquid helium) was fed to the cryostat by means of the transfer line, until the specimen with the transducers was immersed in the cryogenic medium.

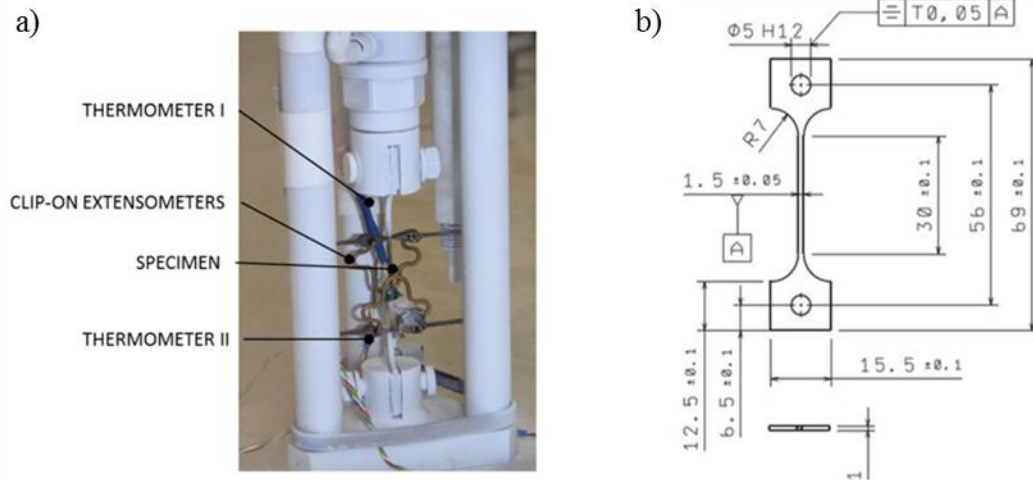


Fig. 10 Interior of the cryostat: a) the sensors with the specimen; b) dimensions of 304ss plate specimen

The level of the cryogen was indicated by a thermistor mounted inside the cryostat. Kinematically controlled tests with a crosshead velocity of 0.25–1.5 mm/min were carried out. During the test, elongation of the specimen was measured by means of the clip-on extensometers, the applied force by means of the piezoelectric transducer, mounted just behind the specimen. The temperature of the specimen during plastic deformation was measured by means of the thermistor mounted in the central part of the specimen. The general scheme of the experimental set-up, as well as the cryostat interior, are presented in Fig. 11 and Fig. 12.

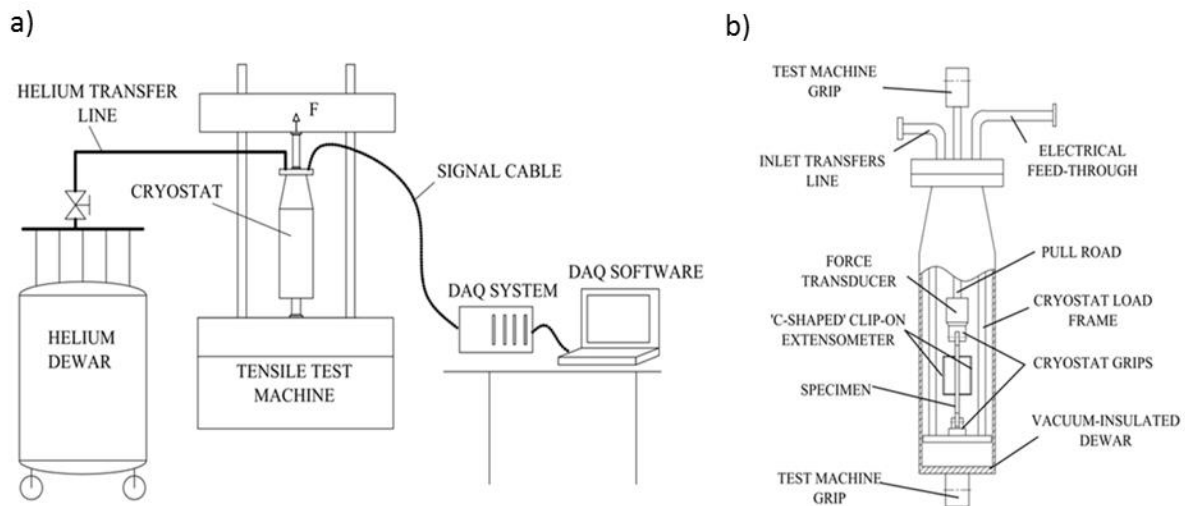


Fig. 11 a) Experimental set-up for tensile testing at extremely low temperatures; b) cryostat equipped with suitable instrumentation

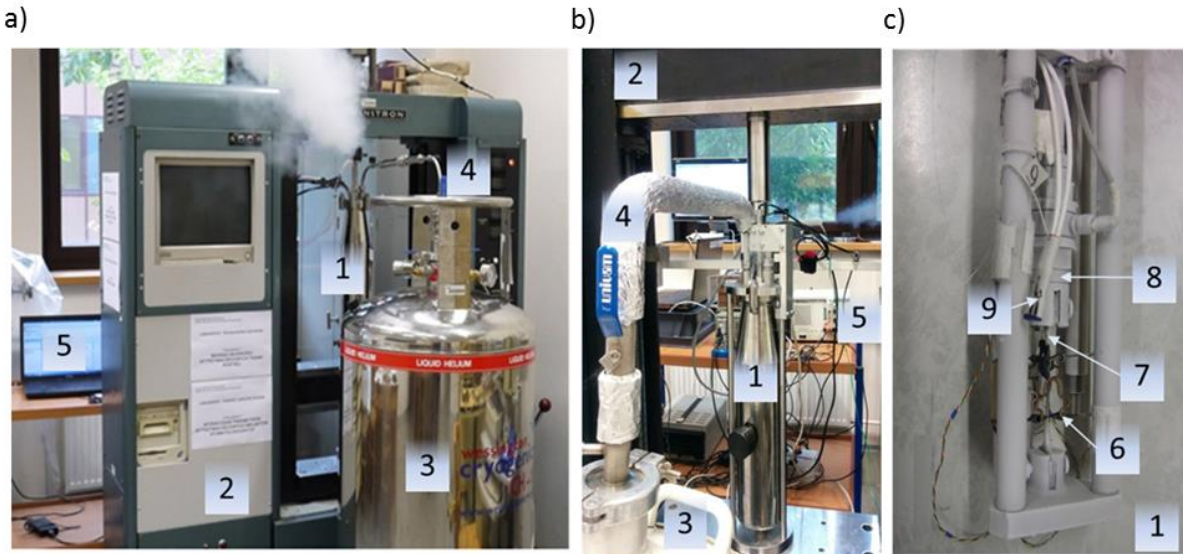


Fig. 12 Experimental set-up for: a) uniaxial tensile tests; b) combined loading; c) cryostat with equipment (1- cryostat, 2- tensile test machine, 3- cryogen dewar, 4- cryogen transfer line, 5- DAQ system, 6- clip-on extensometers, 7- specimen, 8- force transducer, 9- thermistor)

It is worth pointing out, that the clip-on extensometers are recommended by the international standards (ISO 19819, Metallic materials, Tensile Testing in Liquid Helium). Nevertheless, during the tensile test in liquid helium, the DPF can generate vibrations of the extensometers-specimen structure. It can lead to erroneous interpretation of the tensile test results. Simple approach to determine the dynamic properties of compound structure that consists of the strain gauge (clip-on extensometer) and the specimen has been discussed by Tabin and Praćik (2015). Based on this approach, suitable clip-on extensometers were selected to perform the cryogenic tensile tests at extremely low temperatures on the austenitic stainless steel specimens (cf. Section 4.3).

### 4.3. Test results

Discontinuous plastic flow (DPF) is observed in many ductile materials. The results of uniaxial tensile tests of ductile materials are presented in Fig. 13.

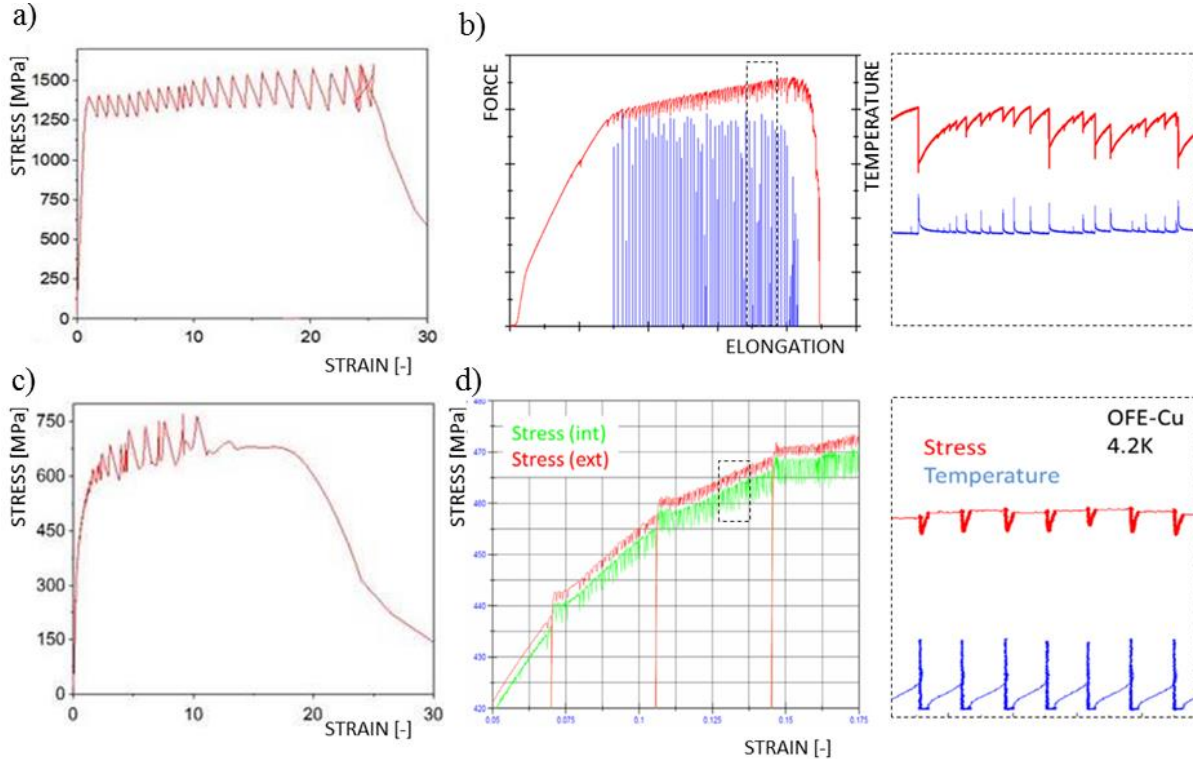


Fig. 13 Uniaxial tensile test in liquid He (4.2 K) of: a) manganese steel- JK2LB (0.003C-22Mn-13Cr-9Ni-1Mo-0.2 N); b) NbTi/Cu composite; c) Niobium-Ti6Al4V; d) OFE-Cu

The experimental analysis, presented below, was carried out for austenitic stainless steel. The uniaxial tensile test was performed by using 304 stainless steel plate specimens, immersed in liquid helium (4.2 K).

During the kinematically controlled test (cross-head velocity:  $V_c=0.5$  mm/min ), the time response of the clip-on extensometers, the force transducer and the temperature sensors was recorded (Fig. 14b). Based on these records, the stress-strain and the temperature-strain curves were generated (Fig. 14a). The position of the slip band during the uniaxial tensile test has been indicated in Fig. 14b: region 1 - the slip band propagates from one extremity of the specimen to the other, region 2 - the slip band occupies the position beyond the specimen gauge length, region 3 - the slip band occurs randomly within the entire length of the specimen.

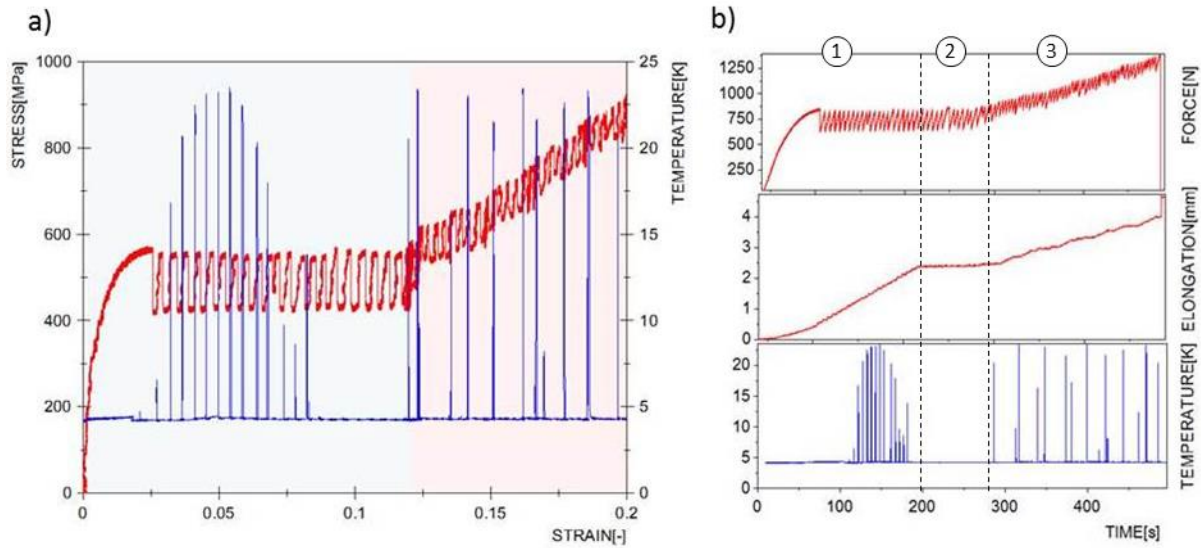


Fig. 14 Tensile test of 304 stainless steel at 4.2 K: a) stress-strain curve (red) and temperature-strain curve (blue); b) time response of the force transducer, the clip-on extensometers and the thermometer

It is worth pointing out, that in the range of near 0 K temperatures the steel specimens still preserve suitable physical and mechanical properties, including high-level ductility. Fig. 15 illustrates the fracture surface of 304 stainless steel specimen tested at 4.2 K, which is characteristic of ductile decohesion. This kind of rupture is associated with intensive plastic deformation. From the macroscopic point of view, it is easy to see that the specimen has been plastically deformed (Fig. 15a).

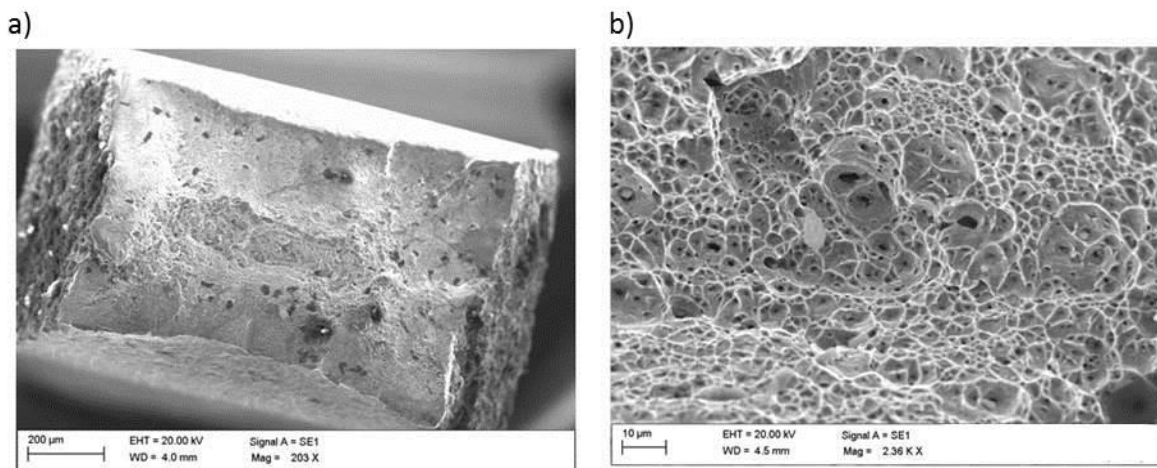


Fig. 15 SEM analysis of ductile fracture of 304 stainless steel specimen tested at 4.2 K: a) plastic deformation of specimen cross section; b) the fractured surface containing microvoids and dimples

Thermodynamic conditions of DPF are strictly linked to the so-called thermodynamic instability, related to vanishing specific heat when the temperature approaches absolute zero. The

macroscopic character of the DPF is reflected by the stress oscillations (Fig. 14a, red curve), and the heat dissipation during each serration generated in the course of slip band evolution. Such an effect is represented by the temperature-strain curve (Fig. 14a, blue curve). It is worth pointing out, that during tensile test of 304 stainless steel the plastic strain induced phase transformation has also been observed (Garion et al. 2006; Skoczen, 2007; Egner et al. 2015). The  $\gamma - \alpha'$  phase transformation is represented by the hardening effect, visible in the stress-strain curve (Fig. 14a).

#### 4.3.1 Verification of the DPF nature

The thermal origin of DPF was first suggested by Basinski (1957). He attributed the load drops to the thermodynamic properties of materials at very low temperatures, represented by the specific heat and the thermal conductivity tending to zero (thermodynamic instability). Basinski developed the adiabatic heating hypothesis. He assumed that any sufficiently fast dissipative process at extremely low temperatures leads to increase of local temperature (the plastic work is converted to heat) and, consequently, to a rapid decrease of the flow stress. Therefore, it explains the existence of DPF at a temperature  $T < T_{cr}$ . The concept of thermal instability has been subsequently developed by Estrin, Kubin (1980, 1988), Estrin, Tangri (1981), Shibata (1988), Burns (1994), Zeiser, Haehner (1997). The evidence on the thermal nature of instability is given by the experiments in which deformation jumps were initiated by heat pulses (Dolgin, 1988). In the alloy Cu + 14 at.% Al heating was induced by passing current pulses through the samples. In the superconducting polycrystalline Nb at 4.2 K, pulsed heating of about 50  $\mu$ s up to 12-13 K took place during the magnetic flux jumps. In both cases, it was possible to initiate the process which was completely equivalent to the deformation jump. Nevertheless, it should be noted that the heating of the sample in the course of a jump is not in itself an evidence of the thermal origin of instability, but it is only a consequence of energy dissipation during plastic deformation (Dolgin and Natsik, 1991).

Seeger (1957) suggested that during plastic deformation dislocation piles-up at the material barriers, which cannot be overcome by thermally activated cross slip since the temperature is low, but by the force due to the stress concentration at the head of dislocation pile-up. According to the other authors (Wessel, 1957; Dolgin and Natsik, 1991), high flow stresses at low temperatures can promote avalanche multiplication of mobile dislocations.

Such an approach was developed, subsequently, by Obst and Nyilas (1991, 1998). The Authors point out that the pile-ups of dislocations on the internal barriers (Lomer-Cottrell locks, Cottrell atmospheres, Suzuki locks, groups of interstitial atoms, dislocation forest, non-metallic inclusions etc.) in the lattice may give rise to stress concentrations of the order of theoretical shear strength. In their view, the load drops are due to a catastrophic process consisting in spontaneous generation of dislocations as soon as the internal barriers are broken. According to Obst and Nyilas, the plastic flow instability is of mechanical nature.

Both the adiabatic heating hypothesis presented by Basinski (1957), and the mechanical approach developed by Seeger (1957) and Obst and Nyilas (1991, 1998) reflect very complex nature of the plastic flow instabilities that occur at extremely low temperatures. An original approach to explain the intermittent plastic flow at extremely low temperatures has been developed by Skoczeń et al. (2008, 2010, 2014). The approach is based on decomposition of single serration into four stages and constitutive description of each stage of the process. This physically based thermo-mechanical model takes into account thermodynamic instability, dislocation dynamics and thermally activated relaxation processes. Moreover, the correct sequence of phenomena has been experimentally confirmed, including dissipation of energy due to inelastic deformation and conversion of plastic power to heat, resulting in the occurrence of temperature spikes. It is the first coupled, physically based, multiscale constitutive model that explains correctly thermo-mechanical nature of the DPF.

In order to verify the origin of DPF, a unique experiment has been carried out. The nature of DPF was experimentally confirmed by means of the tensile tests on steel specimens, performed at 4.2 K. The relevant kinematically controlled tensile test consists essentially of three stages (Fig. 16b): 1 - uniaxial tensile test with constant speed of the crosshead, 2 - halting the crosshead, 3 - continuation of the test with constant speed. The test results are presented in Fig. 16.

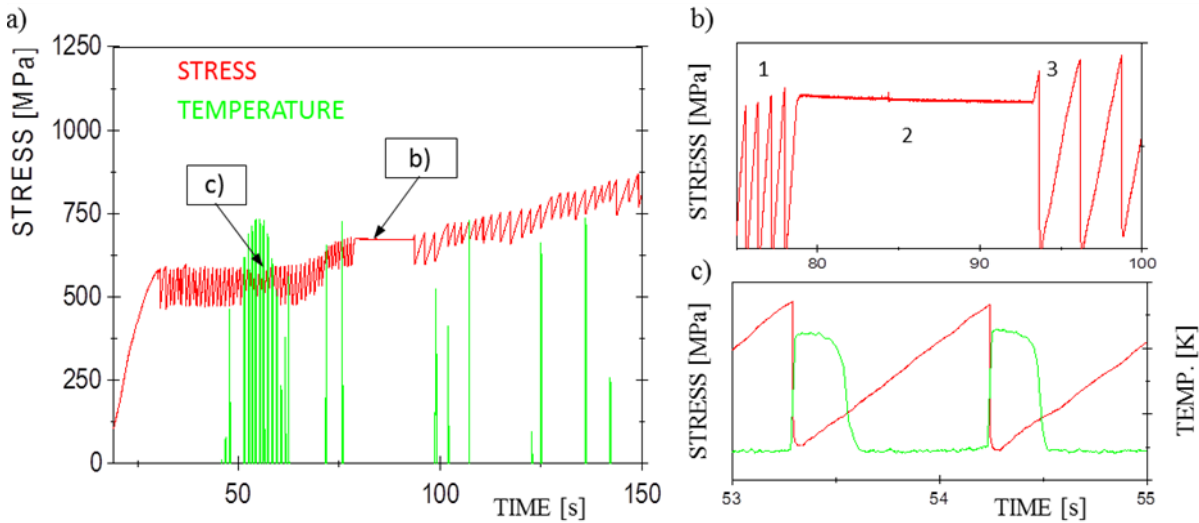


Fig. 16 Verification of DPF: a) time response of force transducer (red) and temperature sensor (green); b) three stages of tensile test: 1 - uniaxial tensile test with constant speed of crosshead, 2 - halting the crosshead, 3 - continuation of the test with constant speed; c) time response for single serration

The load applied to the stainless steel specimen is measured directly on the sample using a force transducer (e.g. piezoelectric sensor). Time response of the force transducer (red) during three stages of serration is presented in Fig. 16b. It seems that time response of the force transducer after stage 2 has similar form to previous serration, despite the fact that the temperature of the specimen dropped to 4.2 K. It confirms the mechanical nature of DPF. Moreover, based on the response of temperature and force it is clear that at first, the abrupt drop of stress (red) occurs, and then the temperature rapidly increases (green) (Fig. 16c). Another example is presented in Fig. 17. The measurements carried out by using the internal load cell clearly show, that the drop of stress precedes the increase of temperature and the thermodynamic response is secondary w.r.t. the mechanical effect (Skoczeń et al., 2010). Obviously, the time response of the temperature sensor should be taken into account. It is less than 15 ms at 4.2 K for Cernox CX-SD (the temperature transducer used in the test). Thus, it is significantly below the difference of response between the force and the temperature transducers (see Fig. 17).

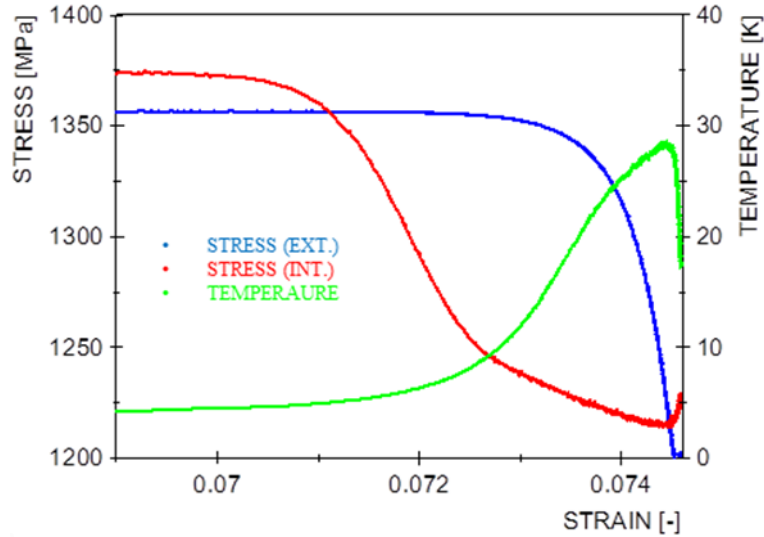


Fig. 17 Single serration for 316L - the external load cell (blue), the internal load cell (red), the temperature (green)

Based on the presented analysis, the mechanical nature of DPF has been confirmed. Moreover, it has been confirmed that massive failure of lattice barriers is at the origin of localised heating observed during the tensile test. Such thermo-mechanical approach was described by Skoczeń (2008), Skoczeń et al. (2010, 2014, 2015), and Tabin et al. (2016, 2017). It is worth pointing out, that the DPF is also coupled with other phenomena that occur at extremely low temperatures in the material, i.e. the strain induced phase transformation or the damage evolution. The appearance and intensity of these phenomena depends on test conditions, chemical composition of the material, and evolution of the strain and the stress fields.

#### 4.3.2 Strain rate effect

A distinctive feature of DPF is that it occurs at the temperatures below a critical value  $T_1$  or  $T_0$ , depending on tested material, for example,  $T_1 < 30 K$  for the austenitic stainless steel. Thus, DPF takes place within a certain range of temperature, as well as for certain range of strain rate. Similar effect is observed for the PLC, where the band types have particular locations in the strain rate-temperature plots, as shown in Fig. 19.

The dependence of the strain rate on plastic flow in OFE-Cu is illustrated in Fig. 20 (Skoczeń et al., 2014; Marcinek, 2016). The uniaxial tensile test was carried out for three different strain rates, from  $1.5 \times 10^{-3}$  to  $1.5 \times 10^{-1} s^{-1}$ . The transition from serrated to smooth flow

is observed for  $1.5 \times 10^{-1} s^{-1}$ . The specimen temperature increases to 20 K and approaches temperature  $T_1$  for OFE-Cu.

It is worth pointing out, that during the kinematically controlled test with a constant velocity of the cross-head, the initially observed serration (stress oscillation as a function of strain) may be suppressed, when the energy dissipation increases gradually and the local temperature of the specimen exceeds  $T_1$  (smooth plastic flow occurs). Such a phenomenon is observed during the kinematically controlled test of Niobium-Ti6Al4V alloy at the liquid helium temperature, Fig. 18.

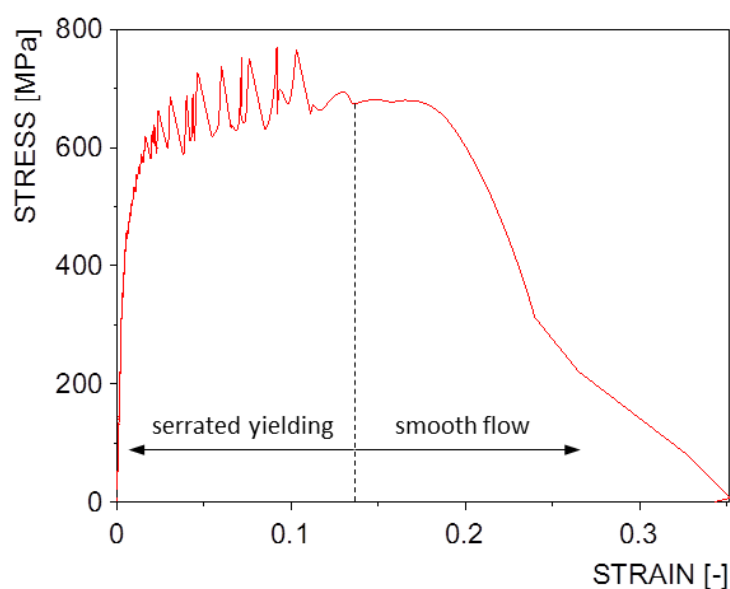


Fig. 18 Vanishing serration in Niobium-Ti6Al4V specimen during a kinematically controlled test at 4.2 K

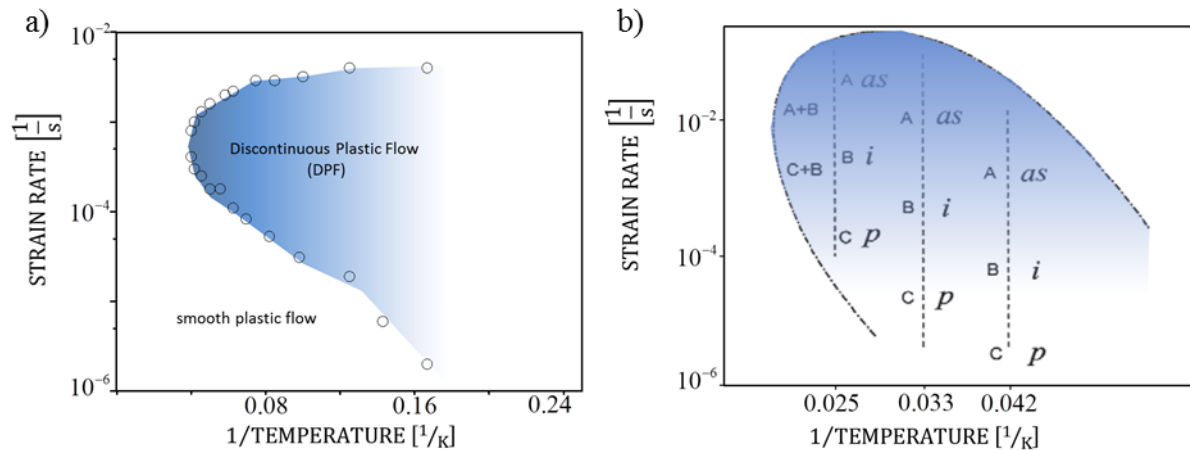


Fig. 19 Temperature-strain rate diagram a) with DPF limits in Cu + 14 at.% Al (Dolgin and Natsik, 1991; Zaiser and Hähner, 1997); b) in Al-Mg alloy; band types (A, B, C) corresponding to the PLC effect: 'i', 'p' and 'as' refer to the crystal type of the sample (Lebyodkin et al., 1997; Ahmet, 2011)

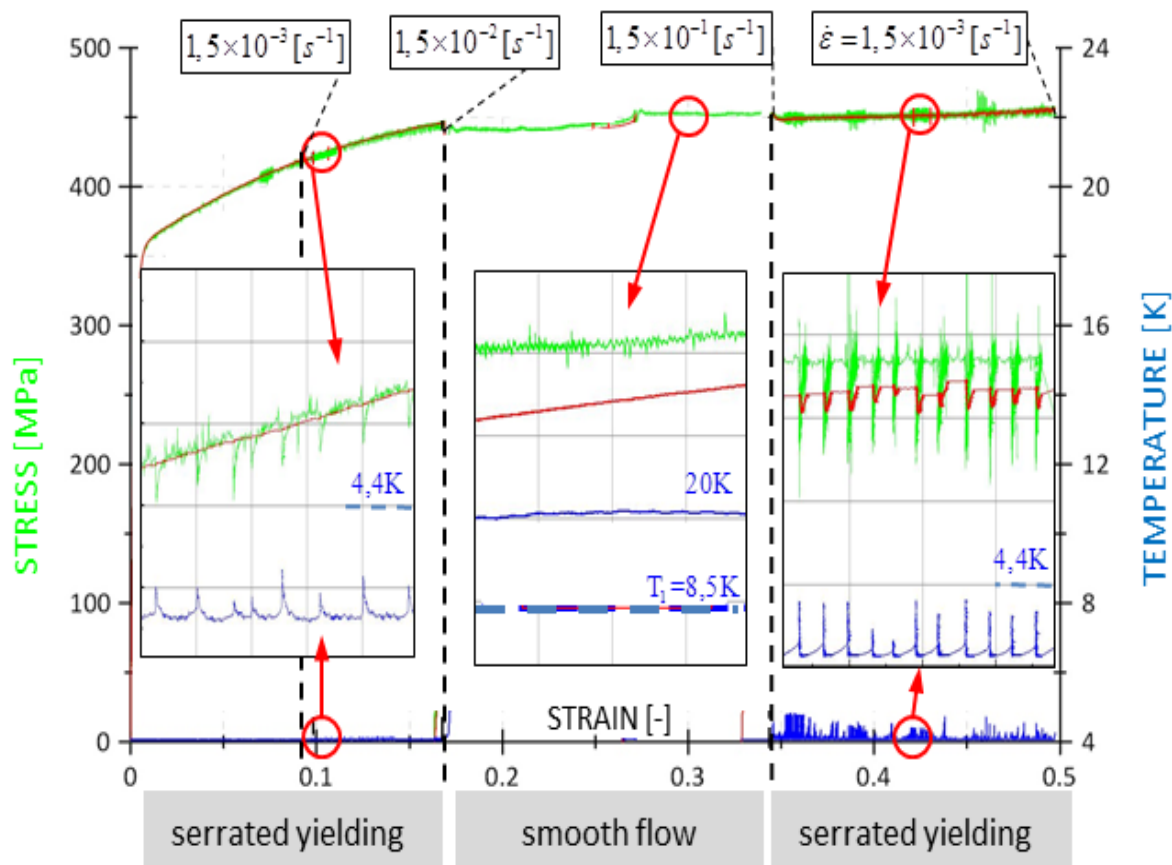


Fig. 20 Effect of strain rate on activation of serrated yielding for OFE Cu; the strain rate program  $1,5 \times 10^{-3} s^{-1} \rightarrow 1,5 \times 10^{-2} s^{-1} \rightarrow 1,5 \times 10^{-1} s^{-1} \rightarrow 1,5 \times 10^{-3} s^{-1}$ ; transition temperature is equal to 8.5 K (temperature evolution is reflected by the blue curve), (Marcinek, 2009)

### 4.3.3 Strain localisation effect during DPF

The stress-strain and the temperature-strain characteristics indicate the nature of slip band propagation during a cryogenic tensile test performed on 304 stainless steel. Analyzing the test results, it is worth focusing at first on the temperature distribution within the range without visible hardening influence (region 1, Fig. 14b). The profile of the temperature-strain curve may suggest the nature of the slip band evolution during the tensile test in liquid He. The temperature distribution in this range has a regular form (the comb-like profile), which occurs when the slip band propagates during plastic straining from one extremity of the specimen to the other, and from serration to serration. It is worth pointing out, that during the period from 190 to 285 s (region 2, Fig. 14b), there is no record of temperature spikes in view of the fact, that the slip band holds the position beyond the specimen gauge length (see Fig. 14b and Fig. 23), thereby beyond the sensing range of the temperature sensor. Nevertheless, during this period the serrations occur (see time response of the force transducer). The temperature distribution within the hardening range (region 3, Fig. 14b) is random, which reflects irregular and constrained motion of the slip bands, which is associated with the interaction of collective and massive breaks through the lattice barriers, and nucleation of secondary (martensitic) phase. In other words, the initially observed regular “travelling” slip band is blocked by nucleation of the martensite, whereas, the new slip bands occur randomly within the specimen. These postulates can be confirmed by means of the analysis of time response of temperature sensors and extensometers, recorded during the test (Fig. 21b and c). Based on this analysis, it is possible to determine the temporal and the spatial characteristics of the slip band.

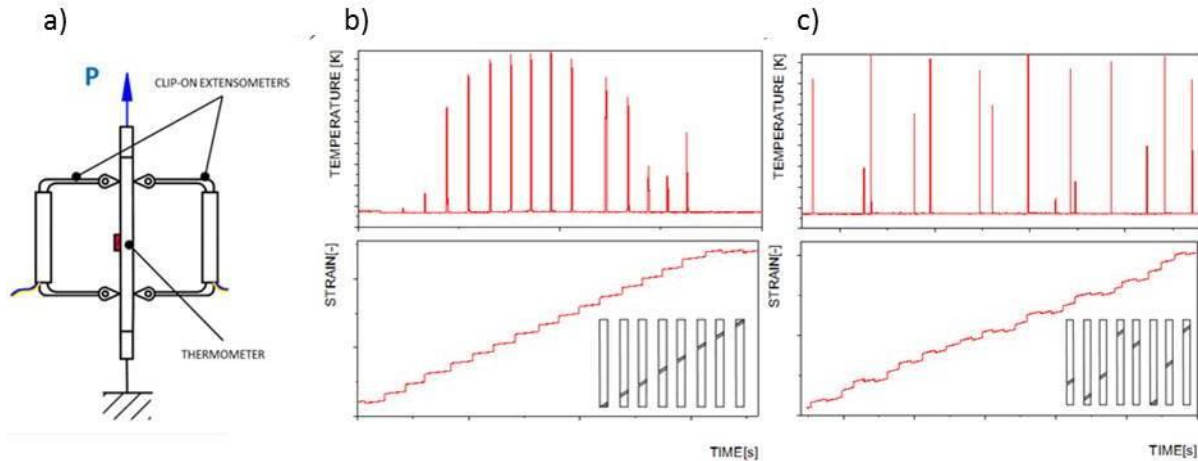


Fig. 21 Cryogenic tensile test of 304 stainless steel specimen: a) experimental set-up; b) temperature and strain–region without phase transformation; c) temperature and strain - region including the phase transformation process

Looking at the inserted bars in Fig. 21b, it is found that the plastic deformation was first initiated in a local area near the bottom part of the gauge section, and has spread out over the whole gauge section (Fig. 21a). Temperature distribution, corresponding to a slip band evolving regularly with constant velocity, is illustrated in Fig. 22.

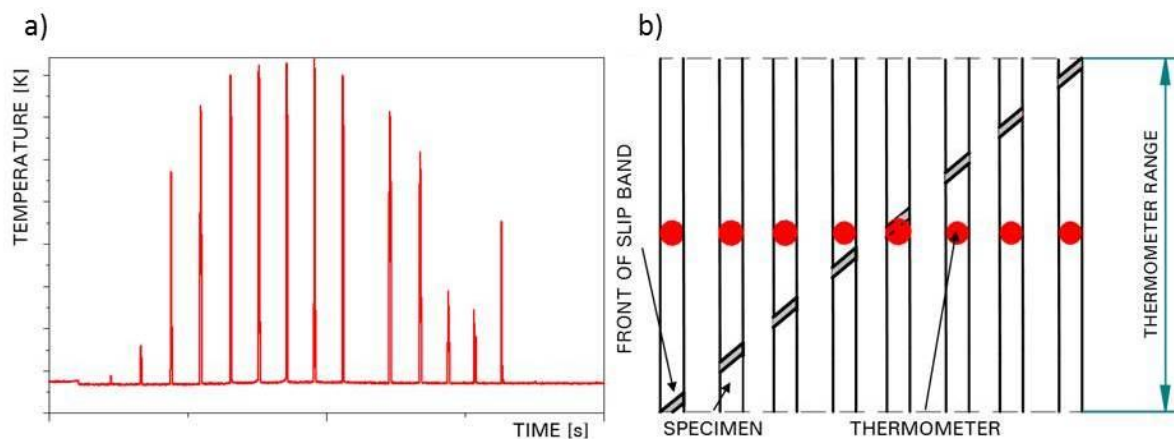


Fig. 22 a) Time response of the thermometer during the cryogenic tensile test in liquid He (the comb-like profile of temperature); b) illustration of the slip band propagation

When the slip band approaches the position of the thermometer, the temperature amplitude (spike) related to the serrations increases. Maximum temperature is registered when the slip band occurs under the thermometer. After that, the temperature recorded by the sensor decreases, until the slip band falls outside the measurement range of the thermometer. For what concerns the hardening range, the temperature distribution shows a random pattern (Fig. 21c). It is worth pointing out, that the time response of the extensometers during the test allows us to

localise the slip band. The behaviour of the extensometer, when the slip band occurs between its arms or beyond them is different, which is shown in Fig. 23. A drop of the strain signal is generated by the slip band that occurs outside the extensometer arms (outside the gauge length). During the period from 190 to 285 s, there is no recorded global increase of elongation in view of the fact, that the slip band occurs outside the gauge length (region 2, Fig. 14b, Fig. 23).

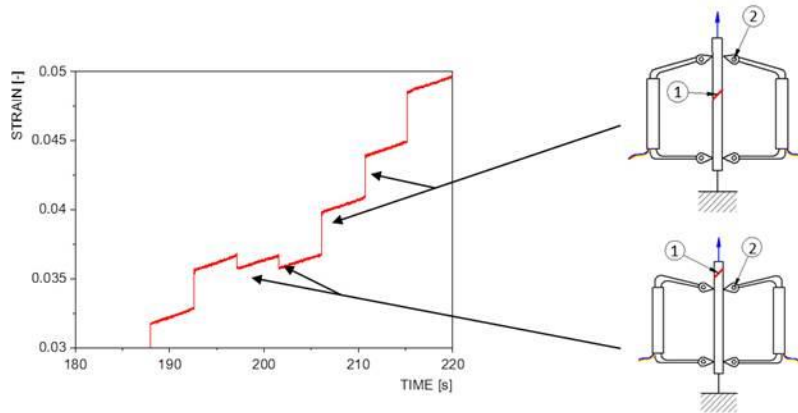


Fig. 23 Time response of the clip-on extensometers as a function of slip band localisation during the cryogenic tensile test in liquid He

During the tensile test of 304 stainless steel, the first slip band occurred near one of two grips, beyond the extensometer arms, which is indicated by drop of strain. Then the slip band propagated across the extensometer arms, and the next drop of strain is recorded when the slip band is again beyond the extensometer arms, near the second grip. On the other hand, whenever the hardening effect is observed the slip band occurs irregularly (Fig. 21c). Both types of time response of the thermometer and the clip-on extensometers are consistent, and confirm the nature of slip band propagation in 304 stainless steel in liquid He. In order to determine the parameters of the slip band evolution, an individual experiment was carried out.

#### 4.3.4 Experimental set-up to identify parameters of slip band propagation

In order to determine the nucleation spot and the direction of slip band(s) evolution, two thermometers were bonded on 304 stainless steel specimen surface: the thermometer II (red) was bonded beyond the bottom grip (outside the gauge length), and the thermometer I (green) was bonded in the middle of the gauge length. The distance between the thermometers is equal to 16 mm. A kinematically controlled tensile test (crosshead speed:  $V_c=0.5$  mm/min ) was carried out in liquid He. Both clip-on extensometers were used. The experimental set-up is presented in Fig. 24.

Based on the time response of the thermometers and the clip-on extensometers, the parameters of slip bands propagation for two distinct ranges: without and with phase transformation were determined. In particular, the average velocity of slip bands within the range without phase transformation (hardening) were calculated. Fig. 25a illustrates time response of two thermometers: the red one, bonded near the bottom grip, and the green one, bonded in the middle of the gauge length. Also, the time derivative of response of extensometers (strain rate) is included in Fig. 25b.

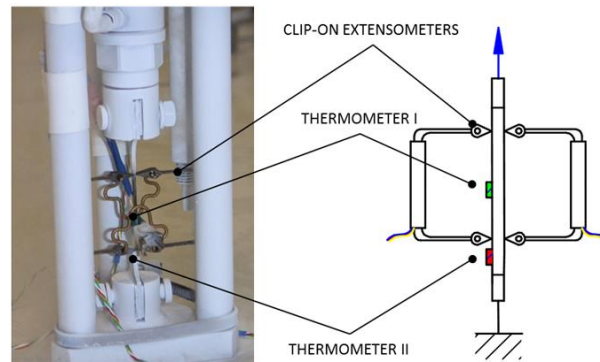


Fig. 24 Experimental set-up for tracking slip band evolution during the uniaxial tensile test in liquid He

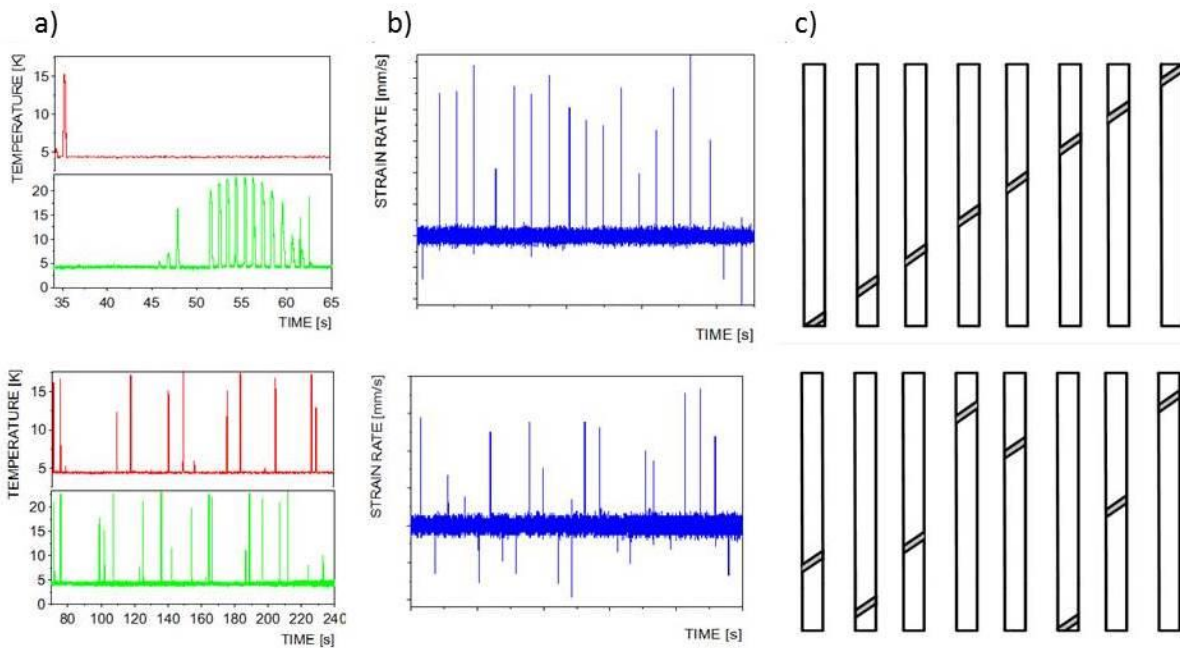


Fig. 25 Visualization of slip band evolution in 304 stainless steel: a) regular slip band propagation (no hardening); b) irregular slip band propagation (phase transformation induced hardening)

Time response of extensometers during the test becomes an important source of information (Fig. 21, Fig. 25). If a slip band occurs outside the gauge length, a drop of signal

generated by the extensometers is observed. Therefore, the time derivative of the signal resembles impulse function with negative value (first peak in the blue curve). On the other hand, when a slip band occurs between the extensometer arms, the time derivative of the signal becomes impulse function with a positive value. Based on the response of thermometers, one can deduce that during the tensile test the slip band occurs near the red thermometer and then propagates towards the green one (in the middle of the specimen). When the thermometer I (green) is reached by the slip band, the measured amplitudes of temperature oscillations (related to serrations) substantially increase. The maximum occurs when the slip band reaches the position of the thermometer. Thereafter, as a consequence of the slip band propagation, the time response of thermometer I decreases, until the slip band leaves the measurement range of thermometer I. On the other hand, the thermometer II (red one) was bonded outside the gauge length. Therefore, the slip band recorded by thermometer II causes simultaneously drop of the extensometer signal. Next, the same slip band occurs within the gauge length, and propagates across the gauge length in the proximity of thermometer I. When the slip band falls outside the gauge length, the negative peak is again observed in the rate of elongation chart. The slip band propagation in the range without hardening has a regular form, and the slip band during the test propagates from grip to grip. Hardening caused by the fcc-bcc phase transformation affects the slip band propagation considerably. In particular, the slip bands occur at random places, and very soon are blocked by the obstacles (secondary phase). Therefore, the time response of thermometers does not have a regular pattern. Also, the strain rate suggests that the slip bands occur at random places, within or outside the gauge length.

The experimental set-up presented in Fig. 24 allows determining the basic parameters of the slip band propagation under the test conditions initially specified (cross-head velocity  $V_c = 0.5 \text{ mm/min}$ ). The distance between two thermometers is equal to  $l_r = 16 \text{ mm}$ . Based on the time response of both thermometers, it is possible to determine the time increment when the slip band occurs under the thermometer II and, later on, under the thermometer I (the test conditions are fixed). Therefore, the average slip band velocity is equal to  $V_{sb} = 48.5 \text{ mm/min}$ , when no phase transformation occurs. The basic parameters of the slip band propagation during the kinematically controlled uniaxial tensile test of 304ss at 4.2 K are presented in Table 6.

Similar effect was observed by Louche and Chrysochoos (2001) during the uniaxial tensile test of S355MC steel at room temperature. Single band, propagating at constant velocity, was observed.

In view of the foregoing analysis, a visualisation of slip band propagation during DPF in 304ss loaded at 4.2 K is presented in Fig. 26. Based on this experimental analysis, the thermodynamic model of “travelling” slip band during DPF has been developed.

Table 6 Experimentally identified parameters of slip band propagation

Parameter	Value
Type of test	kinematically controlled
$l_T$ distance between thermometers	16 mm
$V_c$ cross-head velocity	$0.5 \frac{\text{mm}}{\text{min}}$
$V_{sb}$ slip band velocity	$48.5 \frac{\text{mm}}{\text{min}}$
$f_{serr}$ serration frequency	1 Hz

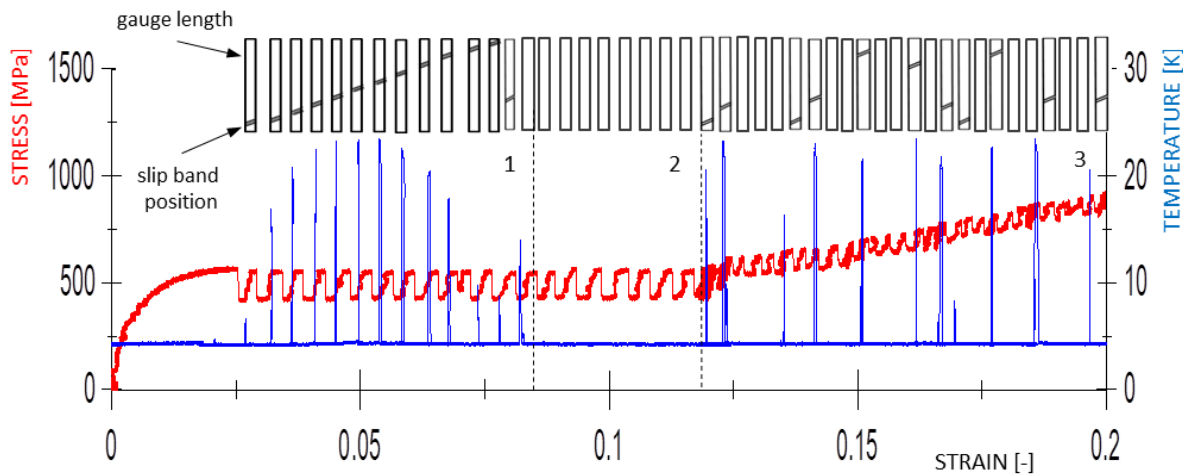


Fig. 26 Tensile test results: stress-strain curve (red) and temperature-strain curve (blue) for 304 stainless steel at 4.2 K; visualization of slip band evolution along the gauge length of the specimen

### 4.3.5 Dynamic behaviour of extensometer-specimen structure during DPF

It is well known that the specimen clamping system, shape and dimensions of the specimens, rigidity of the testing machine, the parameters of the test (crosshead speed, etc.), and the properties of tested materials can influence the accuracy of measurements (Davis, 2014). All too often, however, the researchers do not pay sufficient attention to the complex interactions between the specimens and the measuring apparatus. It can lead to erroneous interpretation of the tensile test results.

Fig. 27 presents the stress-strain curve for 316LN stainless steel tested at 4.2 K (sampling frequency  $f_s = 4800 \text{ Hz}$ ). Each serration includes the artefact reflected by the horizontal oscillation of strain. It is worth pointing out, that DPF has dynamic character and may generate oscillations of the extensometer-specimen structure. Understanding the reason of dynamic behaviour of “clip-on extensometer”–specimen structure, is crucial for the appropriate interpretation of time response of strain, or the stress–strain curve.

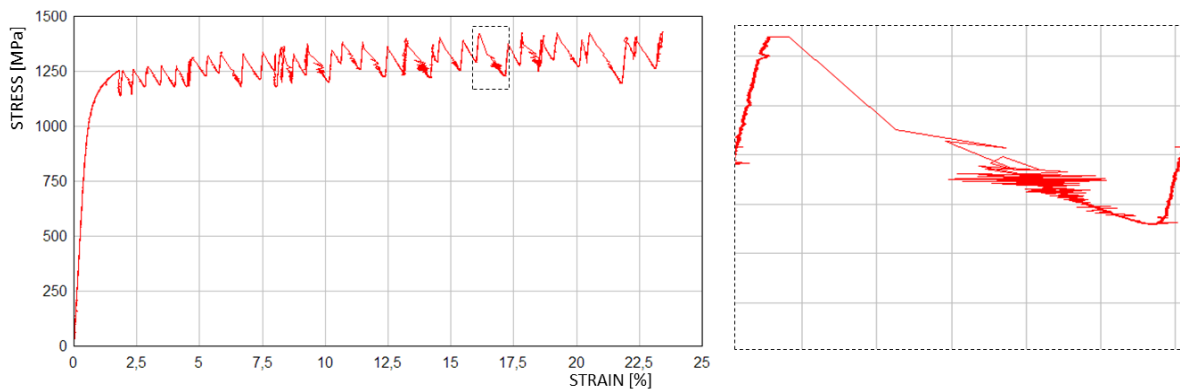


Fig. 27 Stress-strain curve for 316LN stainless steel tested in LHe ( $T=4.2 \text{ K}$ ,  $f_s=4800 \text{ Hz}$ )

Fig. 28 presents time response of two types of extensometers during single serration at similar strain levels. The experimental results indicate that the shape of the extensometers (“C-shaped” vs. “W-shaped”) and their stiffness, significantly influence the natural frequency and the damping ratio of the structure. The “W-shaped” extensometers are more susceptible to dynamic nature of DPF according to the extra frame added between the arms of the extensometer. The added frame extends the measurement range, however, it reduces simultaneously the extensometers stiffness and their damping ratio.

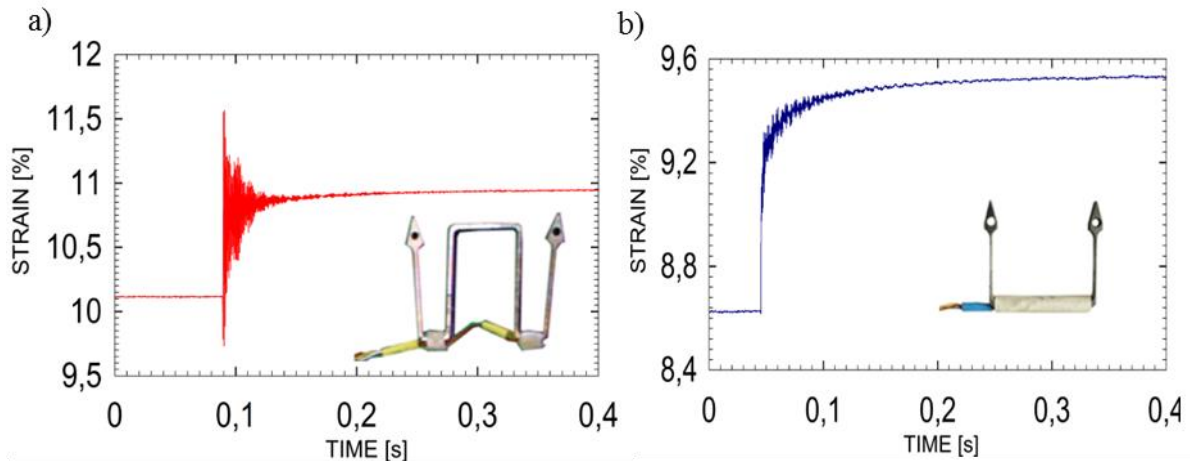


Fig. 28 Part of the strain vs. time curve: differently shaped extensometers vibrate differently during kinematically controlled tensile tests in liquid helium (4.2 K); a) vibrations of “W-shaped” extensometer; b) vibrations of “C-shape” extensometer during single serration

Tabin and Pracik (2015) proposed simple approach to determine dynamic properties of compound structure that consists of strain gauge clip-on extensometers (dual extensometers) and the specimen. Simple and effective method of establishing the modal frequency and modal damping of these structures has been proposed. Furthermore, external sources of vibrations that influence strain measurements, as well as the measurement paths to identify the magnitude of these influences have been discussed.

Knowledge about the natural vibration spectrum of the “clip-on extensometer”–specimen structure obtained in the course of tensile tests (when the plastic instability of testing materials occurs), together with its natural frequency spectrum (obtained without tension, with impact excitation applied) – makes it possible to estimate the influence of the natural vibrations of extensometer on the tensile test results. Modal parameters calculated this way are the basis for building a mathematical model of the phenomena that occur both in the testing specimen, and in the measurement system. The model consists of discrete masses, springs and visco-dampers. Furthermore, it includes experimentally identified functions (complex data for extensometer-specimen structure), registered during the tensile test. The model shown in Fig. 29 will be applied to investigate the influence of different parameters on dynamic characteristics of the phenomena that occur both in the testing specimen, and in the measurement system during the tensile tests.

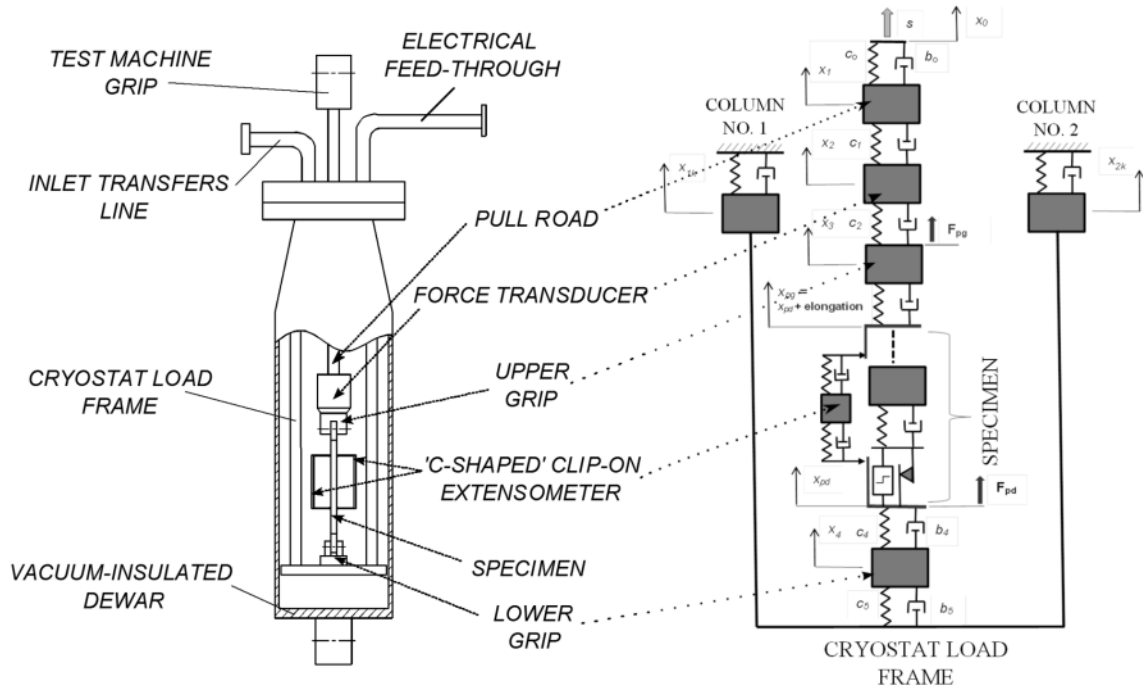


Fig. 29 The cryostat structure, the cross section and the scheme of the model built for simulation (Tabin et al., 2015)

In the case of uniaxial tensile tests of the austenitic stainless steel specimen at 4.2 K, based on the presented approach, suitable clip-on extensometers were selected (“C-shaped”).

## Chapter 5

# Modelling of strain localisation during the DPF

Experimental identification of the strain localisation during discontinuous plastic flow (DPF) at 4.2 K has been carried out. It can be concluded, that the plastic flow instability consists in a strong strain localisation in the form of slip band, “travelling” across the gauge length of the sample. Moreover, the  $\gamma-\alpha'$  phase transformation observed during the DPF makes the nucleation of slip bands, and their free glide, randomly redistributed over the gauge length of the specimen. The propagation of slip bands is reflected by the Dirac-like temperature spikes recorded during the uniaxial tensile test.

In this chapter, the constitutive models of DPF and phase transformation, as well as the thermodynamic model of “travelling“ slip bands, are presented. The measured profile of the temperature spikes is explained by building a model of “travelling” slip band, carrying the representative volume element (RVE), and the fixed thermometer located in the middle of the sample. Thermodynamic problem of heat diffusion in the sample is solved, using the Green-like solution of heat diffusion equation. Moreover, the physically based model of the phase transformation affected DPF allows reproducing the experimentally observed serrations during the plastic deformation.

## 5.1. Constitutive Model of discontinuous plastic flow

### 5.1.1. Kinetics of DPF

The main aim of the Thesis is to predict the macroscopic mechanical behaviour of the plastic materials at the cryogenic temperatures, using the physically based models. The DPF model, presented below, has two major features: the model parameters are physically meaningful, and their values are found by fitting to experimentally determined properties of tested materials. Discontinuous plastic flow (DPF) is characteristic for face centered cubic (fcc) metals and alloys (such as copper, copper alloys or stainless steel) deformed at near 0 K temperature. Macroscopically, DPF is reflected by the stress oscillations as a function of strain (Fig. 30a). DPF occurs below a specific threshold temperature:  $T_1$  for the low stacking fault energy (LSFE) materials, or  $T_0$  for the high stacking fault energy (HSFE) materials. Both temperatures are material parameters, and represent transition from the screw to the edge dislocations mode (Obst and Nyilas, 1991). According to Seeger (1957), type of dislocations in the fcc materials may change at very low temperatures because of lack of thermal energy necessary for generation and motion of dislocations. It is worth pointing out, that the edge dislocations move at lower stress than the screw ones, and cannot leave the lattice barriers by simple cross-slip at extremely low temperatures. Therefore, plastic flow in the low excited lattice is related to the presence of edge dislocations and their response to the applied stress, whereas at the ambient temperature the screw dislocations mode is dominant. The consequence of change of the dislocations mode consists in the fact, that the temperature dependence of the yield stress changes at  $T_0$  or  $T_1$  (see Fig. 30c). The relation between the yield stress and the temperature for different types of materials, such as: Al Mg 4.5 Mn, Cu 63 Zn 37, 310S, etc., was investigated by Obst and Nyilas (1991). Fig. 30c presents such a relation for the austenitic stainless steel 316LN. Below the specific temperature  $T_1$ , the edge dislocations can form dislocation pile-ups at the lattice barriers (including: Lomer-Cottrell locks, Cottrell atmospheres, Suzuki locks, groups of interstitial atoms, dislocation forest, non-metallic inclusions etc.). Collective and massive failure of these barriers is reflected in the stress-strain curve by an abrupt drop of the stress (Fig. 30a, b).

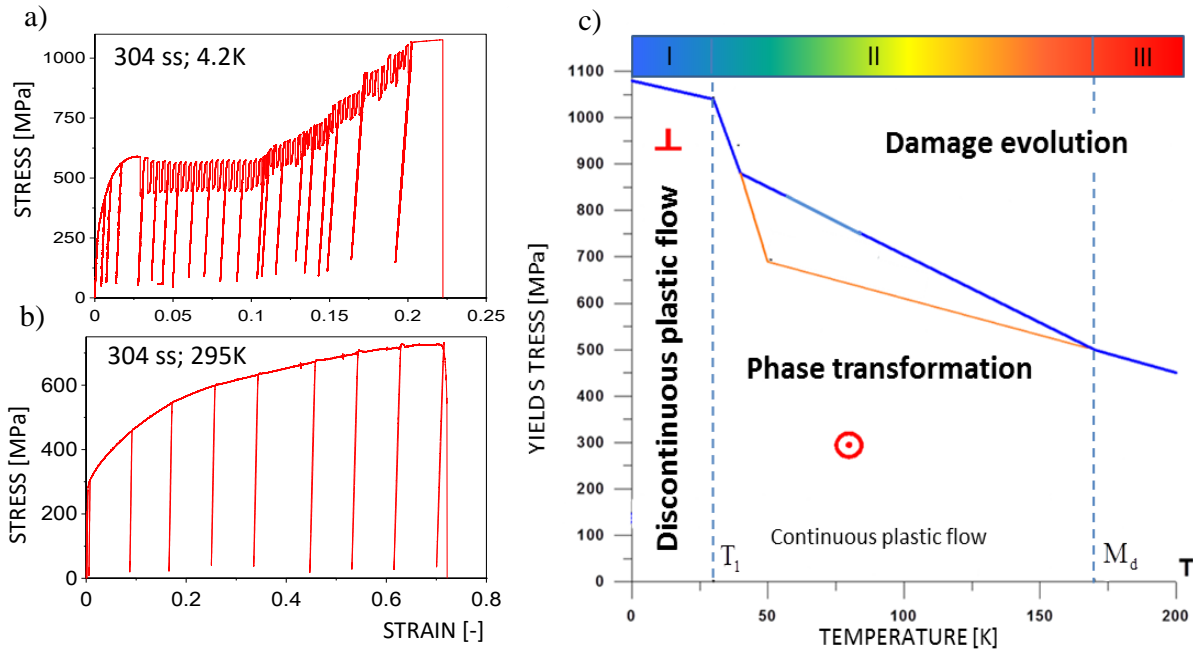


Fig. 30 Representation of the flow stress-temperature dependence for the austenitic stainless steels: stress-strain curve for 304ss a) at liquid helium temperature (4.2 K); b) at room temperature (295 K); c) yield point against temperature for 316LN, and three domains of response of the austenitic stainless steels: discontinuous plastic flow, strain-induced phase transformation and damage evolution

In the fcc metals and alloys at the temperatures near 0 K, edge dislocations are often dissociated in the slip plane into two Shockley partial dislocations, bounding the stacking fault ribbon (Fig. 31a).

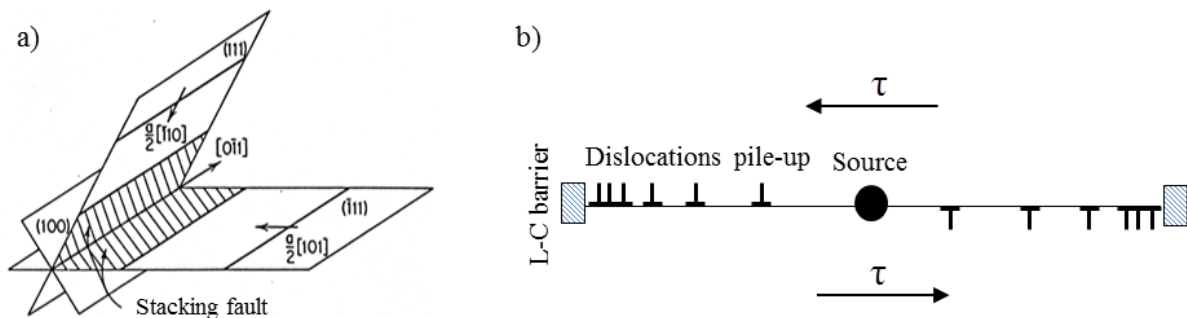


Fig. 31 a) Formation of the Lomer-Cottrell lock by reaction of two glissile dissociated Shockley partial dislocations; b) edge dislocations pile-up during DPF at a lattice barrier

If the dislocations meet at the line of intersection of the two planes, the leading partials repel or attract each other. By analogy with a carpet on the stairs, it is also called a “stair-rod” dislocation. The stair-rod partial therefore exerts a repulsive force on two Shockley partials, and all three partial dislocations form a stable, sessile arrangement. It acts as a barrier for free glide of

further dislocations on two planes, and is known as a Lomer-Cottrell lock (Hull and Bacon, 2011a).

The back stresses of the piled-up groups are supposed to block the movement of newly created dislocations. The local shear stress at the head of the dislocation pile-up, proportional to the number of dislocation in the pile-up, may reach the level of cohesive strength and the Lomer-Cottrell barrier may collapse by becoming a glissile dislocation. Such a local catastrophic event can trigger similar effect in the other groups of dislocation. Thus, the final result is massive and has a collective character. It is followed by spontaneous generation of dislocations by rapidly increasing number of dislocation sources. It leads to a rapid local deformation. It is worth pointing out, that the avalanche-like barrier crossing by dislocations is manifested by acoustic effects of dry sounds emitted by the specimen. Based on the acoustic emission method (AE), tracking of slip band propagation during DPF is possible. Such a method is successfully used in the PLC and the Lüders slip bands propagation effects (Cáceres and Rodriguez, 1987; Chmelík et al., 2007). From the materials point of view, the most significant fact is that each massive failure of barriers during the tensile test is reflected by drop of stress and local increase of temperature (Fig. 32b). The increase of temperature is related to the dissipation of plastic power, and vanishing specific heat when temperature tends to 0 K. Macroscopically, the response of specimen during the kinematically controlled uniaxial tensile test at cryogenic temperature is presented in Fig. 32b. It consists of the oscillations of stress as a function of strain, the so-called serrations. Each serration in the stress-strain relation has similar pattern: after initial elastic process (1) smooth plastic flow occurs (2), until the abrupt drop of stress (3) and possible relaxation (4) take place. It is worth pointing out, that the last stage (4) varies significantly depending on the material (see Fig. 32b).

The mechanical origin of DPF is proved by experiment presented in Section 4.3. It is worth indicating, that the mechanical background of DPF is coupled with the thermodynamic effects. Thus, due to the local catastrophic failure of lattice barriers, the temperature increases rapidly (Fig. 32). Therefore, the constitutive model of DPF presented in this Thesis takes into account the mechanical background of the phenomenon, and the thermodynamic processes related to the mechanisms of heat transport in the weakly excited lattice at very low temperatures.

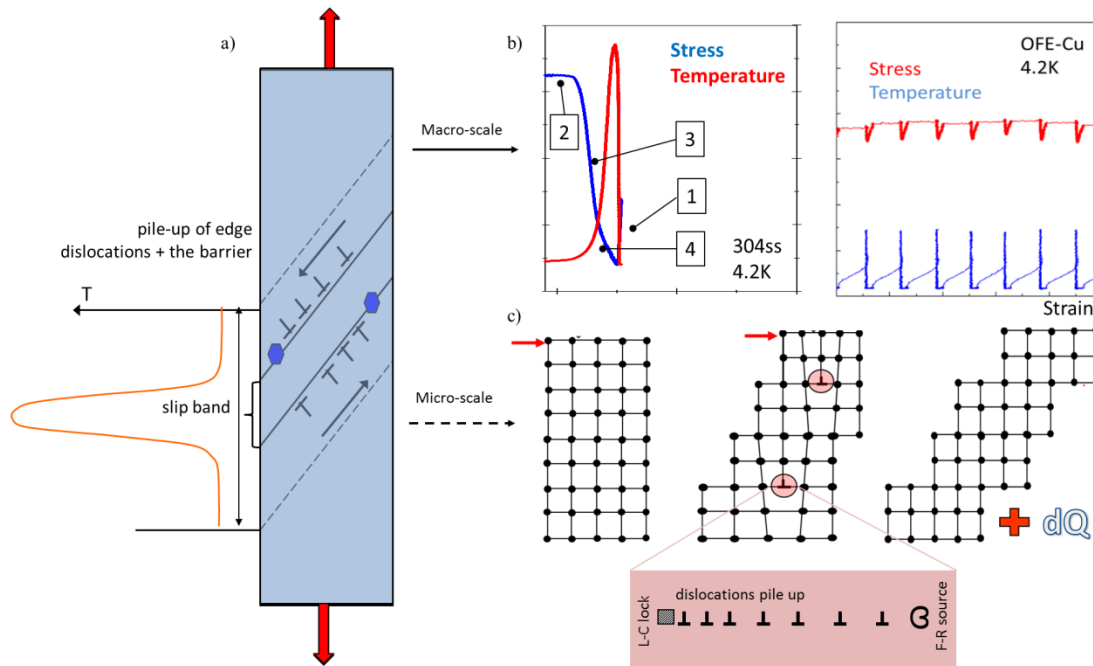


Fig. 32 a) The mechanism of discontinuous plastic flow (DPF); b) serration as the macroscopic response (stress-strain and temperature-strain) of the specimen during the kinematically controlled uniaxial tensile test at cryogenic temperature; c) the load drops observed in the stress-strain curves is attributed to catastrophic and massive failure of lattice barriers which generates localised heating observed during the tensile test

The model is defined by means of mesoscopic representative volume element (RVE). It is assumed, that the main material function that reflects the ability of lattice to enter the plastic flow instability is  $B$ , the density of dislocation pile-ups on the lattice barriers. This parameter is defined as follows:

$$B = \frac{dN}{dS} \quad (8)$$

where  $dN$  is a number of dislocation pile-ups at the lattice barriers, and  $dS$  denotes the RVE cross section. The RVE containing dislocations pile-ups at the lattice barriers is shown in Fig. 33.

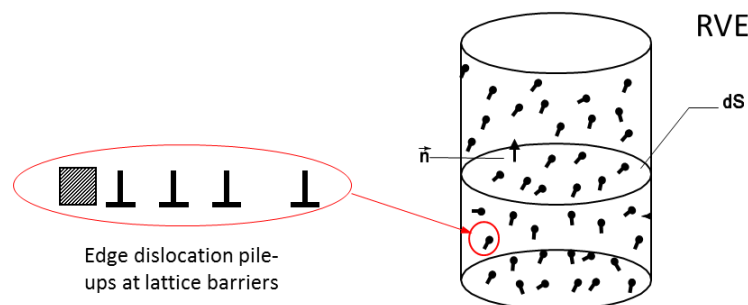


Fig. 33 RVE containing dislocation groups localised at the internal lattice barriers

For the DPF model it is assumed that the production of lattice barriers (e.g. the Lomer-Cottrell locks) is proportional to the accumulated plastic strain (Odqvist parameter). It means, that for a monotonic or cyclic loading the number of created barriers (locks) becomes a function of history of the process, represented by the increment of the accumulated plastic strain:

$$dp = \sqrt{\frac{2}{3} d\underline{\underline{\varepsilon}}^p : d\underline{\underline{\varepsilon}}^p} \quad \text{or} \quad dp = \sqrt{\frac{2}{3} \dot{\underline{\underline{\varepsilon}}}^p : \dot{\underline{\underline{\varepsilon}}}^p} dt \quad (9)$$

Thus, during plastic deformation, the lattice barriers are intensively generated. Therefore, the following kinetic law of evolution of density of dislocation pile-ups at the lattice barriers has been postulated (Skoczeń, 2008):

$$\dot{B} = F_{LC}^+(\rho, T, \underline{\underline{\sigma}}) \dot{p} H(p - p_{LC}) \quad (10)$$

where  $F_{LC}^+$  is function of lattice barriers density and depends on: dislocations density  $\rho$ , temperature  $T$  and stress  $\sigma$ . The threshold value  $p_{LC}$  indicates such a level of the accumulated plastic strain, above which the internal lattice barriers massively develop. Moreover,  $H$  denotes the Heaviside function defined as:

$$\begin{cases} H(x) = 0 & \text{for } x < 0 \\ H(x) = 1 & \text{for } x \geq 0 \end{cases} \quad (11)$$

When the process is isothermal, and small variation of the flow stress occurs, the increment of  $B$  is strictly related to the increment of the accumulated plastic strain:

$$dB = F_{LC}^+ dp \quad p \geq p_{LC} \quad (12)$$

### 5.1.2. RVE based constitutive description of DPF

Macroscopically, the DPF is reflected by stress oscillation during a kinematically controlled tensile test. It has been explained by the microscopic mechanism of rapid formation of dislocation pile-ups at strong obstacles such as the Lomer–Cottrell locks. The local shear stress at the head of dislocation pile-up, proportional to the number of dislocations in the pile-up, may reach the level of cohesive strength and the barrier may collapse. Such a local catastrophic event can trigger similar effect in the other groups of dislocation. Thus, the final result is massive, and has a collective character. Failure of the internal lattice barriers leads to massive motion of released dislocations, as well as to spontaneous generation of dislocations by new sources, accompanied by stepwise increase in the strain rate. Therefore, it is obvious that during the

process of slip, the relationship between the plastic shear strain and the dislocations density exists. However, one should first of all define the dislocations density  $\rho$ . It can be defined as the accumulated length  $dl$  of  $n$  dislocations per unit volume  $dV$ :

$$\rho = \frac{dl}{dV} \quad (13)$$

The dislocations density for the annealed metals remains in the range of  $10^{10} - 10^{12} m^{-2}$ , whereas for the cold rolled metals it stays between  $10^{14} - 10^{15} m^{-2}$ . Now, consider the RVE containing the edge dislocations. The motion of such a dislocation along the slip plane in the lattice leads to the so-called shear strain  $\gamma$ . The simplest mechanism of plastic deformation is reflected by a displacement of the upper part of lattice with respect to the lower part by the Burgers vector  $b$ . The shear strain is:

$$\gamma = \frac{b}{h} \quad (14)$$

where  $h$  means the height of the lattice. Now, consider the case when the dislocation has been partially moved through the slip plane (Fig. 34).

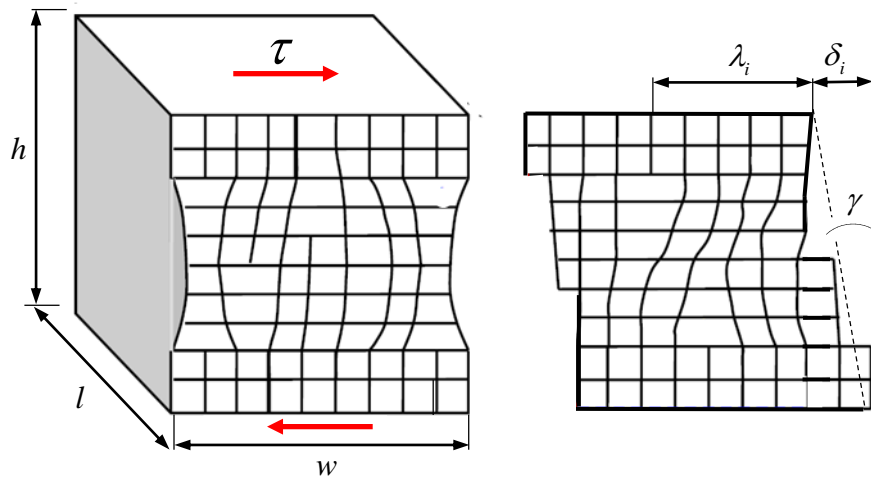


Fig. 34 Shear strain as a result of dislocation motion along the slip plane

The Burgers vector  $b$  is very small when compared to RVE dimensions. Thus, the displacement  $\delta_i$  of the dislocation at the position  $\lambda_i \in (0, w)$  can be expressed by:

$$\delta_i = \frac{\lambda_i}{w} b \quad (15)$$

where  $w$  denotes width of the lattice.

Motion of dislocations has often collective nature. Massive diffusion of dislocations along a given direction can form a slip band. If  $N$  dislocations move, the total displacement  $\Delta$  is defined as:

$$\Delta = \frac{b}{w} \sum_1^N \lambda_i \quad (16)$$

Moreover, the macroscopic plastic shear strain  $\gamma$  is expressed by:

$$\gamma = \frac{\Delta}{h} = \frac{b}{hw} \sum_1^N \lambda_i \quad (17)$$

The average distance that dislocations have reached  $\bar{\lambda}$ , can be defined as:

$$\bar{\lambda} = \frac{\sum_1^N \lambda_i}{N} \Rightarrow \sum_1^N \lambda_i = \bar{\lambda} N \quad (18)$$

Then, Eq. (17) can be expressed as follows:

$$\gamma = \frac{\Delta}{h} = \frac{b}{hw} \bar{\lambda} N \quad (19)$$

For the RVE, the following relation holds:

$$\rho = \frac{Nl}{whl} \Rightarrow N = \rho wh \quad (20)$$

where  $l$  denotes transverse diameter of the lattice. Substituting (20) to (19) one obtains:

$$\gamma = \rho b \bar{\lambda} \quad (21)$$

It should be noted, that in Eq. (21)  $\rho$  represents density of the mobile dislocations. Dislocations that do not move (sessile dislocations), would not contribute to the plastic flow. Based on Eq. (21) the shear strain rate can be expressed by:

$$\dot{\gamma} = \rho b \bar{v} \quad (22)$$

here  $\bar{v}$  is the average dislocations velocity.

In order to describe the evolution of the dislocations density during plastic deformation, the following relation between the shear strain and the dislocations density can be assumed:

$$\frac{d\rho}{d\gamma} = f(\rho, \dot{\gamma}, T) \quad (23)$$

According to the Mecking–Kocks theory (1981), this evolution is a result of competition between the rate of production of dislocations, and the rate of annihilation of dislocations:

$$\frac{d\rho}{d\gamma} = \left. \frac{d\rho}{d\gamma} \right|_+ + \left. \frac{d\rho}{d\gamma} \right|_- \quad (24)$$

Eq. (24) expresses the fact, that the evolution of dislocations density depends on the hardening of the material and on the dynamic recovery. The strain hardening due to the accumulation of dislocations depends on the mean distance  $\bar{\lambda}_i$ , that dislocation can glide before meeting an obstacle. The mean free path in the fcc materials deformed at cryogenic temperatures can be expressed in the following way:

$$\frac{1}{\bar{\lambda}_i} = \frac{1}{d} + k_1\sqrt{\rho} + k_2\sqrt{B} \quad (25)$$

where  $d$  is the average grain size,  $B$  is the surface density of lattice barriers (internal), and  $k_1, k_2$  are the constants. Relation (25), presented primarily by Bouquerel et al. (2006), has been extended to the form that includes lattice barriers density  $B$  as a representation of additional obstacles for dislocations motion (Skoczeń, 2008). Thus, the rate of production of dislocations takes the following form:

$$\left. \frac{d\rho}{d\gamma} \right|_+ = \frac{1}{bd} + \frac{k_1}{b}\sqrt{\rho} + \frac{k_2}{b}\sqrt{B} \quad (26)$$

It is worth pointing out, that during plastic deformation the dislocations can leave the glide planes within which they are stored at the obstacles. It is due to the so-called annihilation process, and is given by the following relation:

$$\left. \frac{d\rho}{d\gamma} \right|_- = -k_a\rho \quad (27)$$

where  $k_a$  represents the dislocation annihilation constant. Thus, two opposing effects determine variation of the dislocations density  $\rho$ , namely the storage and the recovery. Combining Eqs. (24)-(26), one obtains:

$$\frac{d\rho}{d\gamma} = \frac{1}{bd} + \frac{k_1}{b}\sqrt{\rho} + \frac{k_2}{b}\sqrt{B} - k_a\rho \quad (28)$$

In the fcc metals and alloys, the slip occurs in the specific directions associated with the crystallographic planes. The stress projection factors are used to calculate the stresses in these planes. The most common stress projection factor for the polycrystals is the Taylor factor  $M$ . Each grain in the polycrystalline materials is surrounded by other grains, so its change of shape is

compatible with its neighbours. In order to satisfy this compatibility, there exist slips along the easy and hard systems within a grain. Taylor (1938) assumed that each grain of a polycrystal undergoes the same shape change as the whole polycrystal. Also, Taylor proposed that a minimum of five active slip systems are required to accommodate an arbitrary deformation. The five (or more) active systems are those, that provide the greatest amount of work during deformation. In the course of a uniaxial tensile test, the incremental work per unit volume due to the external stress reads:

$$dw = \sigma_x d\varepsilon_x = \tau d\gamma \Rightarrow \frac{\sigma_x}{\tau} = \frac{d\gamma}{d\varepsilon_x} = M \quad (29)$$

Therefore, the relations between the overall stress (strain) and the local resolved shear stress (shear strain) in the polycrystals reads:

$$\sigma_x = M\tau \quad \text{and} \quad \varepsilon_x = \frac{d\gamma}{M} \quad (30)$$

In the fcc metals and alloys, the usual value of the Taylor factor is:  $M = 3.067$ . If the plastic strain dominates  $\varepsilon \simeq \varepsilon^p$ , Eq. (28) will have the following form (Skoczeń, 2008):

$$\frac{d\rho}{d\varepsilon^p} = M \left[ \frac{1}{bd} + \frac{k_1}{b} \sqrt{\rho} + \frac{k_2}{b} \sqrt{B} - k_a \rho \right] \quad (31)$$

As the main material function that reflects the ability of lattice to enter serrated yielding is the density of dislocation pile-ups on the lattice barriers  $B$ , the increment of this parameter can be expressed as:

$$dB = F_{LC}^+ d\varepsilon^p \quad \text{for} \quad \varepsilon \geq \varepsilon_{LC}^p \quad (32)$$

Now, consider the interaction of mobile dislocations with the other dislocations. If a mobile dislocation runs into an immobile one (e.g. forest dislocations), it is pinned by the immobile dislocation and the average resolved shear stress  $\tau$  is given by:

$$\tau = \alpha\mu b\sqrt{\rho} \quad (33)$$

In addition, the lattice resistance to the dislocations motion also acts, so that the intrinsic lattice strength (the Peierls stress)  $\tau_0$  also contributes to the flow stress. Therefore, the flow stress is expressed by:

$$\tau = \tau_0 + \alpha\mu b\sqrt{\rho} \quad (34)$$

where  $\mu$  is the shear modulus, and  $\alpha$  is the coefficient of dislocations interaction.

It is worth pointing out, that in addition to the applied shear stress, each dislocation in the pile-up has an impact on the leading dislocation in the pile-up. This leads to high concentration of stress at the leading dislocation in the pile-up at the lattice obstacle. Dislocations piled up against the barriers, produce the back stresses acting to oppose the motion of additional dislocations along the slip plane. The dislocations in the pile-up are tightly packed, and more widely spaced towards the source (e.g. Frank-Reed source). Eshelby et al. (1951) calculated the spatial distribution of dislocations in the pile-up. The number of edge dislocations that can occupy a distance  $L$  along the slip plane between the source and the obstacle (Hull and Bacon, 2011b) reads:

$$n = \frac{\pi(1-\nu)L\tau}{\mu b} \quad (35)$$

The stress at the head of dislocation pile-up can be expressed as:

$$\tau_e = n\tau \quad (36)$$

Substituting (36) to (35), and assuming that the distance between the source and the lattice barrier  $L$  is interpreted as the mean free path of dislocation  $\bar{\lambda}$ , one obtains the stress at the head of dislocation pile-up (Hull and Bacon, 2011b):

$$\tau_e = \frac{\pi(1-\nu)\bar{\lambda}\tau^2}{\mu b} \quad (37)$$

where  $\bar{\lambda}$  is defined through Eq. (25).

When the local shear stress at the head of dislocation pile-up  $\tau_e$ , reaches the level of the cohesive strength, the barrier collapses. Such a local catastrophic event can trigger similar effects in the other groups of dislocations. Thus, the final result is massive and collective. In order to describe such a process, let assume that the interaction between  $B$  and  $\tau_e$  triggers the serration (Fig. 35). Thus, the following criterion of avalanche-like failure of internal lattice barriers is applied (Skoczeń, 2008; Skoczeń et al., 2010):

$$\begin{cases} B = B_{cr} & \text{for } \tau \leq \tau_{min} \\ \tau_e = \tau_{cr} & \text{for } B \leq B_{min} \\ \frac{B - B_{min}}{B_{cr} - B_{min}} = \frac{\tau_e - \tau_{cr}}{\tau_{min} - \tau_{cr}} & \text{for } \tau > \tau_{min} \wedge B > B_{min} \end{cases} \quad (38)$$

The limits  $B_{min}, \tau_{min}$  were introduced, since for sufficiently large value of one of them, the other is insignificant for the phenomenon to occur and the following formulas were assumed:

$$\tau_{\min} = \alpha_{\tau} \tau_{cr}, \quad B_{\min} = \alpha_B B_{cr} \quad (39)$$

where  $\alpha_{\tau}, \alpha_B$  determine relevant fractions of the critical values. The graphical representation of serration criterion is presented in Fig. 35 (Skoczeń et al., 2010).

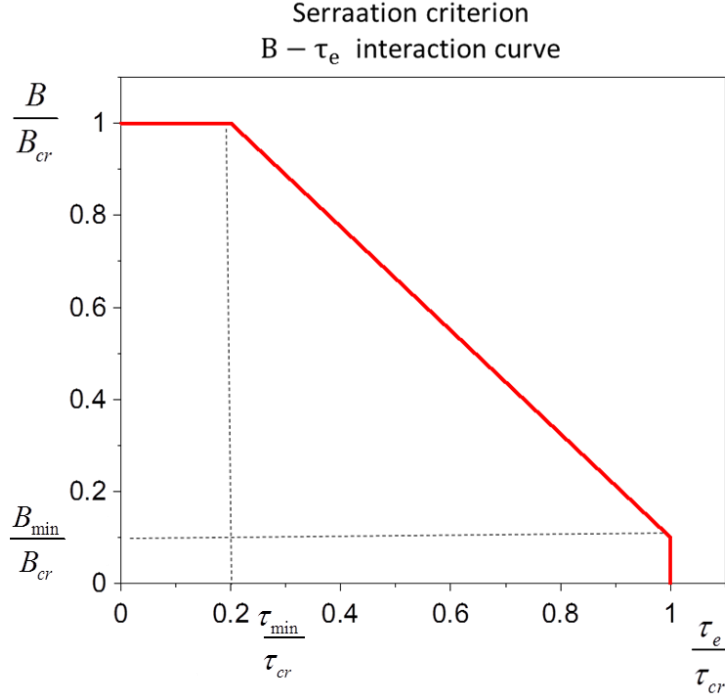


Fig. 35 Interaction curve  $(B, \tau_e)$  for single serration: normalised density of lattice barriers  $B$  against normalised shear stress at the head of dislocation pile-up  $\tau_e$

Thus, as soon as a combination of the density of lattice barriers  $B$  (containing dislocation pile-ups) with the average shear stress at the head of dislocation pile-up  $\tau_e$  reaches the interaction curve, the avalanche-like process is triggered.

In the uniaxial tensile test, the process of massive failure of lattice barriers results in the abrupt drop of stress  $\Delta\sigma$ , and instantaneous increase of the plastic strain  $\Delta\varepsilon_s^p$ , which is interpreted as the amount of slip during the catastrophic failure of lattice barriers (Fig. 36). In the initial model of DPF, drop of stress was based on the phenomenological approach, represented by the function  $F_{LC}^-$  (Skoczeń et al., 2010; Skoczeń et al., 2014). In the present model, the evolution of dislocations density is counted differently (Tabin et al., 2016). Thus, the drop of stress is obtained by means of Eqs (33) and (34), in the following form:

$$\Delta\sigma = M \mu \alpha b (\sqrt{\rho} - \sqrt{\rho_0}) \quad (40)$$

where  $\rho_0$  stands for the density of dislocations after serration. Such a definition makes the approach more physical, and allows for the evolution of the lower envelope of the stress-strain curve. Recall (Skoczeń, 2008), that during the kinematically controlled uniaxial tensile test, the abrupt drop of stress takes place at a constant value of total strain (see Fig. 32 and Fig. 36). The drop of stress results in the relevant strain redistribution, namely, in the decrement of the elastic part identical with the increment of the plastic part, hence:

$$\Delta \varepsilon_s = \frac{M \mu \alpha b (\sqrt{\rho} - \sqrt{\rho_0})}{E} \quad (41)$$

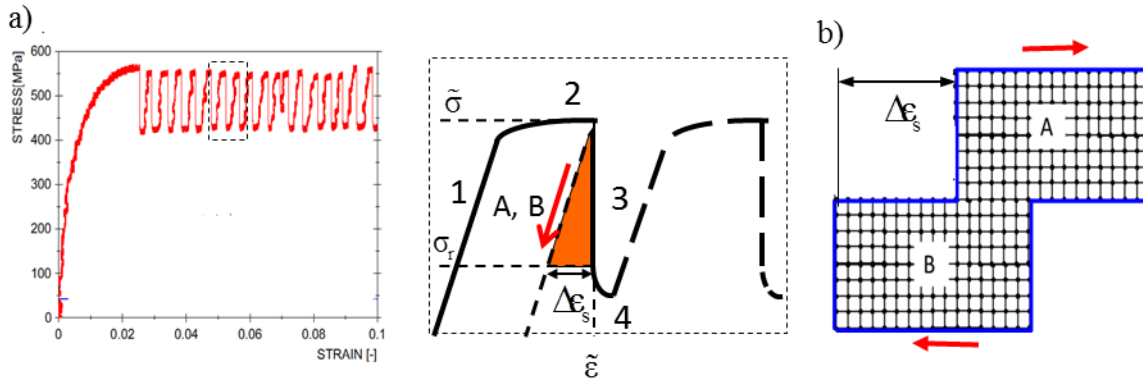


Fig. 36 The mechanism of plastic slip  $\Delta \varepsilon_s$  during DPF: a) the abrupt drop of the stress takes place at constant value of total strain  $\tilde{\varepsilon}$ ; b) illustration of plastic slip  $\Delta \varepsilon_s$

The massive failure of barriers is followed by fast motion of glissile dislocations in the lattice. The heat released in the course of this process depends on the plastic work, and the internal friction in the lattice (Skoczeń, 2008):

$$dQ = \eta_T (dW^p + dW^f) \quad (42)$$

where  $\eta_T$  denotes the Taylor-Quinney coefficient. In order to perform estimation of possible temperature fluctuations, the specific heat has to be expressed as a function of temperature:

$$dT = \frac{dQ}{mC_v(T)} \quad (43)$$

It turns out, that the temperature fluctuations may even reach some 40-50 K for 316LN stainless steel, or 5-8 K for the copper alloys (Fig. 32). Drop of stress in the course of serration is followed by the stress relaxation, down to a basic level determined by the equilibrium conditions. Mathematical description of this transitory behaviour is based on the phenomenological relation,

reflecting the so-called negative strain-rate sensitivity (Zaiser and Hähner, 1997). This stage of the serration is temperature driven (stage 4 in Fig. 32). The temperature rise has the form of Dirac function, and results from the energy dissipation during each serration, as well as from the thermodynamic instability. The stress relaxation is governed by the following set of equations (Zaiser and Hähner, 1997; Skoczeń, 2008):

$$\begin{cases} \sigma = \sigma_r + \Delta\sigma_T \\ (\Delta\sigma_T)_{,t} = [(\sigma_\infty - \sigma_r) - \Delta\sigma_T] / t_\Phi \end{cases} \quad (44)$$

where  $\sigma_r, \sigma_\infty$  are the stress levels: directly after the catastrophic slip and the asymptotic level (stress level after the transients have died out), respectively. Here,  $t_\Phi$  denotes the characteristic time of the relaxation process. The temperature evolves towards a new steady state value, inducing an additional stress increment  $\Delta\sigma_T$ .

## 5.2. Constitutive model of $\gamma$ - $\alpha'$ phase transformation

### 5.2.1. Plastic strain induced phase transformation

Austenitic stainless steels (grades 304, 304L, 316L, 316LN, 321, etc.) are often applied in cryogenic temperatures, even at the temperatures near 0 K. In such extreme conditions, the important features of these materials are their excellent physical and mechanical properties, including ductility and durability. During the plastic deformation at cryogenic temperatures, the austenitic stainless steel undergoes essentially three different dissipative phenomena including: discontinuous plastic flow (DPF), strain induced phase transformation from the parent phase  $\gamma$  to the  $\alpha'$  phase, and evolution of micro-damage (Fig. 38a) (Skoczeń, 2004; Egner et al., 2015). It is worth pointing out, that the DPF, as well as the phase transformation, are reflected in the stress-strain curve (Fig. 37). As already stated, the DPF is represented by the stress oscillations, whereas the strain induced phase transformation brings in significant hardening effect. This chapter is focused on the constitutive description of the strain-induced martensitic phase transformation in the austenitic stainless steels at cryogenic temperatures. Fig. 37 presents the results of kinematically controlled uniaxial tensile test of austenitic stainless steels (304 and 316L) at room temperature (RT), and at liquid helium temperature (4.2 K). The hardening effect due to the phase transformation is observable during the tensile test. Moreover, the intensity of the phenomenon is significantly different as a function of temperature (Fig. 37a) as well as chemical

composition (cf. Fig. 37b, c). In view of the foregoing, it is evident that the phase transformation significantly influences the macroscopic behaviour of the specimen during plastic deformation. Therefore, it is worth focusing on the microstructure evolution during plastic deformation.

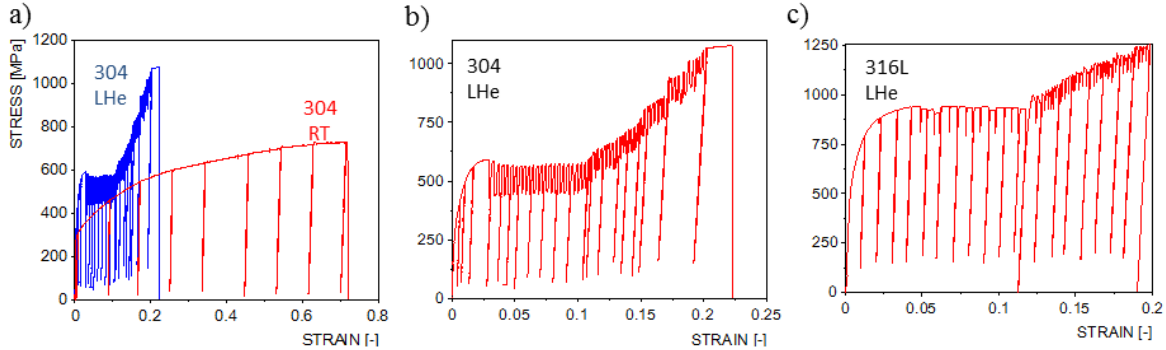


Fig. 37 The stress–strain curves of 304 and 316L stainless steels: a) effect of temperature (LHe - 4.2 K, and RT - 295 K) and chemical composition; b); c) serrated yielding of two metastable steels (304, 316L)

The face centered cubic ( $\gamma$ ) microstructure of austenitic stainless steel is often thermodynamically metastable. Thus, the stress and the inelastic strain may induce diffusionless martensitic phase transformation, by the force of which the  $\gamma$  austenite is transformed to the  $\alpha'$  martensite. Two different martensitic phases are distinguished in the stainless steels, namely,  $\varepsilon$ -hexagonal close packed (hcp) martensite, and  $\alpha'$  body centered cubic (bcc) martensite. Since the  $\alpha'$  and the  $\varepsilon$  martensite variants are much more rigid than the  $\gamma$  austenite, their presence affects the plastic flow and the process of hardening (Fig. 37). It is worth pointing out, that  $\varepsilon$  is not thermodynamically stable like  $\gamma$  or  $\alpha'$ , so it is assumed that  $\varepsilon$  is a transition phase (Venables, 1964).

The thermodynamic aspect of the strain-induced phase transformation is illustrated schematically in Fig. 38. Kinetics of the martensitic transformation is related to the temperature and the chemical free energy (Wayman and Bhadeshia, 1996). The spontaneous diffusionless martensitic transformation takes place when the difference between the Gibbs free energy (chemical free energy) of the austenite and the martensite exceeds a critical value  $\Delta G_{M_s}^{\gamma \rightarrow \alpha'}$ . This critical increment is defined for the  $M_s$  temperature. It is worth pointing out, that the phase transformation may occur at higher temperature than  $M_s$ , if sufficient mechanical driving force  $U'$  is available (Fig. 38b).

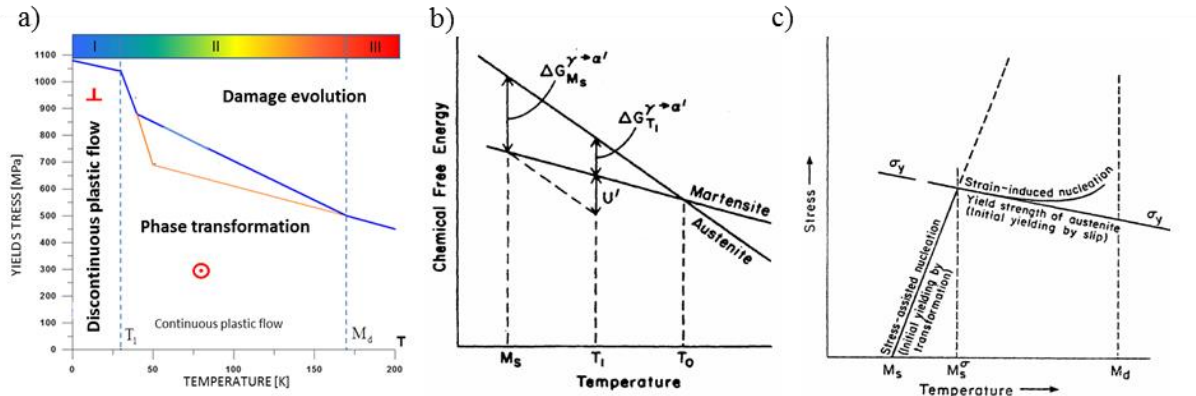


Fig. 38 a) Yield stress against temperature for 316LN; b) illustration of chemical free energy of austenite and martensite as a function of temperature (Wayman and Bhadeshia, 1996); c) critical stress to initiate martensitic transformation (Olson and Cohen, 1972)

The mechanical driving force  $U'$  results from the applied stress, that supports the chemical driving force  $\Delta G_{M_s}^{\gamma \rightarrow \alpha'}$  (Patel and Cohen, 1953). The chemical driving force of martensitic transformation decreases linearly with increasing temperature. Therefore, the applied stress related to mechanical driving force should increase linearly. The relationships between the applied stress, the temperature and the phase transformation were investigated by Bolling and Richman (1970). They defined the temperature  $M_s^\sigma$ , below which plastic strain can occur by means of the martensitic transformation. Above this temperature, yielding is initiated by a slip process in the austenitic phase. Thus, in order to distinguish between the phase transformation below and above temperature  $M_s^\sigma$ , Olson and Cohen (1972) introduced the concept of the stress assisted and the strain induced phase transformation (Fig. 38c).

Based on Fig. 38c one can conclude that for the temperatures below  $M_s$ , the chemical driving force is sufficiently large for pre-existing nucleation sites or embryos in the austenite. Thus, the extra stress is not necessary. On the other hand, for the temperature range between  $M_s$  and  $M_s^\sigma$ , the applied stress is required to trigger nucleation of the martensite embryos. Thus, it is the so-called stress assisted transformation range. The value of the required stress increases with temperature, because of decrease of the chemical driving force (Fig. 38b). At temperature  $M_s^\sigma$ , the strain induced nucleation is activated. For higher temperatures, further reduction in chemical driving force occurs. Therefore, it requires an extra stress to rise above the yield stress  $\sigma_y$ . Temperature  $M_d$  defines the upper limit for the strain induced transformation. Murr et al. (1982)

indicated that for the austenitic stainless steel (grade 304, 18.12% Cr; 8.60% Ni; 0.06% C; 1.19% Mn; 0.20% Co), the temperature  $M_d$  for  $\alpha'$  martensite remains above 323 K, and temperature  $M_s$  is below 77 K. Based on the experimental results for 304 and 316L, it can be concluded that temperature  $M_s$  remains below 4.2 K. The hardening effect observed in Fig. 37 has clearly strain induced background. Thus, in view of the foregoing, one concludes that the chemical composition, the temperature, the strain rate, and the strain state have significant impact on the strain induced martensitic transformation.

It is well established, that the intersections of the shear bands can be very effective strain induced nucleation sites of the martensitic embryos (Venables; Mangonon and Thomas; Olson and Cohen, 1972, 1975; Brooks et al., 1979b; Galindo-Nava and Rivera-Díaz-del-Castillo, 2017). In the case of austenitic stainless steels with high contents of chromium and nickel, low value of the stacking fault energy (SFE) of austenite promotes nucleation of  $\alpha'$  martensite at the intersection of shear bands (Diani and Parks, 1998). The shear bands can be in the form of  $\varepsilon$  martensite (hcp), mechanical twins or stacking fault bundles. The  $\varepsilon$  martensite in the shear band can be considered as an intermediate phase in the formation of  $\alpha'$  martensite. On the other hand, (Narutani et al., 1982) concluded that the  $\gamma - \alpha'$  martensite transformation takes place without an intermediate  $\varepsilon$  phase. Precise mechanisms by which the intersections can produce  $\alpha'$  martensite embryo have been described by Lecroisey and Pineau (1971), Staudhammer et al. (1982), Iwamoto et al. (1998), Cherkaoui et al. (2000). Yet, the phase transformation affected discontinuous plastic flow (DPF) has not been investigated.

### **5.2.1.1 Phase transformation affected DPF**

Based on the experimental results, one concludes that the martensitic phase transformation significantly influences the macroscopic slip band propagation during DPF (cf. Section 4.3). It is worth recalling the research papers by Suzuki et al. (1977), and by Brooks et al. (1979a, b). The Authors have suggested that the  $\alpha'$  martensite nucleation is associated with the piling-up of the Shockley partial dislocations (such partial dislocations generate the Lomer – Cottrell locks). Thus, as the dislocations are forced closer to each other in the pile-up, the atomic structure starts to resemble bcc stacking. When the pile-up reaches a critical size, rapid growth of the  $\alpha'$  martensite embryo occurs with the aid of the chemical driving force. It appears that the growth of the martensitic phase occurs through the continuous nucleation and coalescence of the

$\alpha'$  martensitic embryos during the plastic deformation (Murr et al., 1982). For 304ss, the minimum size of martensitic embryo was found to be 50-70 Å ( $1 \text{ \AA} = 10^{-10} \text{ m}$ ). In order to measure the  $\alpha'$  martensite embryo during the plastic deformation, the transmission electron microscope (TEM) was used (Staudhammer et al., 1983; Talonen, 2007). Distribution of the martensite embryos during the tensile test is presented in Fig. 39.

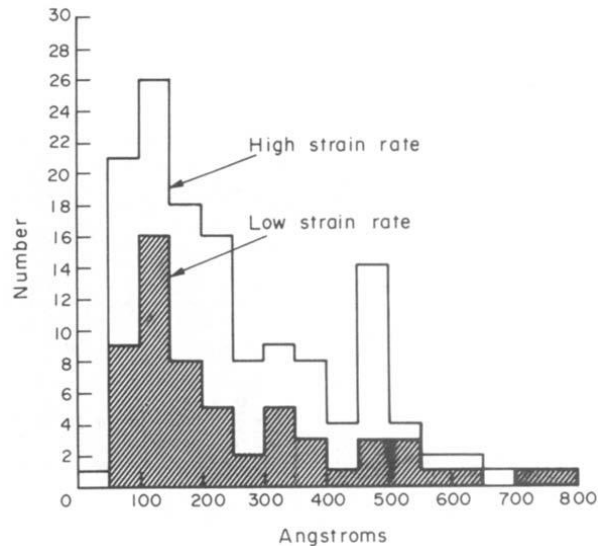


Fig. 39 Distribution of  $\alpha'$  martensite embryos during uniaxial tensile deformation at high and low strain at room temperature (Staudhammer et al., 1983)

In the light of the foregoing, it can be concluded that the discontinuous plastic flow (DPF) is strongly coupled with the strain induced phase transformation.

### 5.2.1.2 Kinetics of the strain induced martensitic transformation

Many authors have experimentally investigated this phenomenon, among them: Olson and Cohen (1975), Murr (1982), Staudhamer (1983), Shrinivas (1995), Iwamoto (1998), Ferreira (2004), Garion and Skoczeń (2002), etc. Based on the investigations presented in their papers, as well as own experiments, one concludes that the chemical composition (Fig. 37b,c), the temperature (Fig. 37a), the plastic strain, the stress state and the strain rate may have significant influence on  $\alpha'$  martensitic transformation.

Regarding the stress state, Murr et al. (1982) found that higher number of shear band intersections and martensitic phase was generated in biaxial tension, due to the higher number of active slip systems than during uniaxial tensile test. Shrinivas et al. (1995) reported that during cold rolling of 316 stainless steel, more  $\alpha'$  martensite was generated than during uniaxial tensile

test. It results from the multiple slip systems, which are activated during rolling (Talonen, 2007). Iwamoto et al. (1998) concluded, based on the experimental results of the uniaxial tension and compression tests for 304 stainless steel, that the volume fraction of martensite for compression is higher than that for tension in the initial stage of deformation, and this relation is reversed at higher strain.

The next factor affecting the strain induced  $\gamma - \alpha'$  phase transformation is the strain rate effect. The experimental results indicate that the transformation is reduced with increasing strain rate. The formation of  $\alpha'$  martensite is reduced due to the adiabatic heating generated during the higher velocity of deformation processes. Such a process decreases the chemical driving force of the transformation (Ferreira et al., 2004). A different point of view has been presented by Staudhamer (1983), who suggested that the high strain rate may promote more irregular structure of the shear bands. Thus, it can reduce the probability of formation of  $\alpha'$  martensite embryos. On the other hand, Hecker et al. (1982) and Murr et al. (1982), believe that high strain rate promotes shear band formation in the austenitic stainless steels. It leads to increase of the volume fraction of martensitic phase, but only at the early stages of tensile deformation. Thus, for higher strain rate, when the plastic deformation is advanced, the martensitic transformation is suppressed due to adiabatic heating (Ferreira et al., 2004).

It is well known that the  $\alpha'$  phase transformation is reduced when the test temperature increases (Olson and Cohen, 1975). Such a behaviour is attributed to the decrease in chemical driving force with increasing temperature, as indicated in Fig. 38b. It is confirmed by the experimental results (Fig. 37a), where the hardening effect is less pronounced for higher temperatures. The volume fraction of martensite as a function of plastic strain is presented in Fig. 40a for 304ss at different temperatures: from 77 K (temperature of liquid nitrogen) to 313 K. The rate of transformation is much higher at low temperatures. It can be concluded, that the presented experimental relations have sigmoidal shape, with the plastic strain thresholds and the saturation levels.

Olson and Cohen (1975) proposed a description of the strain induced martensitic nucleation. First of all, they have considered volume fraction of shear bands as a function of plastic strain. Thus, the number of shear bands can be calculated. Then, the number of shear band intersection in the RVE has been obtained. The increment of the number of  $\alpha'$  martensitic embryos produced per austenite unit volume can be related to the increase of the number of shear

band intersections. Based on such a consideration, the following relation for the volume fraction of martensite  $f^{\alpha'}$  versus plastic strain  $\varepsilon$  has been obtained:

$$f^{\alpha'} = 1 - \exp\left(-\beta\left[1 - \exp(-\alpha\varepsilon)\right]^n\right) \quad (45)$$

where

$$\beta = \frac{\bar{v}^{\alpha'} \pi d^2}{16(\bar{v}^{sb})^n} p \quad (46)$$

and  $\beta$  denotes the parameter proportional to the probability that an intersection will form an embryo,  $\alpha$  denotes a parameter which is temperature sensitive through its dependency on the stacking fault energy,  $p$  is the probability that a shear band intersection will generate a martensitic embryo,  $\bar{v}^{\alpha'}$  denotes average volume of martensite,  $\bar{v}^{sb}$  denotes average volume of shear bands,  $d$  denotes austenitic grain size, and  $n$  is a fixed exponent ( $n = 4.5$  for 304ss; (Olson and Cohen, 1975)).

A good correlation was obtained for Eq. (45) and data presented by Shin et al. (2001), for 304 austenitic stainless steel (Fig. 40a). In order to confirm the fact, that the  $\alpha'$  martensite embryos are produced in the shear band intersections during the plastic deformation, a transmission electron microscope was used (Fig. 41).

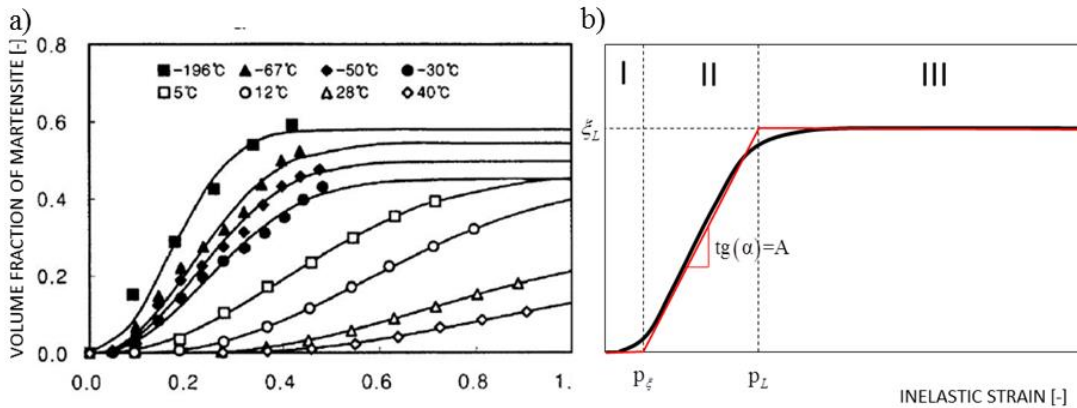


Fig. 40 a) Volume fraction of martensitic phase against inelastic strain for 304ss during uniaxial tensile tests (Shin et al., 2001); b) linearized kinetics of the phase transformation (Garion and Skoczeń, 2002)

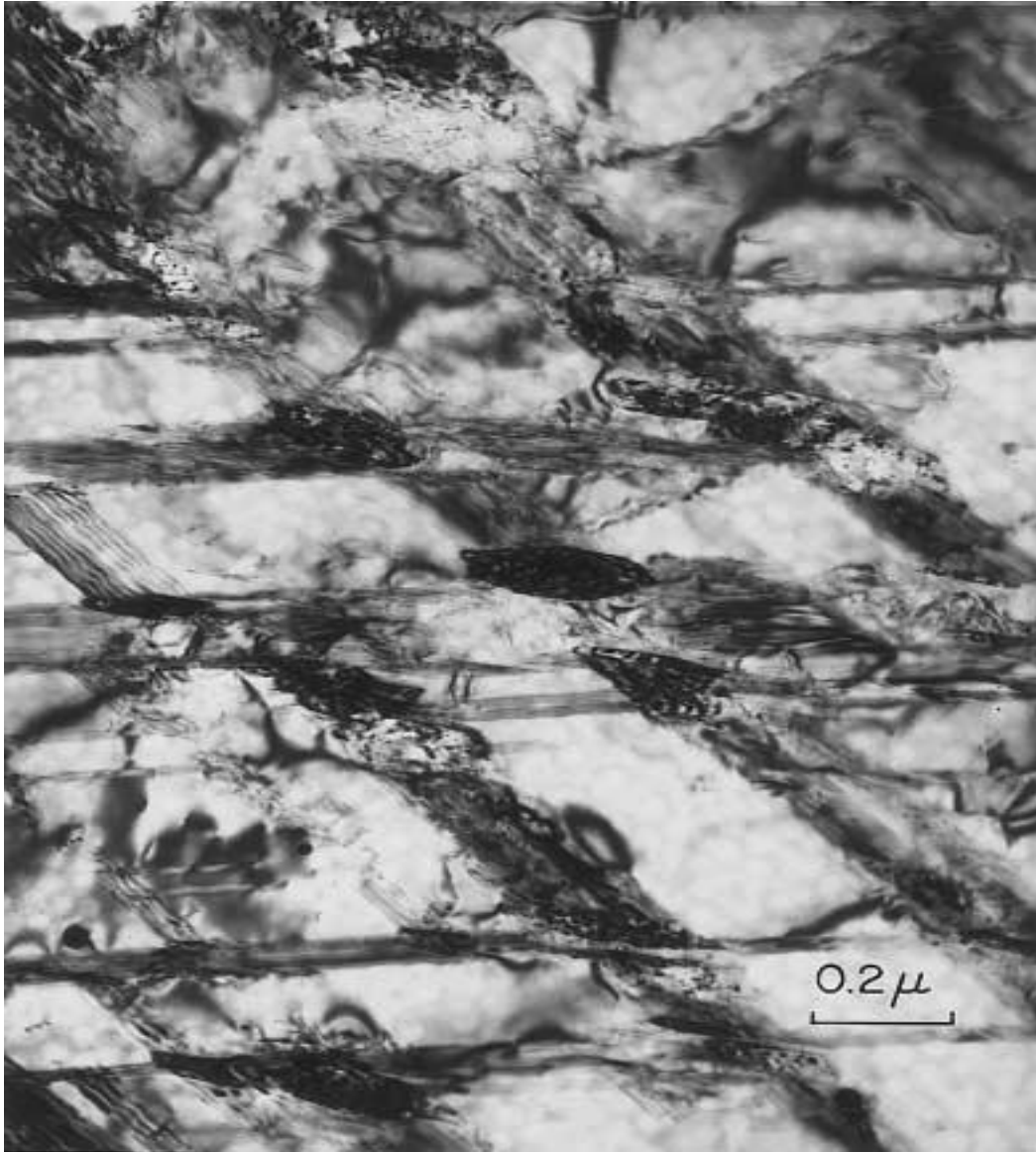


Fig. 41 Martensitic embryos (dark) formed at shear band intersections in the cold-worked 304 stainless steel foil deformed at 77 K (Olson and Cohen, 1975)

The Olson-Cohen model for the evolution of martensite volume fraction was extended by Stringfellow et al. (1992). The Authors concluded, that the martensitic nucleation is not only a function of the plastic strain and the temperature (Olson and Cohen, 1975), but also the stress state. Isotropic hypo-elastic formulation was used to describe the evolution of the stress state. The Authors applied self-consistent approach to describe the deviatoric plastic strain rate. They assumed, that the incompressible spherical inclusions are embedded in the infinitely extended, incompressible, isotropic matrix. Thus, the Eshelby solution was used as a basis for the localisation law.

Analysing the stress strain curve obtained for metastable austenitic stainless steels, Narutani et al. (1982) identified two factors controlling the flow stress, namely the static-hardening effect associated with two-phase mixture, and the dynamic-softening effect arising from the operation of the martensitic transformation as a deformation mechanism. Based on the quantitative determination of these two contributions to the plastic flow behaviour, the constitutive model was developed.

A different approach was proposed by Fisher et al. (1990, 1998). The constitutive model includes micro-plasticity coupled with  $\gamma - \alpha'$  phase transformation. The phase transformation consists in the irreversible deformation of transforming specimens, under the stress state with the equivalent stress significantly lower than the yield stress. Specific form of the chemical free energy (the Gibbs potential), and the plastic flow with the phase transformation have been used. During the displacive transformation ( $\gamma - \alpha'$  phase transformation), change of the volume and the shape of micro-regions were described by the microscopic eigen strain tensor (also called “free” transformation strain tensor (Fisher, 1989)). Based on this concept, the mesoscopic strain tensor can be obtained by integrating the microscopic eigen strain tensor over the RVE. Such an approach is used in the model presented in the present chapter (Eq. (66)).

Diani and Parks (1997) proposed a model that predicts the volume fraction of martensitic phase in a steel during thermo-mechanical loading. The Authors assumed that formation of the shear bands is an irreversible process, and the slip bands can be blocked by the  $\alpha'$  martensitic phase. Only two mechanisms of shear band formation are considered: twinning or formation of the  $\varepsilon$  variant of martensite. At the intersection of shear bands, the nucleation of martensitic phase takes place. A modified Taylor-based numerical calculation was used in order to obtain the intensity of the shear and, hence, the volume fraction of martensite. For the initial stage of phase transformation, the model is in good agreement with the experimental results presented by Shin et al. (2001).

The problem of the strain induced martensitic transformation at the shear band intersection was described by Levitas et al. (1998). The mesoscopic continuum thermomechanical approach was used by the Authors. The model is based on the multiplicative decomposition of the total deformation gradient into elastic, plastic and transformation parts. The generalized Prandtl-Reuss equation has been used for isotropic, elasto-plastic material, as well as the large strains. Location of the martensitic phase and its volume are determined based on the

transformation criterion and the extremum principle. The Authors believe that for the strain induced transformation, the transformation work is maximal in the shear-band intersections. Further growth beyond the intersection is suppressed due to the fact, that the transformation work decreases significantly and the transformation at the other shear-band intersections is favoured.

Han et al. (2004) have also assumed that the martensitic phase nucleates in the shear band intersections. The growth of nucleation site in the austenite due to the plastic deformation was formulated as the increase of the shear band intersection. The self-consistent approach was applied to describe the behaviour of each phase. The numerical model was validated based on the uniaxial tensile test and the shear test of 204M stainless steel.

A new constitutive model was proposed by Tomita and Iwamoto (2001). The model includes the influence of the strain rate, the temperature as well as the applied stress on the strain induced phase transformation. The model validation was carried out based on the monotonic and the cyclic tests including tension, compression and shearing of 304 stainless steel in a wide range of temperatures, from 77 K to 353 K.

An advanced model of plastic strain induced fcc-bcc phase transformation, including simplified kinetics for the extremely low temperatures, has been developed by Garion and Skoczeń (2002, 2003), Garion, Skoczeń and Sgobba (2006), and Skoczeń (2007). The multiscale model includes nonlinear mixed kinematic and isotropic hardening, resulting from interaction between the dislocations and the martensitic inclusions, as well as dynamically evolving tangent stiffness resulting from the evolution of proportion between the phases. The tangent stiffness operator is computed at each point of the equilibrium path by means of the Mori-Tanaka homogenisation. The model has been validated against experimental data and yields correct results for metastable materials operation at near 0 K temperatures. In particular, the model has been applied to predict distribution of both phases in the functionally graded structural members, obtained by means of the strain controlled phase transformation process.

Based on the experimental results, it can be concluded that the kinetics of martensitic transformation is represented by sigmoidal shape for a wide range of temperatures. The below presented model assumes that at extremely low temperatures the plastic strain induced phase transformation occurs in very fast way, and follows nearly linear transformation path in terms of the volume fraction of martensite as a function of plastic strains (Garion and Skoczeń, 2002).

Thus, the linearised kinetic law of phase transformation has been adopted (Fig. 40). It significantly reduces the number of parameters that have to be measured at low temperatures.

### 5.2.1.3 RVE based constitutive description of $\gamma$ - $\alpha'$ phase transformation

In order to model the strain induced phase transformation, a scalar parameter  $\xi$  is defined. This parameter is defined in the RVE (representative volume element) as the ratio between the volume of martensitic phase  $dV_\xi$  and the total volume of the RVE  $dV$  (Fig. 42). Hence:

$$\xi = \frac{dV_\xi}{dV}; \quad 0 \leq \xi \leq 1 \quad (47)$$

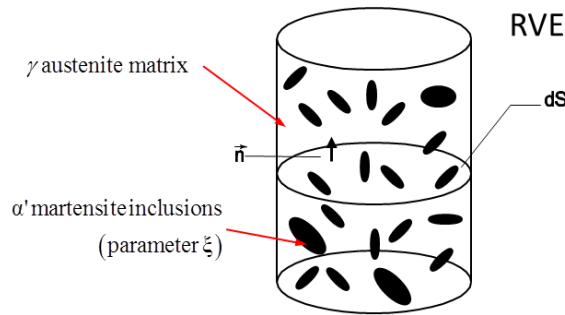


Fig. 42 Representative volume element (RVE) with martensite inclusions

The volume fraction of martensite depends on the plastic strain, the strain rate, the state of stress and the temperature (Olson and Cohen, 1975; Hecker et al., 1982; Shin et al., 2001; Garion and Skoczen, 2002; Garion and Skoczen, 2003; Talonen, 2007; Ortwein, 2015), thus  $\xi$  can be expressed as:

$$\xi = \xi(p, T, \underline{\dot{\epsilon}}^p, \underline{\sigma}) \quad (48)$$

The plastic strain induced  $\gamma$ - $\alpha'$  phase transformation in the austenitic stainless steels occurs in a wide range of temperatures below  $M_d$  (Fig. 38c). The process is controlled via the transformation kinetics, represented by the phase transformation curve (Fig. 40a), which presents the evolution of the martensite content as a function of the accumulated plastic strain. For the uniaxial tensile test at extremely low temperatures, under low strain rate and isothermal condition, the volume fraction of martensite curve has the sigmoidal form, presented in Fig. 40b. The phase transformation process can be subdivided into three stages: low rate transformation below the threshold  $p_\xi$  (stage I), fast transformation with high and nearly constant

transformation rate (stage II) and asymptotically vanishing transformation with the rate decreasing to 0 and the volume fraction of martensite reaching a maximum level  $\xi_L$  (stage III). Stage II can be linearised (Garion, Skoczeń, 2002, 2003). It helps to simplify the constitutive description of the transformation kinetics. In view of the foregoing, the evolution curve can be simplified (red curve, Fig. 40b). The simplified kinetics is described by the following parameters:  $A(T)$  denotes the phase transformation intensity parameter,  $\xi_L$  is the maximum volume fraction of martensite,  $p_\xi$  is the threshold value of the accumulated plastic strain, at which the phase transformation begins, and  $p_L$  denotes the value of the accumulated plastic strain, at which the martensitic saturation is observed. Thus, the following relation describes the volume fraction of martensite:

$$\xi = \begin{cases} 0 & 0 < p < p_\xi \\ A(T)(p - p_\xi) & p_\xi < p < p_L \\ \xi_L & p > p_L \end{cases} \quad (49)$$

For complex loading and general conditions, the evolution law for the volume fraction of martensite has been introduced for the linear stage II of the sigmoidal curve by Garion and Skoczeń (2002, 2003):

$$\dot{\xi} = A(T, \underline{\underline{\dot{\varepsilon}}^p}, \underline{\underline{\sigma}}) \dot{p} H[(p - p_\xi)(\xi_L - \xi)] \quad (50)$$

where  $H[...]$  represents the Heaviside function, and  $\dot{p}$  is the rate of the accumulated plastic strain, defined as:

$$\dot{p} = \sqrt{\frac{2}{3} \underline{\underline{\dot{\varepsilon}}^p} : \underline{\underline{\dot{\varepsilon}}^p}} \quad (51)$$

where  $\underline{\underline{\varepsilon}}^p$  denotes the plastic strain tensor.

### 5.2.2. The constitutive model

The RVE based constitutive model describes the behaviour of ductile materials in which  $\gamma-\alpha'$  phase transformation occurs at extremely low temperatures. The model is based on the following assumptions (Garion and Skoczen, 2002; Garion and Skoczen, 2003; Skoczeń, 2007; Sitko et al., 2010; Ortwein, 2015):

- The accumulated plastic strain is driving force of the martensitic phase transformation.
- The RVE consists of two-phase continuum, namely the austenitic matrix and the martensite platelets, represented by small type Eshelby ellipsoidal inclusions, randomly distributed and randomly oriented in the matrix.
- During loading, the elasto-plastic behaviour of the austenitic matrix is observed, whereas the inclusions show purely elastic response. The yield stress of the martensite fraction is much higher than the yield stress of the austenite.
- Rate independent plasticity is applied: it is assumed that the influence of the strain rate is small for the range of temperatures 4.2–77 K (Hecker et al., 1982), and the phase transformation intensity parameter  $A$  depends on the temperature and the stress state only.
- Small strains are assumed: the accumulated plastic strain  $p$  does not exceed 0.2.
- The two-phase material obeys the classical associated flow rule.

The constitutive model of  $\gamma-\alpha'$  phase transformation has been developed for two-phase isotropic and ductile material. The model consists of the following equations (cf. Garion and Skoczeń, 2002, 2003; Skoczeń, 2007):

- The kinetic law of the strain induced phase transformation:

$$\dot{\xi} = A(T, \underline{\underline{\sigma}}) \dot{p} H \left[ (p - p_{\xi})(\xi_L - \xi) \right] \quad (52)$$

where,  $A(T, \underline{\underline{\sigma}})$  denotes the intensity parameter, which depends on the temperature and the stress state,  $\dot{p}$  is the rate of the accumulated plastic strain, defined as  $\dot{p} = \sqrt{\frac{2}{3} \dot{\underline{\underline{\epsilon}}^p : \dot{\underline{\underline{\epsilon}}^p}}$ ,  $H[\dots]$  represents the Heaviside function,  $p_{\xi}$  denotes the accumulated plastic strain threshold, and  $\xi_L$  is the maximum volume fraction of martensite.

- The constitutive relation between the stress and the strain (Section 5.2.3):

$$\underline{\underline{\sigma}} = \underline{\underline{E}} : (\underline{\underline{\varepsilon}} - \underline{\underline{\varepsilon}}^p - \underline{\underline{\varepsilon}}^{th} - \underline{\underline{\varepsilon}}^{bs}) \quad (53)$$

where  $\underline{\underline{\varepsilon}}^{th}$  is the thermal strain, and  $\underline{\underline{\varepsilon}}^{bs}$  denotes the Bain strain tensor, defined as:

$$\underline{\underline{\varepsilon}}^{bs} = \frac{1}{3} \xi \Delta v \underline{\underline{I}}; \quad d\underline{\underline{\varepsilon}}^{th} = \alpha^h \underline{\underline{I}} dT \quad (54)$$

where,  $\Delta v$  denotes the relative volume change,  $\underline{\underline{I}}$  is the identity tensor. The thermal strain increment  $d\underline{\underline{\varepsilon}}^{th}$  is given as a function of  $\alpha^h$ , the homogenised dilatation coefficient of two-phase material.

- The definition of the yield surface (Section 5.2.4) reads:

$$f(\sqrt{J_2}, \underline{\underline{X}}, R) = \sqrt{\frac{3}{2} (\underline{\underline{s}} - \underline{\underline{X}}) : (\underline{\underline{s}} - \underline{\underline{X}})} - \sigma_0 - R \quad (55)$$

where,  $\underline{\underline{X}}$  is the so-called back stress tensor and represents the hardening variables (cf. Eq. (60)),  $R$  is the isotropic hardening variable,  $\sigma_0$  denotes the yield stress, and  $J_2$  denotes the 2<sup>nd</sup> invariant of the stress deviator, and has the form:

$$J_2 = \sqrt{\frac{3}{2} (\underline{\underline{s}} - \underline{\underline{X}}) : (\underline{\underline{s}} - \underline{\underline{X}})} \quad (56)$$

where  $\underline{\underline{s}}$  is the deviatoric stress tensor:

$$\underline{\underline{s}} = \underline{\underline{\sigma}} - \frac{1}{3} Tr(\underline{\underline{\sigma}}) \underline{\underline{I}} \quad (57)$$

where,  $Tr(\underline{\underline{\sigma}}) = \sigma_{11} + \sigma_{22} + \sigma_{33}$  denotes the trace of the stress tensor  $\underline{\underline{\sigma}}$ .

- The associated plastic flow is applied (Section 5.2.5):

$$\underline{\underline{\dot{\varepsilon}}}^p = \frac{\partial f}{\partial \underline{\underline{\sigma}}} \dot{\lambda} = \frac{3}{2} \frac{\underline{\underline{s}} - \underline{\underline{X}}}{\sqrt{\frac{3}{2} (\underline{\underline{s}} - \underline{\underline{X}}) : (\underline{\underline{s}} - \underline{\underline{X}})}} \dot{\lambda} \quad (58)$$

where  $\underline{\underline{\dot{\varepsilon}}}^p$  denotes the plastic strain rate tensor,  $\dot{\lambda}$  is the plastic strain multiplier, defined as (cf. Sitko et al., 2010):

$$\lambda = \frac{\frac{3}{2} \frac{\underline{s} - \underline{X}}{\sqrt{\frac{3}{2}(\underline{s} - \underline{X}) : (\underline{s} - \underline{X})}} : \underline{\underline{E}} : \left( \underline{\dot{\underline{\varepsilon}}} - \frac{1}{3} \underline{\dot{\underline{\varepsilon}}} \Delta v \underline{\underline{I}} \right)}{\frac{3}{2} \frac{\underline{s} - \underline{X}}{\sqrt{\frac{3}{2}(\underline{s} - \underline{X}) : (\underline{s} - \underline{X})}} : \underline{\underline{E}} : \frac{3}{2} \frac{\underline{s} - \underline{X}}{\sqrt{\frac{3}{2}(\underline{s} - \underline{X}) : (\underline{s} - \underline{X})}} + C_x(\underline{\xi}) + (1 - \beta) C_{a+m}} \quad (59)$$

where  $\underline{\underline{E}}$  denotes 4<sup>th</sup> order elastic stiffness tensor,  $C_{a+m}$  is the homogenised modulus (or the so-called surplus tangent stiffness modulus, expressed in Eqs (160)-(163)), and  $C_x(\underline{\xi})$  is the kinematic hardening modulus (Eq. ((170)). In order to establish a proportion between the kinematic and the isotropic hardening, the Bauschinger parameter  $\beta$  has been introduced (Skoczeń, 2007).

- The evolution of the kinematic hardening variable (Eq. (169)) reads:

$$\underline{\dot{\underline{X}}} = \frac{2}{3} C_x(\underline{\xi}) \underline{\dot{\underline{\varepsilon}}}^p = \frac{2}{3} (C_{a0} + C_{a0} h \underline{\xi} + \beta C_{a+m}) \underline{\dot{\underline{\varepsilon}}}^p \quad (60)$$

where  $C_{a0}$  is the hardening modulus of pure austenite, and  $h$  is the material dependent parameter, reflecting the interactions between the dislocations and the martensite inclusions.

- The evolution of the isotropic hardening variable (Eq. (166)) reads:

$$\dot{R} = C_R(\underline{\xi}) \dot{p} \quad (61)$$

where  $C_R(\underline{\xi}) = (1 - \beta) C_{a+m}$ , and  $\dot{p}$  is the rate of the accumulated plastic strain, defined as:

$$\dot{p} = \sqrt{\frac{2}{3} \underline{\dot{\underline{\varepsilon}}}^p : \underline{\dot{\underline{\varepsilon}}}^p} \quad (62)$$

where  $\underline{\dot{\underline{\varepsilon}}}^p$  is the rate of the plastic strain tensor.

### 5.2.3. The stress-strain relation

The general constitutive law contains the plastic, the thermal and the transformation strains:

$$\underline{\underline{\sigma}} = \underline{\underline{E}} : \left( \underline{\underline{\varepsilon}} - \underline{\underline{\varepsilon}}^p - \underline{\underline{\varepsilon}}^{th} - \underline{\underline{\varepsilon}}^{bs} \right) \quad (63)$$

where  $\underline{\underline{\varepsilon}}^p$  is the plastic strain tensor,  $\underline{\underline{\varepsilon}}^{th}$  denotes the thermal strain tensor,  $\underline{\underline{\varepsilon}}^{bs}$  denotes free deformation tensor, called the Bain strain, and  $\underline{\underline{E}}$  is the elastic stiffness tensor.

The mesoscopic Bain strain tensor is equal to:

$$\underline{\underline{\varepsilon}}^{bs} = \frac{1}{3} \xi \Delta v \underline{\underline{I}} \quad (64)$$

The Bain strain determines the strain associated with transformation from  $\gamma$  to  $\alpha'$  phase during the plastic deformation. Bain strain occurs because the volume of martensite is larger than the primary volume of the austenite (Fig. 43).

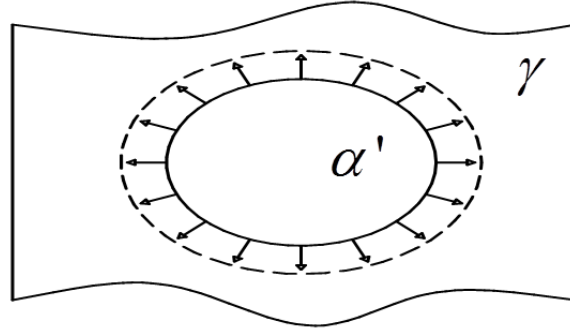


Fig. 43 During  $\gamma - \alpha'$  transformation, the volume of martensite ( $\alpha'$ ) is larger than the primary volume of austenite ( $\gamma$ )

This change of volume is defined as:

$$\Delta v = \frac{V_{\alpha'} - V_{\gamma}}{V_{\gamma}} \quad (65)$$

where  $V_{\alpha'}$  and  $V_{\gamma}$  denote, respectively, the volumes of martensite and austenite. This difference is of the order of 3-5 % of the primary volume. In order to obtain the mesoscopic strain tensor  $\underline{\underline{\varepsilon}}^{bs}$ , integration of the microscopic eigen-strain tensor (“free” transformation strain) over the RVE is required (Garion and Skoczeń, 2002, 2003).

$$\underline{\underline{\varepsilon}}^{bs} = \frac{1}{V} \int_{V_{\alpha'} = \mu} \underline{\underline{\varepsilon}}^{bs} dV \quad (66)$$

It is assumed that the RVE consists of two phases, thus Eq. (66) can be expressed as:

$$\underline{\underline{\varepsilon}}^{bs} = \frac{V_{\gamma}}{V} \frac{1}{V_{\gamma}} \int_{V_{\gamma} = \mu} \underline{\underline{\varepsilon}}^{bs} dV + \frac{V_{\alpha'}}{V} \frac{1}{V_{\alpha'}} \int_{V_{\alpha'} = \mu} \underline{\underline{\varepsilon}}^{bs} dV \quad (67)$$

As the microscopic eigen-strain  $\underline{\underline{\varepsilon}}_{\mu}^{bs}$  occurs only in the martensitic phase, one obtains the following form:

$$\underline{\underline{\varepsilon}}^{bs} = \frac{V_{\gamma}}{V} \frac{1}{V_{\gamma}} \int_{V_{\gamma} = \mu} 0 dV + \frac{V_{\alpha'}}{V} \frac{1}{V_{\alpha'}} \int_{V_{\alpha'} = \mu} \underline{\underline{\varepsilon}}^{bs} dV = \frac{V_{\alpha'}}{V} \frac{1}{V_{\alpha'}} \int_{V_{\alpha'} = \mu} \underline{\underline{\varepsilon}}^{bs} dV \quad (68)$$

Then, substituting the following relation to Eq. (68):

$$\frac{V_\alpha}{V} = \xi \quad (69)$$

and assuming that:

$$\frac{1}{V_\alpha} \int_{V_\alpha} \underline{\underline{\varepsilon}}_{\underline{\underline{\mu}}}^{bs} dV = \left\langle \underline{\underline{\varepsilon}}_{\underline{\underline{\mu}}}^{bs} \right\rangle \quad (70)$$

one obtains:

$$\underline{\underline{\varepsilon}}_{\underline{\underline{\mu}}}^{bs} = \xi \left\langle \underline{\underline{\varepsilon}}_{\underline{\underline{\mu}}}^{bs} \right\rangle \quad (71)$$

Wechsler et al. (1953) proved that during a displacive transformation, the Bain strain is equivalent to a combination of the shear strain plus an extension normal to the habit plane. Thus, the eigen-strain tensor has the following form:

$$\underline{\underline{\varepsilon}}_{\underline{\underline{\mu}}}^{bs} = \begin{pmatrix} 0 & 0 & \frac{\gamma_\mu}{2} \\ 0 & 0 & 0 \\ \frac{\gamma_\mu}{2} & 0 & \Delta v \end{pmatrix}_{(x,y,z)} \quad (72)$$

where  $x, y, z$  stand for the local coordinate system. It is assumed that the habit plane of the product phase is represented by  $(x, y)$ , whereas,  $z$  is the vector normal to the habit plane. The shear strain is denoted by  $\gamma_\mu$ , and the relative volume change  $\Delta v$  has been defined in Eq. (65). In view of the random orientation of grains, one deduces random orientation of the micro-regions in the RVE. Thus, by integrating the microscopic eigen-strain over the RVE one obtains the isotropic tensor:

$$\left\langle \underline{\underline{\varepsilon}}_{\underline{\underline{\mu}}}^{bs} \right\rangle = \frac{1}{3} \Delta v \underline{\underline{I}} \quad (73)$$

Substituting Eq. (73) to (71) one obtains Eq. (64). In Eq. (63), except for the Bain strain  $\underline{\underline{\varepsilon}}_{\underline{\underline{\mu}}}^{bs}$ , the thermal strain tensor appears. The increment of the thermal strain  $d\underline{\underline{\varepsilon}}^{th}$  is given as a function of dilatation  $\hat{\underline{\underline{\alpha}}}$  of two phase material (Garion, 2003):

$$d\underline{\underline{\varepsilon}}^{th} = \hat{\underline{\underline{\alpha}}}(T, \xi) dT \quad (74)$$

In the case of isotropy of the material, tensor  $\hat{\underline{\underline{\alpha}}}$  can be reduced to:

$$\hat{\underline{\underline{\alpha}}} = \alpha^h \underline{\underline{I}} \quad (75)$$

where,  $\alpha^h$  denotes the homogenised dilatation coefficient, and  $\underline{\underline{I}}$  is the identity tensor.

#### 5.2.4. The yield surface

The yield criterion defines the elastic limits of the material under complex stress state. The elastic limit during uniaxial tensile test is the yield stress  $\sigma_0$ , while in a simple shear test, it is the shear stress  $\tau_0$ . Generally, the yield condition can be expressed as:

$$f(\underline{\underline{\sigma}}, k_1, k_2, \dots) = 0 \quad (76)$$

where  $k_1, k_2$  are the material constants, which can be determined experimentally. For the isotropic materials, the values of three principal stresses  $(\sigma_I, \sigma_{II}, \sigma_{III})$  are sufficient to describe the state of stress uniquely. Thus, the yield criterion has the following general form:

$$f(\sigma_I, \sigma_{II}, \sigma_{III}, k_1, k_2, \dots) = 0 \quad (77)$$

Eq. (77) can be expressed in terms of the combinations of three stress invariants  $I_1, J_2, J_3$  where  $I_1$  denotes the first invariant of the stress tensor  $\underline{\underline{\sigma}}$ , whereas  $J_2, J_3$  are the second and third invariants of the deviatoric stress  $\underline{\underline{s}}$ , respectively. Thus, Eq. (77) can be replaced by:

$$f(I_1, J_2, J_3, k_1, k_2, \dots) = 0 \quad (78)$$

The yield criteria of the materials should be determined experimentally. An important experimental fact for ductile metals, shown by Bridgman and others (e.g. Hill, 1950), is that the influence of the hydrostatic pressure on yielding can be neglected. The absence of the hydrostatic pressure means that the yield function can be reduced to the form:

$$f(J_2, J_3, k_1, k_2, \dots) = 0 \quad (79)$$

The Huber-Mises-Hencky (HMH) criterion is based on the maximum distortion energy criterion, and has the form:

$$f(J_2) = J_2 - \tau_0^2 = 0 \quad (80)$$

or

$$f(J_2) = J_2 - \left(\frac{\sigma_0}{\sqrt{3}}\right)^2 = 0 \quad (81)$$

where

$$J_2 = \frac{1}{2} \underline{\underline{s}} : \underline{\underline{s}} \quad \text{or} \quad J_2 = \frac{1}{2} s_{ij} s_{ij} \quad (82)$$

Hence, the yield criterion takes the form:

$$f(J_2) = \sqrt{\frac{3}{2} \underline{s} : \underline{s}} - \sigma_0 = 0 \quad (83)$$

where  $\underline{s}$  is the deviatoric part of stress tensor  $\underline{\sigma}$ , defined in Eq. (57). The yield surface evolves during the plastic flow. Changes can be controlled by the kinematic and the isotropic hardening variables. Hence, for the material with the kinematic and the isotropic hardening one obtains:

$$f(J_2, \underline{X}, R) = J_2(\underline{\sigma} - \underline{X}) - R - \tau_0 = 0 \quad (84)$$

where

$$J_2(\underline{\sigma} - \underline{X}) = \frac{1}{2}(\underline{s} - \underline{X}) : (\underline{s} - \underline{X}) \quad (85)$$

Substituting (85) to (84), one obtains:

$$f(J_2, \underline{X}, R) = \sqrt{\frac{3}{2}(\underline{s} - \underline{X}) : (\underline{s} - \underline{X})} - R - \sigma_0 = 0 \quad (86)$$

### 5.2.5. The associated flow rule

The flow rule is a “kinematic assumption” postulated for the plastic flow. It defines direction of the plastic strain increment  $d\underline{\varepsilon}^p$  in the stress space. In 1928 von Mises postulated the concept of the plastic potential function  $g(\underline{\sigma})$ , similarly to the elastic potential function (or complementary energy density function). Since the elastic strain can be derived by differentiating the elastic potential function (or complementary energy density function) with respect to the stress tensor  $\underline{\sigma}$ , the components of the plastic strain increment  $d\underline{\varepsilon}^p$  can be defined based on the following equation:

$$d\underline{\varepsilon}^p = \frac{\partial g(\underline{\sigma})}{\partial \underline{\sigma}} d\lambda \quad (87)$$

where  $d\lambda$  is a positive scalar factor of proportionality, which is only nonzero when the plastic deformation occurs. If the potential function  $g$  is equal to the yield function  $f$ , Eq. (87) is called the associated flow rule and has the form:

$$d\underline{\varepsilon}^p = \frac{\partial f(\underline{\sigma})}{\partial \underline{\sigma}} d\lambda \quad (88)$$

otherwise, if  $g \neq f$ , the nonassociated flow rule appears. In the present case, the yield function  $f$  is defined by Eq. (86), hence:

$$\frac{\partial f}{\partial \underline{\underline{\underline{\sigma}}}} = \frac{\partial f}{\partial (J_2)} \frac{\partial (J_2)}{\partial (\underline{\underline{\underline{s}}} - \underline{\underline{\underline{X}}})} \frac{\partial (\underline{\underline{\underline{s}}} - \underline{\underline{\underline{X}}})}{\partial (\underline{\underline{\underline{\sigma}}})} \quad (89)$$

where

$$\frac{\partial f}{\partial (J_2)} = \frac{\frac{3}{2}}{\sqrt{\frac{3}{2}(\underline{\underline{\underline{s}}} - \underline{\underline{\underline{X}}}) : (\underline{\underline{\underline{s}}} - \underline{\underline{\underline{X}}})}} \quad (90)$$

and

$$\frac{\partial (J_2)}{\partial (\underline{\underline{\underline{s}}} - \underline{\underline{\underline{X}}})} = \underline{\underline{\underline{s}}} - \underline{\underline{\underline{X}}} \quad (91)$$

The deviatoric stress has been defined in Eq. (57), thus:

$$\frac{\partial (\underline{\underline{\underline{s}}} - \underline{\underline{\underline{X}}})}{\partial \underline{\underline{\underline{\sigma}}}} = \frac{\partial \left( \underline{\underline{\underline{\sigma}}} - \frac{1}{3} \text{Tr}(\underline{\underline{\underline{\sigma}}}) \underline{\underline{\underline{I}}} \right)}{\partial \underline{\underline{\underline{\sigma}}}} = \frac{\partial \underline{\underline{\underline{\sigma}}}}{\partial \underline{\underline{\underline{\sigma}}}} - \frac{\partial \left( \frac{1}{3} \text{Tr}(\underline{\underline{\underline{\sigma}}}) \underline{\underline{\underline{I}}} \right)}{\partial \underline{\underline{\underline{\sigma}}}} = \underline{\underline{\underline{I}}} - \underline{\underline{\underline{J}}} = \underline{\underline{\underline{K}}} \quad (92)$$

alternatively, it may be rewritten using summation notation:

$$\frac{\partial (S_{pq} - X_{pq})}{\partial \sigma_{ij}} = \frac{\partial \left( \sigma_{pq} - \frac{1}{3} \sigma_{kk} \delta_{pq} \right)}{\partial \sigma_{ij}} = \frac{\partial \sigma_{pq}}{\partial \sigma_{ij}} - \frac{\partial \left( \frac{1}{3} \sigma_{kk} \delta_{pq} \right)}{\partial \sigma_{ij}} = \frac{1}{2} (\delta_{pi} \delta_{qj} + \delta_{pj} \delta_{qi}) - \frac{1}{3} \delta_{ki} \delta_{kj} \delta_{pq} = J_{ijkl}^{dev} \quad (93)$$

where  $\underline{\underline{\underline{K}}}$  or  $J_{ijkl}^{dev}$  denote the deviatoric part of the identity tensor  $\underline{\underline{\underline{I}}}$  or  $J_{ijkl} = \frac{1}{2} (\delta_{ik} \delta_{jl} + \delta_{il} \delta_{jk})$ ,

respectively. Substituting (92), (91) and (90) to (89), one obtains:

$$\frac{\partial f}{\partial \underline{\underline{\underline{\sigma}}}} = \frac{3}{2} \frac{(\underline{\underline{\underline{s}}} - \underline{\underline{\underline{X}}})}{\sqrt{\frac{3}{2}(\underline{\underline{\underline{s}}} - \underline{\underline{\underline{X}}}) : (\underline{\underline{\underline{s}}} - \underline{\underline{\underline{X}}})}} \quad (94)$$

Finally, the associated plastic flow rule (88) can be expressed in the following form:

$$\underline{\underline{\underline{\dot{\epsilon}}}}^p = \frac{3}{2} \frac{(\underline{\underline{\underline{s}}} - \underline{\underline{\underline{X}}})}{\sqrt{\frac{3}{2}(\underline{\underline{\underline{s}}} - \underline{\underline{\underline{X}}}) : (\underline{\underline{\underline{s}}} - \underline{\underline{\underline{X}}})}} \dot{\lambda} \quad (95)$$

The plastic multiplier  $\dot{\lambda}$  can be calculated based on the consistency condition. In the elastic domain, the yield function remains negative and rate of the plastic multiplier  $\dot{\lambda} = 0$ , whereas in

the plastic domain the yield function is zero and the rate  $\dot{\lambda}$  is positive. Both cases are involved in the loading-unloading condition:

$$\dot{\lambda} \geq 0, f(\underline{\underline{\sigma}}) \leq 0, \dot{\lambda} f(\underline{\underline{\sigma}}) = 0 \quad (96)$$

From the mathematical point of view, these conditions are the so-called Kuhn-Tucker conditions. During the plastic flow, the stress remains on the yield surface. Consequently, the time derivative of the yield function  $\dot{f}$  vanishes, whenever the rate of the plastic multiplier  $\dot{\lambda} \neq 0$ . Thus, the consistency condition has the form:

$$\dot{f} \dot{\lambda} = 0 \quad (97)$$

It is known, that in the plastic regime the yield function must be equal to zero (the stress remains on the yield surface), and the rate of the plastic multiplier is positive. Thus, for the plastic regime the consistency condition reads:

$$\dot{f}(\underline{\underline{\sigma}}, \underline{\underline{X}}, R) = \frac{\partial f}{\partial \underline{\underline{\sigma}}} \dot{\underline{\underline{\sigma}}} + \frac{\partial f}{\partial \underline{\underline{X}}} \dot{\underline{\underline{X}}} + \frac{\partial f}{\partial R} \dot{R} = 0 \quad (98)$$

The derivative  $\frac{\partial f}{\partial \underline{\underline{\sigma}}}$  has been already calculated (Eq. (94)), whereas the derivative  $\frac{\partial f}{\partial \underline{\underline{X}}}$  can be expressed as:

$$\frac{\partial f}{\partial \underline{\underline{X}}} = \frac{\partial f}{\partial (J_2)} \frac{\partial (J_2)}{\partial (\underline{\underline{s}} - \underline{\underline{X}})} \frac{\partial (\underline{\underline{s}} - \underline{\underline{X}})}{\partial (\underline{\underline{X}})} = -\frac{3}{2} \frac{\underline{\underline{s}} - \underline{\underline{X}}}{\sqrt{\frac{3}{2} (\underline{\underline{s}} - \underline{\underline{X}}) : (\underline{\underline{s}} - \underline{\underline{X}})}} = -\frac{\partial f}{\partial \underline{\underline{\sigma}}} \quad (99)$$

The last expression in Eq. (98) can be rewritten as:

$$\frac{\partial f}{\partial R} = \frac{\partial f}{\partial (J_2)} \frac{\partial (J_2)}{\partial (\underline{\underline{s}} - \underline{\underline{X}})} \frac{\partial (\underline{\underline{s}} - \underline{\underline{X}})}{\partial R} - \frac{\partial \sigma_0}{\partial R} - \frac{\partial R}{\partial R} = -1 \quad (100)$$

Substituting Eqs (94), (99) and (100) to Eq. (98) the consistency condition reads:

$$\dot{f}(\underline{\underline{\sigma}}, \underline{\underline{X}}, R) = \frac{3}{2} \frac{(\underline{\underline{s}} - \underline{\underline{X}})}{\sqrt{\frac{3}{2} (\underline{\underline{s}} - \underline{\underline{X}}) : (\underline{\underline{s}} - \underline{\underline{X}})}} : (\dot{\underline{\underline{\sigma}}} - \dot{\underline{\underline{X}}}) - \dot{R} = 0 \quad (101)$$

Then,  $\dot{\underline{\underline{\sigma}}}, \dot{\underline{\underline{X}}}, \dot{R}$  can be determined based on Eqs (53), (60), (61). Thus, one obtains:

$$\dot{\underline{\underline{\sigma}}} = E : \left( \dot{\underline{\underline{\varepsilon}}} - \dot{\underline{\underline{\varepsilon}}}^p - \dot{\underline{\underline{\varepsilon}}}^{th} - \dot{\underline{\underline{\varepsilon}}}^{bs} \right) \quad (102)$$

Where  $\underline{\underline{\dot{\varepsilon}}}^{bs} = \frac{1}{3} \underline{\underline{\dot{\xi}}} \Delta v I$ , and it is assumed that  $\underline{\underline{\dot{\varepsilon}}}^{th} = \underline{\underline{0}}$ , therefore:

$$\underline{\underline{\dot{\sigma}}} = \underline{\underline{E}} : \left( \underline{\underline{\dot{\varepsilon}}} - \frac{3}{2} \frac{(\underline{\underline{s}} - \underline{\underline{X}})}{\sqrt{\frac{3}{2}(\underline{\underline{s}} - \underline{\underline{X}}) : (\underline{\underline{s}} - \underline{\underline{X}})}} \lambda - \frac{1}{3} \underline{\underline{\dot{\xi}}} \Delta v I \right) \quad (103)$$

Recalling the evolution of the kinematic hardening variable (Eq. (60)), and the associated flow rule (Eq. (95)), the rate of the kinematic hardening variable reads:

$$\underline{\underline{\dot{X}}} = \frac{2}{3} C_x(\underline{\underline{\xi}}) \underline{\underline{\dot{\varepsilon}}}^p = \frac{(\underline{\underline{s}} - \underline{\underline{X}})}{\sqrt{\frac{3}{2}(\underline{\underline{s}} - \underline{\underline{X}}) : (\underline{\underline{s}} - \underline{\underline{X}})}} C_x(\underline{\underline{\xi}}) \dot{\lambda} \quad (104)$$

The last expression from the consistency condition (Eq. (101)) is the rate of the isotropic hardening, defined as:

$$\dot{R} = (1 - \beta) C_{a+m} \dot{p} \quad (105)$$

where the rate of the accumulated plastic strain  $\dot{p}$  takes the:

$$\dot{p} = \sqrt{\frac{2}{3} \underline{\underline{\dot{\varepsilon}}}^p : \underline{\underline{\dot{\varepsilon}}}^p} = \sqrt{\frac{(\underline{\underline{s}} - \underline{\underline{X}}) : (\underline{\underline{s}} - \underline{\underline{X}})}{(\underline{\underline{s}} - \underline{\underline{X}}) : (\underline{\underline{s}} - \underline{\underline{X}})}} \dot{\lambda}^2 = \dot{\lambda} \quad (106)$$

Thus, the rate of the accumulated plastic strain  $\dot{p}$  is equal to the plastic multiplier  $\dot{\lambda}$ . Hence, Eq. (105) is equal to:

$$\dot{R} = (1 - \beta) C_{a+m} \dot{\lambda} \quad (107)$$

Substituting time derivatives  $\underline{\underline{\dot{\sigma}}}$  (Eq. (103)),  $\underline{\underline{\dot{X}}}$  (104) and  $\dot{R}$  (Eq. (107)) into the consistency condition, formula (Eq. (101)), one obtains:

$$\dot{f}(\underline{\underline{\sigma}}, \underline{\underline{X}}, R) = \frac{3}{2} \frac{(\underline{\underline{s}} - \underline{\underline{X}})}{\sqrt{\frac{3}{2}(\underline{\underline{s}} - \underline{\underline{X}}) : (\underline{\underline{s}} - \underline{\underline{X}})}} : \left[ \underline{\underline{E}} : \left( \underline{\underline{\dot{\varepsilon}}} - \frac{3}{2} \frac{(\underline{\underline{s}} - \underline{\underline{X}}) \dot{\lambda}}{\sqrt{\frac{3}{2}(\underline{\underline{s}} - \underline{\underline{X}}) : (\underline{\underline{s}} - \underline{\underline{X}})}} - \frac{1}{3} \underline{\underline{\dot{\xi}}} \Delta v I \right) - \left( \frac{(\underline{\underline{s}} - \underline{\underline{X}}) C_x(\underline{\underline{\xi}}) \dot{\lambda}}{\sqrt{\frac{3}{2}(\underline{\underline{s}} - \underline{\underline{X}}) : (\underline{\underline{s}} - \underline{\underline{X}})}} \right) \right] - (1 - \beta) C_{a+m} \dot{\lambda} = 0 \quad (108)$$

Hence, the plastic multiplier is obtained:

$$\dot{\lambda} = \frac{\frac{3}{2} \frac{(\underline{\underline{s}} - \underline{\underline{X}})}{\sqrt{\frac{3}{2}(\underline{\underline{s}} - \underline{\underline{X}}) : (\underline{\underline{s}} - \underline{\underline{X}})}} : \underline{\underline{E}} : \left( \underline{\underline{\dot{\varepsilon}}} - \frac{1}{3} \underline{\underline{\dot{\xi}}} \Delta v I \right)}{\frac{3}{2} \frac{(\underline{\underline{s}} - \underline{\underline{X}})}{\sqrt{\frac{3}{2}(\underline{\underline{s}} - \underline{\underline{X}}) : (\underline{\underline{s}} - \underline{\underline{X}})}} : \underline{\underline{E}} : \frac{3}{2} \frac{(\underline{\underline{s}} - \underline{\underline{X}})}{\sqrt{\frac{3}{2}(\underline{\underline{s}} - \underline{\underline{X}}) : (\underline{\underline{s}} - \underline{\underline{X}})}} + C_x(\underline{\underline{\xi}}) + (1 - \beta) C_{a+m}} \quad (109)$$

In general, the incremental form of the plastic multiplier can be expressed as:

$$d\lambda = \frac{\frac{\partial f}{\partial \sigma_{kl}} E_{klmn} \left( d\varepsilon_{mn} - \frac{1}{3} d\xi \Delta v \delta_{mn} \right)}{\frac{\partial f}{\partial \sigma_{op}} \frac{\partial f}{\partial \sigma_{rs}} E_{oprs} + C_x(\xi) + (1-\beta)C_{a+m}} \quad (110)$$

where  $f$  defines the yield function,  $d\xi$  is the increment of the volume fraction of martensite,  $\Delta v$  denotes the relative volume change during  $\gamma - \alpha'$  phase transformation (Eq. (65)),  $\delta_{mn}$  is the 2<sup>nd</sup> order identity tensor,  $C_{a+m}$ ,  $C_x(\xi)$  are the homogenised and the kinematic hardening moduli, respectively.

### 5.2.6. Evolution of the hardening variables

During plastic flow of ductile materials (such as austenitic stainless steels) at a temperature near 0 K, the hardening effect is observed (cf. Fig. 37). From the microscopic point of view, during the plastic deformation, the martensitic embryos (new harder phase) occur in the austenitic matrix. Therefore, the mobile dislocations in the austenitic matrix are stopped by the martensite inclusions as well as by the immobile dislocations (e.g. forest dislocations). Thus, the elastic-plastic matrix and the elastic inclusions are the principal components that constitute the two phase material model (Garion, 2003). In the RVE based constitutive description of the phase transformation, the hardening model is represented by the kinematic part related to the back stress  $\underline{\underline{X}}$ , and the isotropic part represented by the hardening parameter  $R$ . Both, the kinematic and the isotropic hardening variables are affected by the evolution of the martensitic phase during the plastic deformation. Thus, the evolution laws of the hardening variables can be postulated in the following incremental form for the kinematic hardening:

$$d\underline{\underline{X}} = d\underline{\underline{X}}_{a0} + d\underline{\underline{X}}_{a\xi} + d\underline{\underline{X}}_{a+m} = \frac{2}{3} C_x(\xi) d\underline{\underline{\varepsilon}}^p = \frac{2}{3} (C_{a0} + C_{a0} h \xi + \beta C_{a+m}) \dot{\underline{\underline{\varepsilon}}}^p \quad (111)$$

and for the isotropic hardening:

$$dR = C_R(\xi) dp \quad (112)$$

where  $C_{a0}$  is the hardening modulus of pure austenite,  $h$  is the material dependent parameter, reflecting the interaction between the dislocations and the martensite inclusions,  $C_R(\xi) = (1-\beta)C_{a+m}$ . Here,  $\beta$  denotes the Bauschinger parameter,  $C_{a+m}$  is the homogenised

modulus (or the so-called surplus tangent stiffness modulus), and  $dp$  is the increment of the accumulated plastic strain.

### 5.2.6.1 Kinematic hardening

Based on the experimental results obtained during the uniaxial tensile tests and the microscopic analysis, it can be concluded that the back-stress increment is composed of three contributions:

- Strain hardening of the original, non-transformed, purely austenitic phase, due to the interactions between dislocations. In the stress-strain curve of uniaxial tensile test this effect is represented by tangent modulus  $C_{a0}$  (Fig. 44).
- The hardening effect caused by the Orowan mechanism: interactions between the dislocations and the martensitic inclusions in the austenitic matrix. In the uniaxial tests, this effect is represented by the tangential modulus  $C_{a\xi}$  (Fig. 44).
- The last contribution in Eq. (111) is associated with the properties of the austenite matrix and the martensite inclusions, resulting from the homogenisation process. In the stress-strain curve of the uniaxial tensile test, this effect is represented by tangent modulus  $C_{a+m}$  (Fig. 44b).

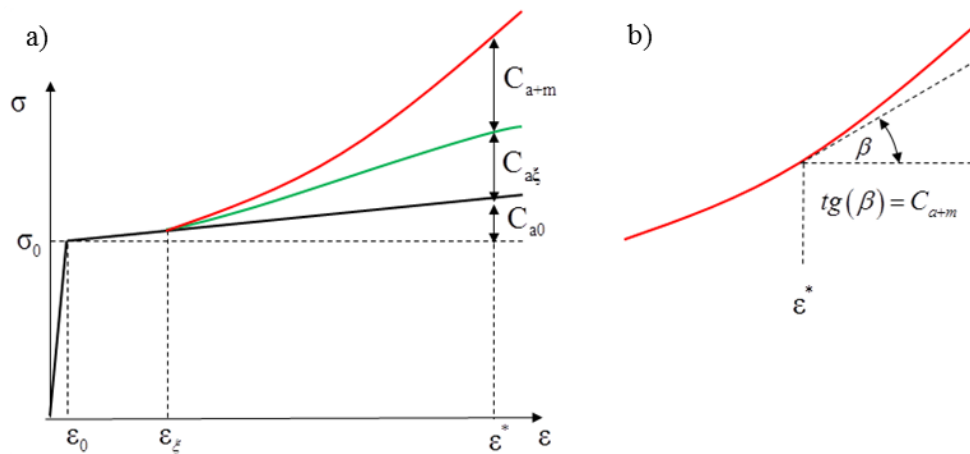


Fig. 44 a) Uniaxial tensile test results: the stress-strain curve with the hardening effect; b) definition of linearised tangent moduli

The expression  $d\underline{X}_{a0}$  in Eq. (111) represents hardening of pure austenite due to the interactions between the dislocations (e.g. interactions between mobile dislocations and forest dislocation), and can be postulated in the following incremental form:

$$d\underline{\underline{X}}_{a0} = \frac{2}{3} C_{a0} d\underline{\underline{\varepsilon}}^p \quad (113)$$

This part of kinematic hardening is proportional to the increment of the plastic strain tensor  $\underline{\underline{\varepsilon}}^p$ . Tangent modulus of pure austenite  $C_{a0}$  can be experimentally identified.

The second expression  $d\underline{\underline{X}}_{a\xi}$  in Eq. (111) represents the back stress related to the Orowan mechanism. It results from the interaction between the mobile dislocations and the martensitic inclusions. The mobile dislocations are blocked by the martensitic inclusions. Skoczeń (2007) shows, that the shear stress necessary for a dislocation to pass across two martensitic inclusions (or embryos) with the average size  $d$ , separated by distance  $l$ , depends linearly on the volume fraction of martensite  $\xi$  (Fig. 45):

$$\tau_p = \mu \frac{b}{d} \left( \frac{6\xi_0}{\pi} \right)^{\frac{1}{3}} \left( 1 + \frac{\Delta\xi}{\xi_0} \right)^{\frac{1}{3}} \quad (114)$$

where  $\mu$  denotes the shear modulus of the austenite,  $b$  is the Burgers vector,  $\xi_0$  is the initial volume fraction of the inclusions,  $\Delta\xi$  denotes the increment of the volume fraction of new phase. Eq. (114) was derived from the assumption that the average size of inclusion  $d$  (Fig. 45) is constant, and much smaller than the distance between two inclusions ( $d \ll l$ ).

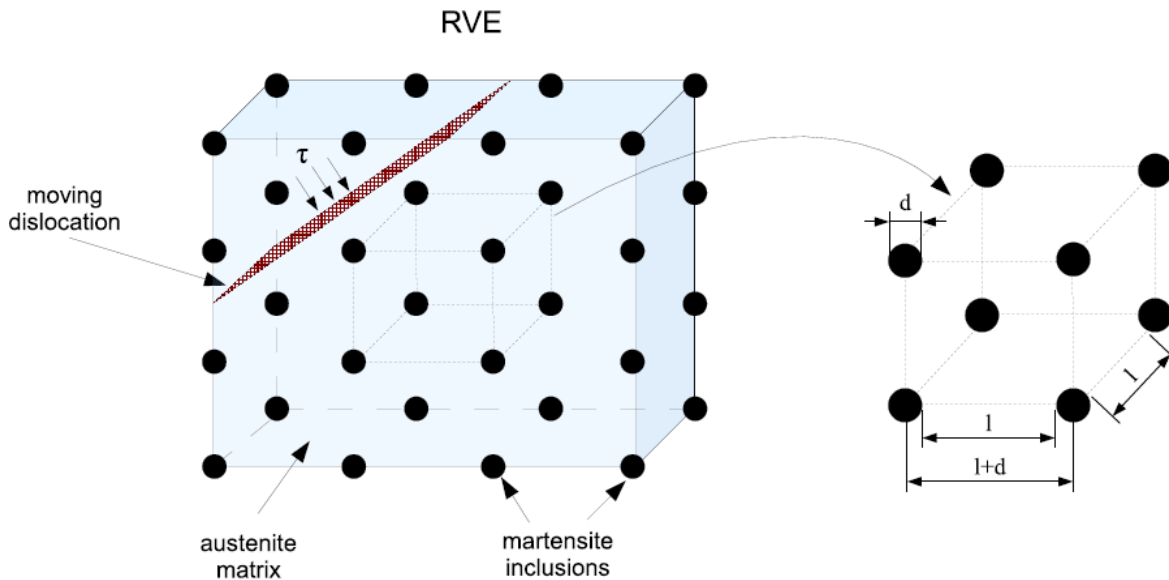


Fig. 45 The Orowan mechanism. RVE with a dislocation that is blocked by the martensitic inclusions (Sitko et al., 2010)

Moreover, in order to linearise the shear stress formula, the expression  $\left(1 + \frac{\Delta\xi}{\xi_0}\right)^{\frac{1}{3}}$  was expanded in Taylor series (Eq. (114)). Thus, the final expression for the shear stress reads:

$$\tau_p = \mu \frac{b}{d} \left(\frac{6\xi}{\pi}\right)^{\frac{1}{3}} \left(1 + \frac{\xi - \xi_0}{3\xi_0}\right) \quad (115)$$

In the case of two-phase material, the shear stress  $\tau_p$  becomes an approximately linear function of the volume fraction of martensite (Skoczeń, 2007). Moreover, due to the Orowan mechanism, the hardening modulus  $C_{a0}$  of pure austenite is replaced by the tangent modulus  $C_a(\xi)$  expressed as:

$$C_a(\xi) = C_{a0}\phi(\xi) \text{ for } 0 \leq \xi \leq \xi_L \text{ and } \phi(0) = 1 \quad (116)$$

In the light of (115), the function  $\phi(\xi)$  takes the linear form:

$$\phi(\xi) = 1 + h\xi \quad (117)$$

where  $h$  is a material dependent parameter, reflecting the interactions between the dislocations and the inclusions. This parameter can be obtained experimentally. The function  $\phi(\xi)$  can be interpreted as a part of the hardening process, that corresponds to the increase of the volume fraction of martensite. The higher the volume fraction of martensite, the more hardening occurs, since the probability that a dislocation will stack on an inclusion increases. Thus, the expression  $d\underline{X}_{a0} + d\underline{X}_{a\xi}$  in Eq. (111), that reflects the total back stress in the elasto-plastic austenite, can be expressed as:

$$d\underline{X}_a = d\underline{X}_{a0} + d\underline{X}_{a\xi} = \frac{2}{3}C_a(\xi)d\underline{\varepsilon}^p = \frac{2}{3}C_{a0}\phi(\xi)d\underline{\varepsilon}^p = \frac{2}{3}C_{a0}(1 + h\xi)d\underline{\varepsilon}^p \quad (118)$$

For pure austenitic phase, a linearization of the stress-strain relation in the vicinity of the current state, leads to the following formula (Sitko et al., 2010):

$$\Delta\underline{\sigma}_a = \underline{E}_{ta} : \Delta\underline{\varepsilon} \quad (119)$$

where  $\underline{E}_{ta}$  is the tangent stiffness tensor of austenite. Similar approach can be applied in the case of two-phase continuum:

$$\Delta\underline{\sigma} = \underline{E}_H : \Delta\underline{\varepsilon} \quad (120)$$

However, in this case, the tangent stiffness tensor  $\underline{\underline{E}}_H$  is based on the homogenisation process.

Due to the fact, that a mixture of old and new phase occurs, an additional hardening increment in the stress relations is postulated:

$$\Delta \underline{\underline{\sigma}} = \Delta \underline{\underline{\sigma}}_a + \Delta \underline{\underline{\sigma}}_{a+m} = \underline{\underline{E}}_{ta} : \Delta \underline{\underline{\varepsilon}} + \left( \underline{\underline{E}}_H - \underline{\underline{E}}_{ta} \right) : \Delta \underline{\underline{\varepsilon}} \quad (121)$$

The same “trial” increment is assumed for pure austenite and for the homogenised two-phase continuum in order to calculate the macroscopic stress during the strain controlled process. It is assumed, that kinematically controlled  $\gamma - \alpha'$  phase transformation is considered (Sitko et al., 2010). The local linearised tangent stiffness tensor of elasto-plastic austenite  $\underline{\underline{E}}_{ta}$  in Eq. (121) can

be expressed as (Sitko and Skoczeń, 2012):

$$\underline{\underline{E}}_{ta} = 3k_{ta} \underline{\underline{J}} + 2\mu_{ta} \left( \underline{\underline{K}} - \frac{\underline{\underline{n}} \otimes \underline{\underline{n}}}{1 + \frac{C}{3\mu}} \right) \quad (122)$$

where  $k_{ta}$  denotes the bulk modulus,  $\mu_{ta}$  denotes the shear modulus of the elasto-plastic austenite,  $C$  is the hardening modulus of the austenitic phase, and  $\mu$  is the shear modulus of the austenite. Here,  $\underline{\underline{J}}$  and  $\underline{\underline{K}}$  are the 4<sup>th</sup> rank projectors defined, respectively, as volumetric and deviatoric part of symmetric 4<sup>th</sup> order identity tensor  $\underline{\underline{I}}$  (in the indicial notation expressed as:

$J_{ijkl}^{sym} = \frac{1}{2}(\delta_{ik}\delta_{jl} + \delta_{il}\delta_{jk})$ ). Hence, one obtains:

$$\underline{\underline{J}} = \frac{1}{3} \underline{\underline{I}} \otimes \underline{\underline{I}} \quad \text{or} \quad J_{ijkl}^{vol} = \frac{1}{3} \delta_{ik} \delta_{jl} \quad (123)$$

$$\underline{\underline{K}} = \underline{\underline{I}} - \underline{\underline{J}} \quad \text{or} \quad J_{ijkl}^{dev} = \frac{1}{2}(\delta_{ik}\delta_{jl} + \delta_{il}\delta_{jk}) - \frac{1}{3} \delta_{ik} \delta_{jl} \quad (124)$$

In Eq. (122),  $\underline{\underline{n}}$  denotes the tensor normal to the yield surface, that can be expressed as:

$$\underline{\underline{n}} = \frac{\partial f}{\partial \underline{\underline{\sigma}}} = \frac{3}{2} \frac{(\underline{\underline{s}} - \underline{\underline{X}})}{\sqrt{\frac{3}{2}(\underline{\underline{s}} - \underline{\underline{X}}) : (\underline{\underline{s}} - \underline{\underline{X}})}} \quad \text{or} \quad n_{ij} = \frac{\partial f}{\partial \sigma_{ij}} = \frac{3}{2} \frac{(s_{ij} - X_{ij})}{\sqrt{\frac{3}{2}(s_{kl} - X_{kl})(s_{kl} - X_{kl})}} \quad (125)$$

Doghri et al. (2003, 2005) stated that the elastic-plastic tangent stiffness (Eq. (122)) can be reduced to an isotropic form. Thus, the nonlinear expression in Eq. (122) can be stripped down.

Hence:

$$\underline{\underline{E_{ta}}} = 3k_{ta}\underline{\underline{J}} + 2\mu_{ta}\underline{\underline{K}} \quad (126)$$

where

$$k_{ta} = \frac{E_{ta}}{2(1+\nu_a)}, \quad \mu_{ta} = \frac{E_{ta}}{3(1-2\nu_a)} \quad (127)$$

$\nu_a$  is the Poisson ratio of austenite, and  $E_{ta}$  denotes one-dimensional tangent modulus of the austenite. For the uniaxial tensile test (plastic range) the stress rate remains in the following relation to strain rate:

$$\dot{\sigma} = E_{ta}\dot{\varepsilon} \quad (128)$$

Based on the Hook law, the stress rate has the following form:

$$\dot{\sigma} = E(\dot{\varepsilon} - \dot{\varepsilon}^p) \quad (129)$$

where  $E$  is the elastic modulus of the austenite. The rate of the plastic strain  $\dot{\varepsilon}^p$  can be calculated from the associated flow rule:

$$\dot{\varepsilon}^p = \frac{\partial f}{\partial \sigma} \dot{\lambda} \quad (130)$$

where  $\dot{\lambda}$  is the plastic strain multiplier. Here, it has been assumed that the yield function is represented without the hardening effect (model perfectly plastic), thus:

$$f(\sigma, \sigma_0) = \sigma - \sigma_0 \quad (131)$$

Substituting Eq. (131) to Eq. (130), one obtains:

$$\dot{\varepsilon}^p = \frac{\partial(\sigma - \sigma_0)}{\partial \sigma} \dot{\lambda} = \dot{\lambda} \quad (132)$$

In the elastic domain, the yield function remains negative and the rate of the plastic multiplier  $\dot{\lambda} = 0$ , whereas in the plastic domain the yield function is equal to zero, and  $\dot{\lambda}$  is positive. Both cases are involved in the loading-unloading condition:

$$\dot{\lambda} \geq 0, \quad f(\sigma) \leq 0, \quad \dot{\lambda} f(\sigma) = 0 \quad (133)$$

As already stated, these relations are the Kuhn-Tucker conditions. During the plastic flow, the stress state remains on the yield surface. Consequently, the time derivative of the yield function  $\dot{f}$  vanishes, whenever the rate of the plastic multiplier  $\dot{\lambda} \neq 0$ . Thus, the consistency condition takes the form:

$$\dot{\lambda} \dot{f} = 0 \quad (134)$$

Moreover, during the plastic process, Eq. (134) reduces to the form  $\dot{f} = 0$ :

$$\dot{f} = \frac{\partial \sigma}{\partial t} - \frac{\partial \sigma_0}{\partial \varepsilon^p} \frac{\partial \varepsilon^p}{\partial t} = \dot{\sigma} - H \dot{\varepsilon}^p = 0 \quad (135)$$

where  $H$  is the hardening modulus of austenite. Thus, Eq. (135) can be rewritten as:

$$\dot{\sigma} = H \dot{\varepsilon}^p \quad (136)$$

Knowing that  $\dot{\varepsilon}^p = \dot{\lambda}$  (Eq. (132)), and substituting Eq. (129) to (136), one obtains:

$$E(\dot{\varepsilon} - \dot{\lambda}) = H \dot{\lambda} \quad (137)$$

The plastic multiplier  $\dot{\lambda}$  can be calculated as:

$$\dot{\lambda} = \frac{E \dot{\varepsilon}}{H + E} \quad (138)$$

Inserting Eqs (129), (130), (138) into Eq. (128), one obtains:

$$E_{ia} = \frac{EH}{E + H} \quad (139)$$

In the present case, the hardening modulus  $H$  is related to the interaction between the mobile dislocations and the immobile ones, as well as to the Orowan mechanism. Therefore, based on Eq. (116):

$$H = C_a(\xi) = C_{a0}(1 + h\xi) \quad (140)$$

Finally, the tangent modulus of austenite is expressed as:

$$E_{ia} = \frac{E_a \cdot C_a(\xi)}{E_a + C_a(\xi)} = \frac{E_a \cdot C_{a0}(1 + h\xi)}{E_a + C_{a0}(1 + h\xi)} \quad (141)$$

The elasticity tensor of martensite has an isotropic form, and is defined as follows:

$$\underline{\underline{E}}_m = 3k_m \underline{\underline{J}} + 2\mu_m \underline{\underline{K}} \quad (142)$$

where  $k_m, \mu_m$  denote, respectively, the bulk and the shear moduli of elastic martensite:

$$k_m = \frac{E_m}{2(1 + \nu_m)}, \quad \mu_m = \frac{E_m}{3(1 - 2\nu_m)} \quad (143)$$

The inclusions are assumed ellipsoidal, and uniformly distributed in the matrix. The problem of single ellipsoidal inclusion, embedded in an infinite homogeneous matrix and subjected to uniform transformation strain, was solved by Eshelby (1957) who concluded, that the stresses and the strains within the inclusion can be effectively derived. This solution became a basis of the main homogenisation algorithms, such as the self-consistent (Hill, 1965) or the Mori–Tanaka (M-T algorithm), (Mori and Tanaka, 1973). In order to identify the tangent stiffness tensor of two-

phase continuum  $\underline{\underline{E}}_H$  (see Eq. (121)), the Mori–Tanaka homogenisation scheme was used (Garion and Skoczen, 2002; Garion et al., 2006):

$$\underline{\underline{E}}_H = \underline{\underline{E}}_{MT} = 3k_{MT} \underline{\underline{J}} + 2\mu_{MT} \underline{\underline{K}} \quad (144)$$

where  $\underline{\underline{E}}_H$  is calculated from the following formula:

$$\left[ \underline{\underline{E}}_{MT} + \underline{\underline{E}}^* \right]^{-1} = \sum f_i \left[ \underline{\underline{E}}_i + \underline{\underline{E}}^* \right]^{-1} \quad (145)$$

where  $f_i$  is the volume fraction of  $i$  phase,  $\underline{\underline{E}}^*$  denotes the Hill influence tensor. In the case of two-phase continuum, one obtains:

$$\left[ \underline{\underline{E}}_{MT} + \underline{\underline{E}}^* \right]^{-1} = f_a \left[ \underline{\underline{E}}_{ta} + \underline{\underline{E}}^* \right]^{-1} + f_m \left[ \underline{\underline{E}}_m + \underline{\underline{E}}^* \right]^{-1} \quad (146)$$

where  $f_a, f_m$  are the volume fractions of austenite and martensite, respectively. In view of the fact that  $f_m = \xi$  (see Eq. (50)), Eq. (146) becomes:

$$\left[ \underline{\underline{E}}_{MT} + \underline{\underline{E}}^* \right]^{-1} = (1 - \xi) \left[ \underline{\underline{E}}_{ta} + \underline{\underline{E}}^* \right]^{-1} + \xi \left[ \underline{\underline{E}}_m + \underline{\underline{E}}^* \right]^{-1} \quad (147)$$

The Hill influence tensor  $\underline{\underline{E}}^*$  has the following isotropic form:

$$\underline{\underline{E}}^* = 3k^* \underline{\underline{J}} + 2\mu^* \underline{\underline{K}} \quad (148)$$

where  $k^*$  and  $\mu^*$  denote the bulk and the shear moduli respectively, that are equal to:

$$k^* = \frac{4}{3} \mu_{ta}, \quad \mu^* = \frac{\mu_{ta} (9k_{ta} + 8\mu_{ta})}{6(k_{ta} + 2\mu_{ta})} \quad (149)$$

where  $\mu_{ta}$  and  $k_{ta}$  are defined via Eq. (127).

It is furthermore assumed, that the strain increment is mainly due to the plastic strain ( $\Delta \underline{\underline{\varepsilon}} \approx \Delta \underline{\underline{\varepsilon}}^p$ ). Therefore, the expression  $\Delta \underline{\underline{\sigma}}_{a+m}$  from Eq. (121) can be rewritten as:

$$\Delta \underline{\underline{\sigma}}_{a+m} = \left( \underline{\underline{E}}_H - \underline{\underline{E}}_{ta} \right) : \Delta \underline{\underline{\varepsilon}}^p \quad (150)$$

Inserting the expressions for  $\underline{\underline{E}}_H$  (Eq. (144)) and  $\underline{\underline{E}}_{ta}$  (Eq. (126)) to Eq. (150), one obtains:

$$\Delta \underline{\underline{\sigma}}_{a+m} = \left( 3(k_{MT} - k_{ta}) \underline{\underline{J}} + 2(\mu_{MT} - \mu_{ta}) \underline{\underline{K}} \right) : \Delta \underline{\underline{\varepsilon}}^p \quad (151)$$



Thus,  $\mu_{MT}$  in Eq. (157) is expressed as:

$$\mu_{MT} = \frac{15}{4} \frac{E_{ia}(-1+\nu_a)(20\mu_m\nu_a^2 + 5E_{ia}\nu_a + 4\mu_m\nu_a - 7E_{ia} - 16\mu_m)}{(-20\mu_m\nu_a^2\xi + 10E_{ia}\nu_a\xi - 4\mu_m\nu_a\xi + 20\mu_m\nu_a^2 - 8E_{ia}\xi + 16\mu_m\xi + 5E_{ia}\nu_a + 4\mu_m\nu_a - 7E_{ia} - 16\mu_m)(-4+5\nu_a)(1+\nu_a)} \quad (159)$$

Substituting Eqs (127) and (158) to the expression for  $C_{a+m}$  (Eq. (153)), one obtains:

$$C_{a+m} = -\frac{3}{2} \frac{\xi(-1+\nu_a)C_{a0}E_a((1+\nu_m)E_a - E_m(1+\nu_a))(h\xi+1)C_{a0} - E_aE_m(1+\nu_a)(h\xi+1)}{\left(\left(1+\nu_m\right)\left(\left(\xi+\frac{1}{2}\right)\nu_a - \frac{4}{5}\xi - \frac{7}{10}\right)E_a - E_m\left(-\frac{4}{5}+\nu_a\right)(1+\nu_a)(-1+\xi)\right)(h\xi+1)C_{a0} - E_m\left(-\frac{4}{5}+\nu_a\right)(1+\nu_a)E_a(-1+\xi)}(1+\nu_a)(E_a+C_{a0}(h\xi+1)) \quad (160)$$

The parameters from the above equation are presented in Table 7. The formula presented in Eq. (160) was obtained by means of symbolic computation, using MAPLE 17 software. For further analysis, the modulus calculated by means of Eq. (160) will be denoted as  $C_{a+m}^{III}$ . The analytical form of  $C_{a+m}$  was presented first by Skocz n, 2007, and then by Sitko et al. (2010):

$$C_{a+m}^I = \frac{5 \cdot E_a}{2 \cdot (1 + \nu_a)} \left( \frac{\eta}{(1 + \eta)} \right) \cdot \left( \frac{\xi}{(2 \cdot a \cdot (1 + \eta) + 3 \cdot \eta)} \frac{1}{(2 \cdot a \cdot (1 + \eta) - 2 \cdot \eta)^{-\xi}} \right) \quad (161)$$

where  $\eta = \frac{C_{a0} \cdot (1 + h \cdot \xi)}{E_a}$  and  $a = \frac{1 + \nu_a}{1 + \nu_m}$ . Moreover, the Author(s) assumed that  $\eta \ll 1$ , thus

$1 + \eta \approx 1$ , therefore Eq. (161) can be significantly simplified:

$$C_{a+m}^{sl} = \frac{5E_a\eta\xi}{3(1-\xi)} \quad (162)$$

The analytical form of  $C_{a+m}$  was also developed by Ortwein et al. (2016):

$$C_{a+m}^{II} = \frac{E_a \cdot C_{a0} \cdot (1 + h \cdot \xi)}{E_a + C_{a0} \cdot (1 + h \cdot \xi)} \cdot \left( \frac{\frac{15 \cdot \xi \cdot (1 - \nu_a)}{2 \cdot (4 - 5 \cdot \nu_a) \cdot (1 + \nu_a)} \left( \frac{E_m}{(1 + \nu_m)} - \frac{E_a \cdot C_{a0} \cdot (1 + h \cdot \xi)}{(E_a + C_{a0} \cdot (1 + h \cdot \xi)) \cdot (1 + \nu_a)} \right)}{\frac{E_m \cdot (1 - \xi)}{(1 + \nu_m)} + \frac{E_a \cdot C_{a0} \cdot (1 + h \cdot \xi)}{(E_a + C_{a0} \cdot (1 + h \cdot \xi)) \cdot (1 + \nu_a)}} \cdot \left( \xi + \frac{(7 - 5 \cdot \nu_a)}{2 \cdot (4 - 5 \cdot \nu_a)} \right) \right) \quad (163)$$

The material parameters of 304ss, presented in Table 7 were experimentally identified and adopted to the numerical calculations of different versions of  $C_{a+m}$ .

Table 7 The experimentally identified parameters of 304ss

<b>Parameter</b>	<b>Equation</b>	<b>Value</b>
$E_a$	elastic modulus of austenite (141)	$1.9 \cdot 10^5 \text{ MPa}$
$C_{a0}$	tangent modulus of austenite (116)	$750 \text{ MPa}$
$h$	material dependent parameter (117)	1.9
$\nu_a$	Poisson's ratio of austenite (127)	0.5
$E_m$	elastic modulus of martensite (142)	$1.9 \cdot 10^5 \text{ MPa}$
$\nu_m$	Poisson's ratio of martensite (143)	0.3
$\varepsilon_\xi$	plastic strain threshold (49)	0.004
$A$	phase transformation intensity parameter (49)	4.23

Fig. 46 presents different versions of the tangent stiffness modulus versus strain, and relative error with regard to  $C'_{a+m}$  definition (Eq. (161)).

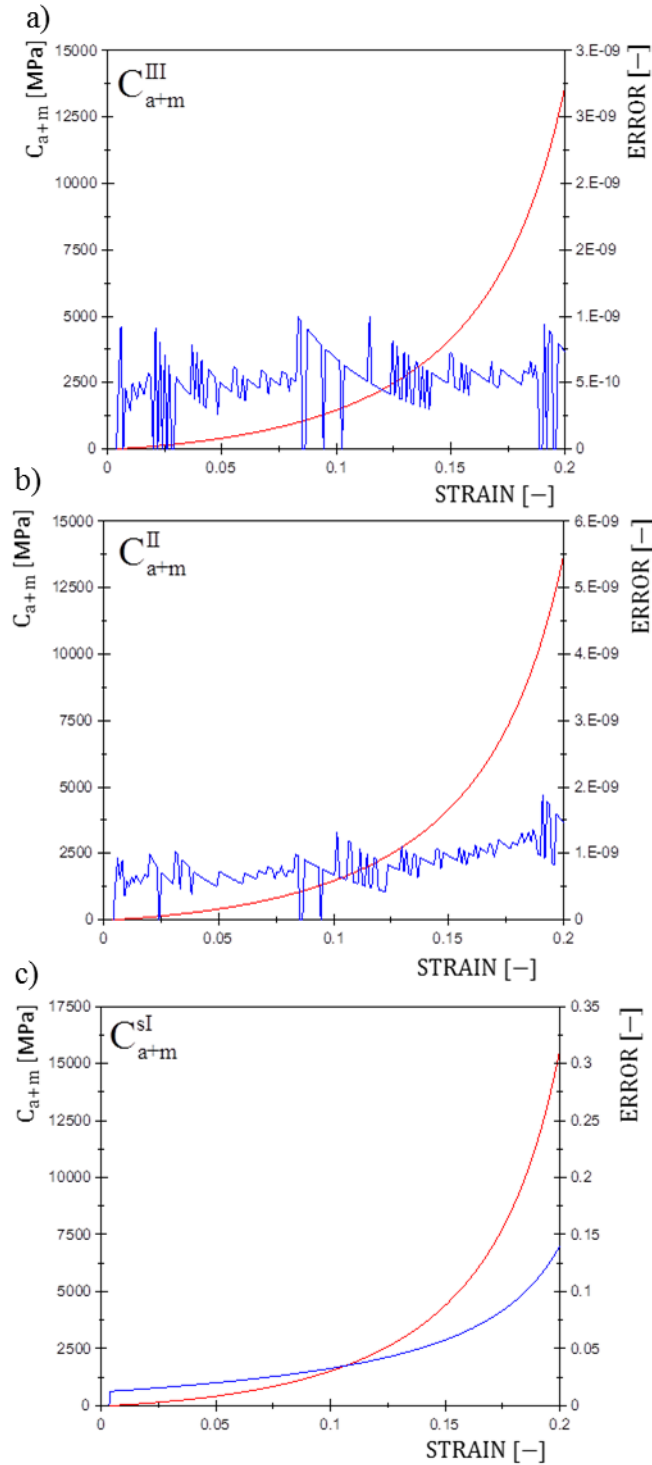


Fig. 46 Comparison of surplus tangent stiffness moduli  $C_{a+m}$ : the modulus (red) and the relative error (blue) versus strain; a) the modulus  $C_{a+m}^{III}$  (Eq. (160)); b) the modulus  $C_{a+m}^{II}$  (Eq. (163)); c) the modulus  $C_{a+m}^{sI}$  (Eq. (162)); the relative error was calculated with respect to  $C_{a+m}^I$  (Eq. (161))

Based on the above versions of surplus tangent stiffness modulus, it can be concluded that the moduli  $C_{a+m}^I, C_{a+m}^{II}, C_{a+m}^{III}$  are nearly identical. The relative error results from rounding error. On the other hand, for the simplified modulus  $C_{a+m}^{sl}$ , the relative error significantly increases when  $\varepsilon > 0.15$ . The maximum value of the error is equal to 15% for  $\varepsilon = 0.20$ .

### 5.2.6.2 Isotropic hardening

The isotropic hardening is also coupled with the phase transformation (Garion and Skoczeń, 2002, 2003). The yield stress of the martensite is much higher than the yield stress of the austenite. Thus, the isotropic hardening of two-phase continuum depends on the volume fraction of martensite. The increment of the isotropic hardening parameter is equal to the stress increment, caused by the presence of martensite in the austenitic matrix (Skoczeń, 2007):

$$\Delta R = \Delta R_{a+m} = \|\Delta \sigma_{a+m}\| = \sqrt{\frac{2}{3} \Delta \sigma_{a+m} : \Delta \sigma_{a+m}} \quad (164)$$

The stress increment  $\Delta \sigma_{a+m}$ , defined via Eq. (153), reads:

$$\Delta R = \Delta R_{a+m} = \sqrt{\left(2(\mu_{MT} - \mu_{ia})\right)^2 \frac{2}{3} \Delta \underline{\underline{\varepsilon}}^p : \Delta \underline{\underline{\varepsilon}}^p} = 2(\mu_{MT} - \mu_{ia}) \Delta p \quad (165)$$

where  $\Delta p = \sqrt{\frac{2}{3} \Delta \underline{\underline{\varepsilon}}^p : \Delta \underline{\underline{\varepsilon}}^p}$ . In the differential form, one obtains:

$$dR = dR_{a+m} = 2(\mu_{MT} - \mu_{ia}) dp = C_{a+m} dp \quad (166)$$

Thus, the increment of the isotropic hardening parameter depends on the accumulated plastic strain  $dp$ , and surplus (homogenised) tangent stiffness modulus  $C_{a+m}$ .

### 5.2.6.3 Mixed hardening

In order to establish a relation between the kinematic and the isotropic hardening, the Bauschinger parameter  $\beta$  has been introduced (Życzkowski, 1967):

$$\beta = \frac{\sigma^+ - \sigma^-}{2(\sigma^+ - \sigma_0)}, \quad 0 \leq \beta \leq 1 \quad (167)$$

where  $\sigma^+$  denotes the stress level at which the unloading process starts,  $\sigma^-$  is the yield stress at the reverse active process, and  $\sigma_0$  is the yield point (Fig. 47). The Bauschinger parameter varies between 0 (isotropic hardening, no Bauschinger effect), and 1 (kinematic hardening, pure Bauschinger effect).

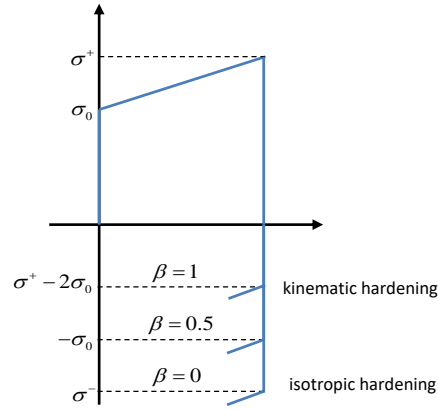


Fig. 47 Bauschinger parameter  $\beta$  and types of hardening during the loading-unloading tensile test

In view of the foregoing, the evolution of the isotropic hardening depends on the Bauschinger parameter in the following way:

$$dR = C_R(\xi) dp = (1 - \beta) C_{a+m} dp \quad (168)$$

whereas, the kinematic hardening is described by the following:

$$d\underline{X} = \frac{2}{3} C_X(\xi) d\underline{\varepsilon}^p = \frac{2}{3} (C_{a0} + C_{a0} h \xi + \beta C_{a+m}) d\underline{\varepsilon}^p \quad (169)$$

According to Ortwein (2015),  $C_x(\xi)$  can be calculated from Eq. (163):

$$C_X(\xi) = C_{a0} (1 + h\xi) \frac{(1 - \beta) E_a \cdot C_{a0} (1 + h\xi)}{2(E_a + C_{a0} (1 + h\xi))} \frac{\frac{15(1 - \nu_a) \xi}{(4 - 5\nu_a)(1 + \nu_a)} \left( \frac{E_m}{1 + \nu_m} - \frac{E_a \cdot C_{a0} (1 + h\xi)}{(E_a + C_{a0} (1 + h\xi))(1 + \nu_a)} \right)}{\left( \frac{E_m (1 - \xi)}{1 + \nu_m} + \frac{E_a \cdot C_{a0} (1 + h\xi)}{(E_a + C_{a0} (1 + h\xi))(1 + \nu_a)} \left( \xi + \frac{(7 - 5\nu_a)}{2(4 - 5\nu_a)} \right) \right)} \quad (170)$$

In order to define the kinematic and the isotropic hardening variables, integration with respect to the accumulated plastic strain and the plastic strain is required, thus:

$$R = \int_0^{p^*} (1 - \beta) C_{a+m} dp, \quad \underline{X} = \int_0^{\underline{\varepsilon}^{p^*}} \frac{2}{3} C_X(\xi) d\underline{\varepsilon}^p \quad (171)$$

where  $p^*$ ,  $\underline{\varepsilon}^{p^*}$  denote the final values of the accumulated plastic strain and the plastic strain tensor, respectively, along the loading path (Ortwein, 2015).

### 5.3. Thermodynamic model of strain localisation in DPF

It has been experimentally confirmed, that the strain induced martensitic transformation in the austenitic stainless steels significantly affects the macroscopic slip band propagation during the DPF (Section 4.3) (Tabin et al., 2015). It is worth recalling the research papers by Suzuki et al. (1977), and Brooks et al. (1979a, b). The Authors suggested that the  $\alpha'$  martensite nucleation is associated with the piling-up of the Shockley partial dislocations (such partial dislocations generate the Lomer –Cottrell locks). Moreover, Murr et al. (1982) claim that the dislocations are forced against each other in the pile-up, the continuous nucleation of the martensite occurs, and then, the growth of new phase through coalescence of its embryos takes place. Macroscopically, the experimental confirmation of such approach is presented in Fig. 48. The strain localisation effect observed during DPF is coupled with the phase transformation. It is clearly observed in the stress-temperature-strain curves of the uniaxial tensile test of 304ss at 4.2 K.

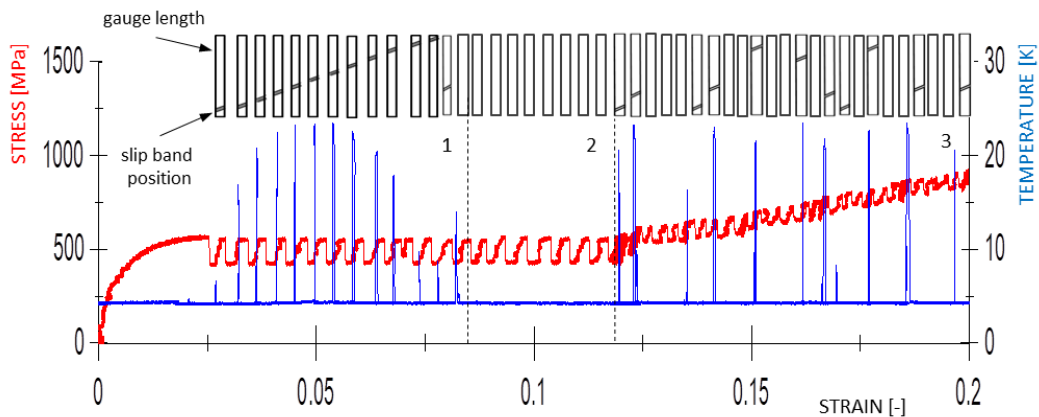


Fig. 48 Tensile test results: the stress-strain curve (red) and the temperature-strain curve (blue) for 304 stainless steel at 4.2 K; visualization of the slip band evolution along the gauge length of the specimen

The  $\gamma - \alpha'$  phase transformation significantly affects the slip band propagation. It is reflected by the temperature distribution. As already stated, the temperature distribution during region 1 (Fig. 48, without hardening) has regular form (the comb-like profile). It is observed when the slip band, propagates smoothly from one extremity of the specimen to the other. On the other hand, the temperature distribution within the hardening range (region 3, Fig. 48) is random. It is well established, that the intersecting slip systems within a slip band can be very effective strain-induced nucleation places of the martensitic phase. Thus, the initially observed regularly “travelling” slip band is “pinned” by nucleation of the martensite, and then, a new slip band occurs randomly within the specimen. From the thermodynamic point of view, the heat diffusion

equation is the starting point of the analysis of temperature distribution generated by the slip band evolution during DPF, both for region 1 and 3.

### 5.3.1. Solution of heat diffusion equation

For a flat specimen the heat diffusion equation can be markedly simplified to one-dimensional partial differential equation:

$$\frac{\partial \theta}{\partial t} = \lambda \frac{\partial^2 \theta}{\partial x^2} \quad (172)$$

$$x \in (-\infty, \infty); t \in \langle 0, \infty \rangle$$

with the following initial condition:

$$\theta(x, 0) = f(x) \quad (173)$$

$$x \in (-\infty, \infty)$$

General solution of the heat diffusion equation (172) is given by (Tichonow and Samarski, 1963):

$$\theta(x, t) = \int_{-\infty}^{\infty} C(\omega) e^{-i\omega x} e^{-\lambda \omega^2 t} d\omega \quad (174)$$

The initial condition (173) can be rewritten as:

$$\theta(x, 0) = f(x) = \int_{-\infty}^{\infty} C(\omega) e^{-i\omega x} d\omega \quad (175)$$

This equation implies that the function  $f(x)$  is the inverse Fourier transform of the function  $C(\omega)$ , which in turn implies that  $C(\omega)$  is the Fourier transform of  $f(x)$ :

$$C(\omega) = F(\omega) = \frac{1}{2\pi} \int_{-\infty}^{\infty} f(x) e^{i\omega x} dx \quad (176)$$

Substituting  $C(\omega)$  to Eq. (174), the general solution can be written as:

$$\theta(x, t) = \int_{-\infty}^{\infty} \left[ \frac{1}{2\pi} \int_{-\infty}^{\infty} f(\xi) e^{i\omega \xi} d\xi \right] e^{-i\omega x} e^{-\lambda \omega^2 t} d\omega \quad (177)$$

where  $\xi$  is used as a dummy integration variable. Now, the order of the integration can be changed over:

$$\theta(x, t) = \int_{-\infty}^{\infty} f(\xi) \left[ \frac{1}{2\pi} \int_{-\infty}^{\infty} e^{-\lambda \omega^2 t} e^{-i\omega(x-\xi)} d\omega \right] d\xi \quad (178)$$

The expression in the bracket forms the heat kernel, that has the following form (Tichonow and Samarski, 1963):

$$G(x-\xi, t) = \frac{1}{2\pi} \int_{-\infty}^{\infty} e^{-k\omega^2 t} e^{-i\omega(x-\xi)} d\omega = \frac{1}{\sqrt{4\pi k t}} e^{-\frac{(x-\xi)^2}{4\lambda t}} \quad (179)$$

Therefore, Eq. (178) can be rewritten as:

$$\theta(x,t) = \int_{-\infty}^{\infty} f(\xi)G(x-\xi,t)d\xi \quad (180)$$

Eq. (180) represents spatial convolution of the functions  $f(\xi)$  and  $G(x-\xi,t)$ . Let consider special case, when the initial temperature distribution  $f(\xi)$  is concentrated at a point  $x_0$ , namely:

$$f(\xi) = A\delta(\xi - x_0) \quad (181)$$

Where  $\delta$  denotes the Dirac function. This implies, that the intensity of the heat source at time  $t = 0$  in an infinite rod reads:

$$Q = c_v \rho \int_{-\infty}^{\infty} f(\xi) d\xi = c_v \rho \int_{-\infty}^{\infty} A \delta(\xi - x_0) dx = c_v \rho A \quad (182)$$

For  $t > 0$ , the temperature function  $\theta(x,t)$  is given by:

$$\theta(x,t) = \int_{-\infty}^{\infty} f(\xi)G(x-\xi,t)d\xi = \int_{-\infty}^{\infty} A \delta(\xi - x_0)G(x-\xi,t)d\xi = AG(x-x_0,t) \quad (183)$$

where the fact, that the only contribution to the integral comes from the point at which the argument of the delta Dirac function is zero ( $x_0$ ), has been used. Thus, one obtains:

$$\theta(x,t) = AG(x-x_0,t) = \frac{Q}{c_v \rho \sqrt{4\pi k t}} e^{-\frac{(x-x_0)^2}{4\lambda t}} \quad (184)$$

The total area under this distribution is equal to  $A$  for any time  $t$ . The convolution in Eq. (180) represents a weighted average of the function  $f(\xi)$  about the point  $x_0$  (Eq. (181)).

As already stated, during the kinematically controlled tensile test, the “travelling” slip band generates abruptly some amount of heat (during serration), recorded by the thermometer in the form of the temperature spikes (Fig. 48). The temperature distribution in the range without phase transformation (region 1, Fig. 48) has regular form. The slip band propagates smoothly from one extremity of the specimen to the other (Fig. 49).

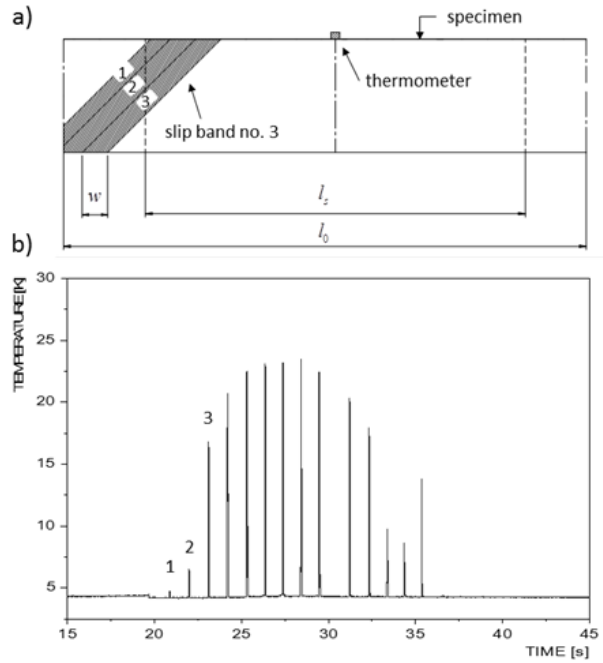


Fig. 49 Thermodynamic aspect of DPF (region 1) in 304 stainless steel: a) slip band propagates along gauge length  $l_0$  ( $l_s$  is the measurement range of the thermometer, and  $w$  is the width of the slip band);  
b) time response of the thermometer

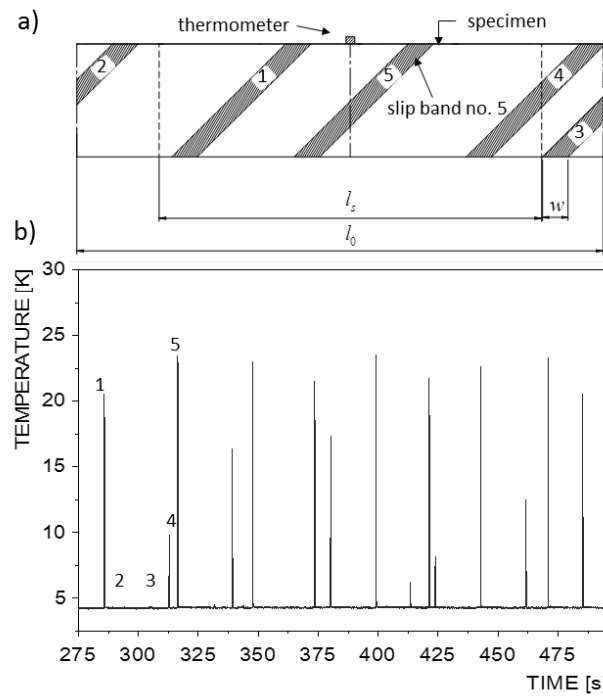


Fig. 50 Thermodynamic aspect of DPF coupled with the phase transformation (region 3) in 304 stainless steel:  
a) the slip band propagates along the gauge length in a random way; b) time response of the thermometer

After exceeding the plastic strain threshold, the hardening effect is observed (region 3, Fig. 48). The martensitic phase starts gradually to appear in the material. New phase significantly affects sequential spreading (“travelling”) of slip band during the test. As already stated, the intersecting shear systems in a slip band can be very effective nucleation sites of the martensitic phase. It is believed, that the slip band is pinned by the martensitic phase. Then, the place where a new slip band will be observed depends on the material imperfections. A scheme of the process is presented in Fig. 50.

To sum up, the strain localisation effect is reflected by the temperature distribution during the tensile test of stainless steel specimen at LHe temperature. Based on the thermodynamic analysis, a numerical simulation of the temperature evolution can be carried out. The results of the analysis are presented in Chapter 6.

## Chapter 6

# Numerical model

Based on the general constitutive description of the strain induced phenomena: DPF and  $\gamma-\alpha'$  phase transformation, and the strain localisation effect (reflected by the Green-like solution of heat diffusion equation), one-dimensional numerical response of 304 austenitic stainless steel during a kinematically controlled tensile test at 4.2 K is presented and discussed. General assumptions for the constitutive model of DPF coexisting with the phase transformation, and for the thermodynamic model of strain localisation, were formulated in Chapter 5.

### 6.1. Computational aspects of DPF coexisting with phase transformation

With regard to the numerical aspects of one-dimensional model of DPF coexisting with phase transformation, the following extra assumptions are adopted:

- The explicit incremental scheme (Forward Euler method) is applied for the stress integration, controlled with a constant value of the total strain increment  $\Delta\varepsilon_0$ . Thus, the evolution of the stress has the following general form:

$$\sigma_{k+1} = \sigma_k + F(\sigma_k, \varepsilon_k) \Delta\varepsilon_0 \quad (185)$$

where, the increment of strain  $\Delta\varepsilon_0$  is defined as:

$$\Delta\varepsilon_0 = \frac{\varepsilon_{\max}}{N} \quad (186)$$

where  $N$  denotes the number of the iteration steps. The maximum value of strain  $\varepsilon_{\max}$  is identified based on the experimental stress strain curve.

- The response of stress during the kinematically controlled uniaxial tensile test is defined in terms of four stages within each serration cycle: elastic loading (1), smooth plastic flow

(2), abrupt drop of stress (3) and stress relaxation (4) (cf. Fig. 32, Section 5.1.1; Skoczeń et al., 2010).

- It is assumed, that the increase of the plastic strain due to stage 3, (fast slip) is caused by a different mechanism than in the regular continuous yielding within stage 2 (motion of dislocations), (see Fig. 51a, b), (Skoczeń et al., 2014; Tabin et al., 2015). Distribution of the increment of plastic strain within single serration is presented in Fig. 51c.

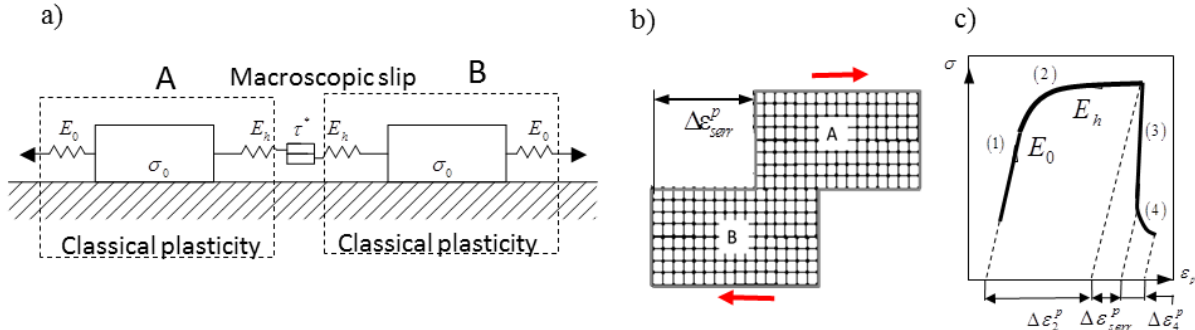


Fig. 51 a) Illustration of different mechanisms of plastic deformation during DPF (Skoczeń et al., 2010, 2014); b) the amount of slip  $\Delta \varepsilon_{serr}^p$  during the process of catastrophic failure of lattice barriers; c) breakdown of plastic strain within one serration

- Following the experimental results, it is assumed that the abrupt drop of stress (stage 3) occurs at a constant value of total strain ( $\varepsilon_{k+1} = \varepsilon_k$ ). Hence, redistribution of the elastic and the plastic parts of strain takes place in stage 3.

$$|\varepsilon_{serr}^p| = |\varepsilon_{serr}^s| \quad (187)$$

- The plastic strain threshold  $\varepsilon_{LC}^p$  for the initiation of each serration gradually increases.
- The return mapping algorithm is used as soon as the hardening curve is reached. Thus, for stage 1:

$$\begin{aligned} \text{if } \sigma_k > \sigma_p \text{ then} \\ \sigma_{k+1} &= \sigma_p \\ \varepsilon_{k+1} &= \varepsilon_k + \frac{\sigma_p - \sigma_k}{E_0} \end{aligned} \quad (188)$$

where  $\sigma_p$  denotes the current yield point, and  $E_0$  is the elastic modulus.

- Drop of stress is followed by the temperature rise, that indicates that DPF has mechanical origin.

- During the DPF the dissipated plastic power is converted to heat, which is partly used to warm up the sample, and partly exchanged by convection between the specimen and the surrounding cryogen (liquid helium).
- The stress relaxation is described by phenomenological Eq. (218) (cf. Zaiser and Hähner, 1997; Skoczeń et al., 2010; Skoczeń et al., 2014; Tabin et al., 2017). However, it correctly reflects the thermally affected stress relaxation.

The general concept of the forward Euler scheme is presented below. It is worth pointing out, that this method, sometimes called “explicit Euler”, is perhaps the simplest scheme to find the approximate solution of the ordinary differential equation. Thus, the general first order differential equation can be written as:

$$\begin{aligned}\frac{dy}{dt} &= F(y, t) \\ y(0) &= y_0\end{aligned}\tag{189}$$

The initial data is given at  $t = 0$ , and positive  $t$  is considered only. Eq. (189) has smooth solution within the interval  $0 \leq t \leq T$ . First of all,  $t$  has to be discretised. To do this, the interval  $0 \leq t \leq T$  is subdivided into  $N$  equal parts:

$$\Delta t = \frac{T}{N}\tag{190}$$

To construct the approximation, at first  $t$  derivative in Eq. (189) has to be developed:

$$\frac{dy(x)}{dt} = \lim_{\Delta t \rightarrow 0} \frac{y(t + \Delta t) - y(t)}{\Delta t}\tag{191}$$

Since  $t$  has been discretized, no information about the solution less than  $\Delta t$  can be found. This means replacing the derivative with:

$$\frac{dy(t)}{dt} \approx \frac{y(t + \Delta t) - y(t)}{\Delta t}\tag{192}$$

The Forward Euler scheme is as follows:

$$\begin{aligned}y_0 &= y_0 \\ y_1 &= y_0 + F(t_0, y_0) \Delta t \\ &\dots \\ y_{k+1} &= y_k + F(t_k, y_k) \Delta t\end{aligned}\tag{193}$$

The above presented scheme is adapted to the model of DPF coexisting with phase transformation.

The integration starts with the initial conditions:

$$\begin{aligned}
 \varepsilon_k &= 0 && \text{initial strain} \\
 \sigma_k &= 0 && \text{initial stress} \\
 B_k &= B_0 && \text{initial value of number of dislocation pile-ups at the} \\
 &&& \text{lattice barriers} \\
 \rho_k &= \rho_0 && \text{initial dislocations density} \\
 \xi_k &= 0 && \text{initial volume fraction of } \alpha' \text{ phase} \\
 \sigma_p &= \sigma_0 && \text{initial value of the yield stress} \\
 E_0 &&& \text{elastic modulus} \\
 (E_h)_k &= E_{h0} && \text{initial hardening modulus} \\
 \varepsilon_{LC}^p &= (\varepsilon_{LC}^p)_0 && \text{initial plastic strain threshold for the evolution of} \\
 &&& \text{lattice barriers} \\
 (\varepsilon^p)_k &= 0 && \text{initial plastic strain} \\
 (\varepsilon_\xi^p)_k &= (\varepsilon_\xi^p)_0 && \text{initial plastic strain threshold for the evolution of} \\
 &&& \alpha' \text{ phase}
 \end{aligned} \tag{194}$$

The first part of deformation involves the elastic regime (stage 1). As long as the stress remains below the yield point  $\sigma_p$ , the stress and the strain are calculated as follows:

$$\varepsilon_{k+1} = \varepsilon_k + \Delta\varepsilon \tag{195}$$

$$\sigma_{k+1} = \sigma_k + E_0 \Delta\varepsilon \tag{196}$$

The plastic deformation (stage 2) starts when the stress exceeds the yield point  $\sigma_p$ . As long as the  $\alpha'$  embryos do not occur, linear strain hardening is assumed:

$$\sigma_{k+1} = \sigma_k + E_{h0} \Delta\varepsilon \tag{197}$$

The plastic strain during stage 2 is defined as:

$$\varepsilon_{k+1}^p = \varepsilon_k^p + \Delta\varepsilon^p \quad \text{where} \quad \Delta\varepsilon^p = \Delta\varepsilon \left( 1 - \frac{E_{h0}}{E_0} \right) \tag{198}$$

where,  $E_{h0}$  is the initial hardening modulus of pure austenite. Then, the threshold for the evolution of  $\alpha'$  fraction is tested. As soon as the initial strain threshold  $\varepsilon_{\xi}^p$  is exceeded, the evolution of the martensite fraction  $\xi$  follows the formula:

$$\text{if } \varepsilon_{k+1}^p > (\varepsilon_{\xi}^p)_{k+1} \text{ then } \xi_{k+1} = \xi_k + \Delta\xi \quad (199)$$

where

$$\Delta\xi = A\Delta\varepsilon_{k+1}^p \quad (200)$$

Here,  $A$  denotes the intensity parameter of the martensitic transformation (Garion and Skoczen, 2002; Garion, 2003; Garion and Skoczen, 2003). This parameter is determined experimentally (Garion, Skoczeń and Sgobba, 2006).

During the phase transformation the strain hardening modulus is updated according to the formula (Eq. (162), Section: 5.2.6):

$$E_h = E_{h0} \cdot (1 + h \cdot \xi_k) + \frac{\left(5 \cdot E_0 \cdot \eta \cdot \frac{\xi_k}{3 \cdot (1 + \eta)}\right)}{\left(\frac{3}{1 + \nu} \cdot (1 + \eta) + 3 \cdot \eta\right)} - \xi_k \quad (201)$$

where  $h$  is an experimentally defined material parameter, reflecting interactions between the dislocations and the martensitic phase,  $\eta$  is the relation between the hardening modulus  $E_{h\xi}$ , related to the Orowan mechanism, and the elastic modulus  $E_0$  of pure austenite:

$$\eta = \frac{E_{h\xi}}{E_0}; \text{ where } E_{h\xi} = E_{h0} (1 + h \cdot \xi_k) \quad (202)$$

Hence, the stress is updated according to the formula:

$$\sigma_{k+1} = \sigma_k + E_h \Delta\varepsilon = \sigma_k + \left( E_{h0} \cdot (1 + h \cdot \xi_k) + \frac{\left(5 \cdot E_0 \cdot \eta \cdot \frac{\xi_k}{3 \cdot (1 + \eta)}\right)}{\left(\frac{3}{1 + \nu} \cdot (1 + \eta) + 3 \cdot \eta\right)} - \xi_k \right) \Delta\varepsilon \quad (203)$$

and the plastic strain is calculated according to the following formula:

$$\varepsilon_{k+1}^p = \varepsilon_k^p + \Delta\varepsilon^p \quad \text{where} \quad \Delta\varepsilon^p = \Delta\varepsilon \left( 1 - \frac{E_h}{E_0} \right) \quad (204)$$

Also, the yield stress value is updated.

Another threshold is checked with respect to the evolution of the number of pile-ups of dislocations at the lattice barriers. Thus, when  $\varepsilon^p > \varepsilon_{LC}^p$  a new value of  $B$  is calculated according to Eq. (12), (Section 5.1.1):

$$\text{if } \varepsilon_{k+1}^p > \varepsilon_{LC} \text{ then } B_{k+1} = \min(B_k + F_{LC}^+ \Delta\varepsilon_{k+1}^p; B_{cr}) \quad (205)$$

where  $B_{cr}$  is the critical value, beyond which the serration occurs immediately (Eq. (38), Fig. 35, Section 5.1.1), and  $F_{LC}^+$  is a function expressed in the following way:

$$F_{LC}^+ = k_4 \sqrt{\rho_k} \quad (206)$$

where  $k_4$  denotes a constant. Moreover, during this stage, the state parameters change. The updated value of dislocations density  $\rho$  reads:

$$\rho_{k+1} = \rho_k + \Delta\rho \quad (207)$$

where the creation and the annihilation terms are introduced in the definition of  $\Delta\rho$  (Mecking and Kocks, 1981; Bouquerel et al., 2006; Skoczeń et al., 2010; Skoczeń et al., 2014):

$$\Delta\rho = \Delta\varepsilon^p M \left( \frac{1}{db} + k_1 \frac{\sqrt{\rho_k}}{b} + \frac{k_2}{b} \sqrt{B_k} - k_a \rho_k \right) \quad (208)$$

Here,  $M$  is the Taylor factor,  $d$  stands for the average grain size,  $b$  denotes the Burgers vector,  $B$  is the density of lattice barriers,  $k_1, k_2$  are constants,  $k_a$  represents the dislocation annihilation constant. The corresponding average shear stress in the lattice  $\tau$  (Bouquerel et al., 2006) has the following form:

$$\tau = \tau_0 + \alpha \mu b \sqrt{\rho_{k+1}} \quad (209)$$

where  $\mu$  is the shear modulus,  $\alpha$  is the coefficient of dislocations interaction, and  $\tau_0$  denotes the intrinsic lattice strength. The mean free path of dislocation  $\bar{\lambda}$  is expressed by (Skoczeń et al., 2010, 2014):

$$\bar{\lambda} = \left( \frac{1}{d} + k_1 \sqrt{\rho_{k+1}} + k_2 \sqrt{B_{k+1}} \right)^{-1} \quad (210)$$

The shear stress at the head of dislocation pile-up  $\tau_e$  is determined with the use of relations:

$$\tau_e = \frac{\pi(1-\nu)}{\mu b} \bar{\lambda} \tau^2 \quad (211)$$

where  $\nu$  denotes the Poisson ratio. Finally, the serration criterion is tested (Eq. (38), Fig. 35, Section 5.1.1). If the combination of the density of dislocation pile-ups at lattice barriers  $B$ , and the average shear stress at the head of dislocation pile-up  $\tau_e$  do not reach the interaction curve (Fig. 35, Section 5.1.1), the stress is calculated based on Eq. (191) or Eq. (203), and the continuous plastic flow occurs. If not, stage 3 occurs, and the avalanche-like process is triggered. The majority of lattice barriers are broken, resulting in the abrupt drop of stress. It is assumed that the relation between the stress in the lattice and the density of dislocations exists (Eqs (30) and (34), Section 5.1.1) and is defined as:

$$\sigma_{k+1} = M \left( \tau_0 + \alpha \mu b \sqrt{\rho_{k+1}} \right) \quad (212)$$

Therefore, the drop of stress during stage 3 can be described as the difference in stress before and after serration (Tabin et al., 2016):

$$\Delta \sigma^{serr} = \sigma_k^{before} - \sigma_k^{after} = M \mu \alpha b \left( \sqrt{\rho_k} - \sqrt{\rho_k^{serr}} \right) \quad (213)$$

where  $\rho_k^{serr}$  is the after-serration density of dislocations. It is assumed that after serration this parameter does not retain the initial value  $\rho_0$  (Eq. (194)). Moreover, the  $\rho_k^{serr}$  develops during the plastic deformation. In the presented model, this parameter is calculated based on the best-fit approximation formula:

$$\rho_k^{serr} = \left( \frac{0.00095}{(\varepsilon_p)_k^{2/3}} + 0.5 \right) \rho_k \quad (214)$$

This formula is calculated based on the uniaxial tensile test results for 304ss at 4.2 K. The same approach is applied to the number of pile-ups of dislocation at the lattice barriers after serration  $B_k^{serr}$ .

It is assumed, that the serration starts at  $\sigma_k^{before}$ , takes place at a constant value of total strain  $\varepsilon^{serr}$ , and the increment of plastic strain corresponds to the equivalent decrement of the elastic strain (Fig. 36, Section 5.1.1).

Therefore, the plastic strain increment during stage 3 has the form (Fig. 51):

$$\Delta \varepsilon_p^{serr} = \frac{M \alpha b \left( \sqrt{\rho_k} - \sqrt{\rho_k^{serr}} \right)}{2(1+\nu) E_0} \quad (215)$$

It is worth pointing out, that the increase of the plastic strain due to serration  $\Delta \varepsilon_p^{serr}$  is caused by fast slip (Fig. 51). At the end of stage 3, the stress and the unchanged strain are calculated:

$$\begin{aligned} \varepsilon_{k+1} &= \varepsilon_k = \varepsilon^{serr} \\ \sigma_{k+1} &= \sigma_k - E_0 \Delta \varepsilon_p^{serr} \end{aligned} \quad (216)$$

Then, a new strain threshold for the evolution of the lattice barriers  $\varepsilon_{LC}^p$  is established:

$$\left( \varepsilon_{LC}^p \right)_{k+1} = \left( \varepsilon_{LC}^p \right)_k + \varepsilon_k^p \quad (217)$$

Finally, stage 4 is expected, where the stress develops according to the formula (Eq. (44), Section 5.1.1):

$$\sigma_{k+1} = \sigma_k + \Delta \sigma_k \quad \text{where} \quad \Delta \sigma_k = \frac{(\sigma_\infty - \sigma_{k-1} - \Delta \sigma_{k-1})}{t_\phi} \quad (218)$$

where

$$\varepsilon_{k+1} = \varepsilon_k + \Delta \varepsilon \quad (219)$$

The stress decrement takes place as long as its value is not sufficiently close to the asymptotic value  $\sigma_\infty$ , assumed to be 95% of the after serration value obtained in Eq. (216).

The plastic strain is evaluated as:

$$\varepsilon_{k+1}^p = \varepsilon_k^p + \Delta \varepsilon^p \quad \text{where} \quad \Delta \varepsilon^p = \Delta \varepsilon \left( 1 - \frac{\Delta \sigma}{\Delta \varepsilon E_0} \right) \quad (220)$$

The calculation of stress is repeated for following Eq. (218), as long as  $\sigma_{k+1} > 1.04 \sigma_\infty$ . As soon as the asymptotic level is reached, the relaxation stage is ended. If  $\varepsilon^p$  does not exceed  $\varepsilon_\xi^p$ , the yield stress is updated to:

$$\sigma_p = \frac{E_0 E_h (\varepsilon - \varepsilon^{serr}) + E_0 \sigma^{serr} - E_h \sigma}{E_0 - E_h} \quad (221)$$

where  $\varepsilon^{serr}$  denotes the total strain for the last stress serration (Eq. (216)), and  $\sigma^{serr}$  is the stress value the last serration started from. Finally, the integration scheme goes back to Eqs (186), (188), i.e. to the elastic deformation range.

## 6.2. Numerical model of strain localisation during DPF

Four-stage approach is applied also for the thermal effect. As the strain localisation is observed during DPF, it is assumed that the RVE “travels” together with the slip band (Fig. 52). It means, that the temperature is registered in the place where the slip band occurs.

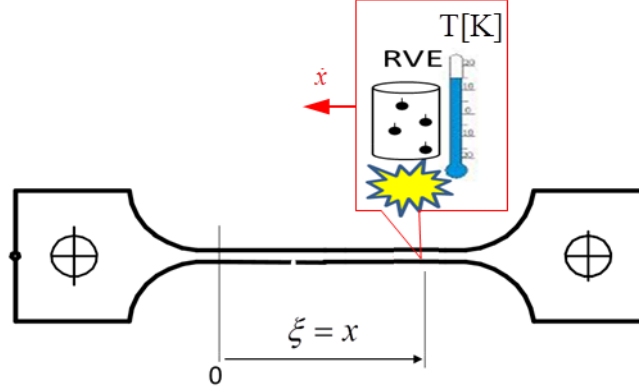


Fig. 52 The thermometer “travels” together with the slip band and the temperature is registered in the place where the slip band occurs

Furthermore, it is assumed, that there is no change of temperature as long as the elastic deformation lasts (stage 1), since there is no dissipation of energy. During the continuous plastic flow (stage 2), the dissipated plastic power is converted (with some efficiency  $\eta_T$ ) to heat (Dumoulin et al., 2010). This heat power is partly used to warm up the sample, and partly exchanged by convection between the sample and the surrounding liquid helium. The evolution of temperature is evaluated on the basis of the heat balance equation (Skoczeń et al., 2014):

$$\rho_m C_v \Delta T_{k+1} + \lambda \frac{4A}{gV} \frac{\Delta \varepsilon}{v_\varepsilon} \Delta T_{k+1} = \eta_T \sigma_{k+1} \Delta \varepsilon_{k+1}^p \quad (222)$$

where  $\rho_m$  denotes the mass density,  $C_v$  is the specific heat,  $\lambda$  denotes the thermal conductivity,  $A$ ,  $g$ ,  $V$  are the area, the thickness and the volume of the sample, respectively, and  $\frac{\Delta \varepsilon}{v_\varepsilon}$  denotes the estimated time increment, computed as the ratio of the strain increment and the strain rate. Thus, based on Eq. (222), the change of temperature  $\Delta T_{k+1}$  is calculated as:

$$\Delta T_{k+1} = \frac{\eta_T \sigma_{k+1} \Delta \varepsilon_{k+1}^p}{\rho_m C_v + \lambda \frac{4}{g^2} \frac{\Delta \varepsilon}{v_\varepsilon}} \quad (223)$$

and represents an increase of temperature during stage 2. Stage 3 (serration) takes place within an extremely short time (micro-seconds). It is assumed, that this stage is nearly adiabatic. Therefore, the total plastic power corresponding to this stage is converted to heat, and used for temperature increase. The heat balance equation has the form:

$$\rho_m C_v \Delta T_{k+1} = \eta_T \sigma_{k+1} \Delta \varepsilon_{k+1}^p \quad (224)$$

Moreover, the increment of temperature can be calculated:

$$\Delta T_{k+1} = \frac{\eta_T \sigma_{k+1} \Delta \varepsilon_{k+1}^p}{\rho_m C_v} \quad (225)$$

This describes temperature peak experimentally observed, because of reduced value of the denominator. During stage 4 (relaxation), there is no heat source, and the sample is cooled down to the liquid helium temperature (4.2 K). Hence:

$$\rho_m C_v \Delta T_{k+1}' + \frac{4\lambda}{g^2} \frac{\Delta \varepsilon}{v_\varepsilon} (T_{k+1} - T_0) = 0 \quad (226)$$

and the temperature decrement is calculated as long as the term in the parenthesis is greater than zero, i.e. thermal equilibrium is achieved:

$$\Delta T_{k+1} = -\frac{4\lambda}{\rho_m C_v g^2} \frac{\Delta \varepsilon}{v_\varepsilon} (T_{k+1} - T_0) \quad (227)$$

The specific heat  $C_v$ , and the thermal conductivity  $\lambda$ , are functions of temperature (after Marquardt et al. 2000) as shown in Fig. 53 for 304 stainless steel. In addition, these parameters of 304ss are compared with the thermal parameters of fibreglass epoxy, the material very often used in cryogenic temperatures.

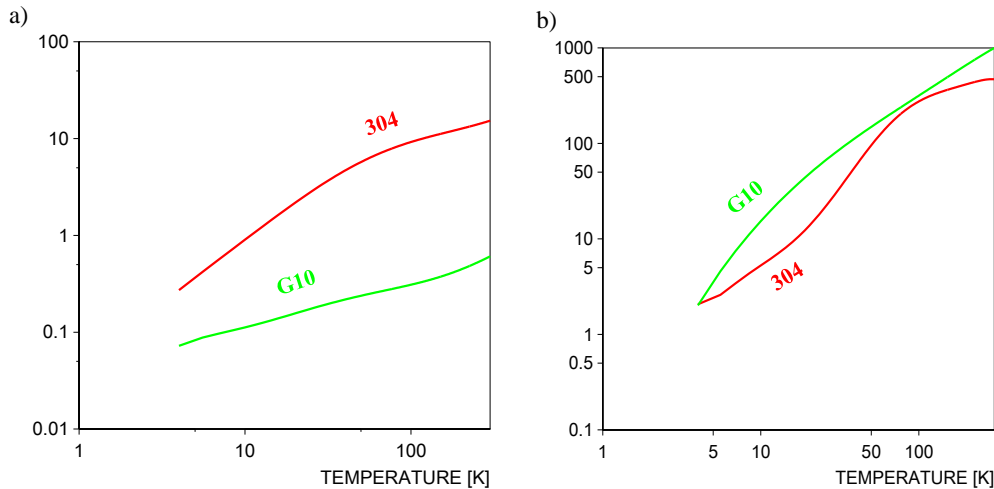


Fig. 53 Thermal conductivity and specific heat of 304 stainless steel and G-10 fibreglass epoxy, as a function of temperature (Marquardt et al., 2000)

In the case of 304 stainless steel, the available data are sufficient to give a fairly accurate estimate of  $\lambda(T)$  in the range 4.2-300 K (Marquardt et al., 2000):

$$\begin{aligned} \log \lambda = & -1.4087 - 1.3982 \log T + 0.2543 (\log T)^2 + \\ & - 0.6260 (\log T)^3 + 0.2334 (\log T)^4 + 0.4256 (\log T)^5 + \\ & - 0.4658 (\log T)^6 + 0.1650 (\log T)^7 - 0.0199 (\log T)^8 \end{aligned} \quad (228)$$

The mean heat conductivity takes the following form:

$$\bar{\lambda} = \frac{1}{(T_2 - T_1)} \int_{T_1}^{T_2} \lambda(T) dT \quad (229)$$

Similarly the specific heat is estimated in the range 4.2-300 K (Marquardt et al., 2000):

$$\begin{aligned} \log C_v = & -1.4087 - 1.3982 \log T + 0.2543 (\log T)^2 + \\ & - 0.6260 (\log T)^3 + 0.2334 (\log T)^4 + 0.4256 (\log T)^5 + \\ & - 0.4658 (\log T)^6 + 0.1650 (\log T)^7 - 0.0199 (\log T)^8 \end{aligned} \quad (230)$$

The mean specific heat has the following form:

$$\bar{C}_v = \frac{1}{(T_2 - T_1)} \int_{T_1}^{T_2} C_v(T) dT \quad (231)$$

### 6.3. Numerical results

The following set of parameters was applied in the numerical analysis:

Table 8 The parameters applied in the numerical analysis of the stress, the temperature and the dislocations density (Fig. 54-Fig. 57)

Parameter	Equation	Value
$\sigma_0$	initial yield point stress value (194)	550 MPa
$E_0$	elastic modulus (194)	$2.1 \cdot 10^5$ MPa
$E_{h0}$	Initial hardening modulus (194)	250 MPa
$\rho_0$	density of dislocations (194)	$5 \cdot 10^{12} \frac{1}{m^2}$
$B_0$	initial value of density of dislocations pile-ups at lattice barriers (194)	$5 \cdot 10^{12} \frac{1}{m^2}$
$M$	Taylor's factor (208)	3.0
$\tau_0$	internal lattice friction (209)	$\frac{\sigma_0}{M} = \frac{550}{3}$ MPa

$\mu$	shear modulus	(209)	$\frac{E_0}{2(1+\nu)} = \frac{2.1 \cdot 10^5}{2(1+0.3)} \text{MPa}$
$\alpha$	dislocations interaction factor	(209)	0.4
$b$	length of the Burgers vector	(208)	$2.58 \cdot 10^{-10} \text{ m}$
$d$	average grain size	(208)	$5 \cdot 10^{-6} \text{ m}$
$(\varepsilon_{LC}^p)_0$	initial plastic strain threshold for the evolution of the lattice barriers	(194)	0.02
$(\varepsilon_{\xi}^p)_0$	initial plastic strain threshold for the evolution of the $\alpha'$ phase	(194)	0.004
$k_1$	constant	(208)	0.25
$k_2$	constant	(208)	0.01
$k_3$	constant	(208)	0.01
$k_a$	dislocation annihilation constant	(208)	0.01
$t_{\Phi}$	time of the relaxation process	(218)	100s
$A$	intensity parameters of martensitic transformation	(200)	4.23
$h$	experimentally defined material parameter, reflecting interactions between the dislocations and martensitic phase	(201)	1.9
$T_0$	test temperature	(226)	4.2 K
$V_{\epsilon}$	strain rate	(222)	$1.8 \cdot 10^3 \frac{1}{\text{s}}$
$\rho_m$	density of tested material	(222)	$7860 \frac{\text{kg}}{\text{m}^3}$
$g$	sample thickness	(222)	$3 \cdot 10^{-3} \text{ m}$
$\eta_T$	efficiency	(222)	0.9

The results of the numerical model are presented in Fig. 54 through Fig. 57.

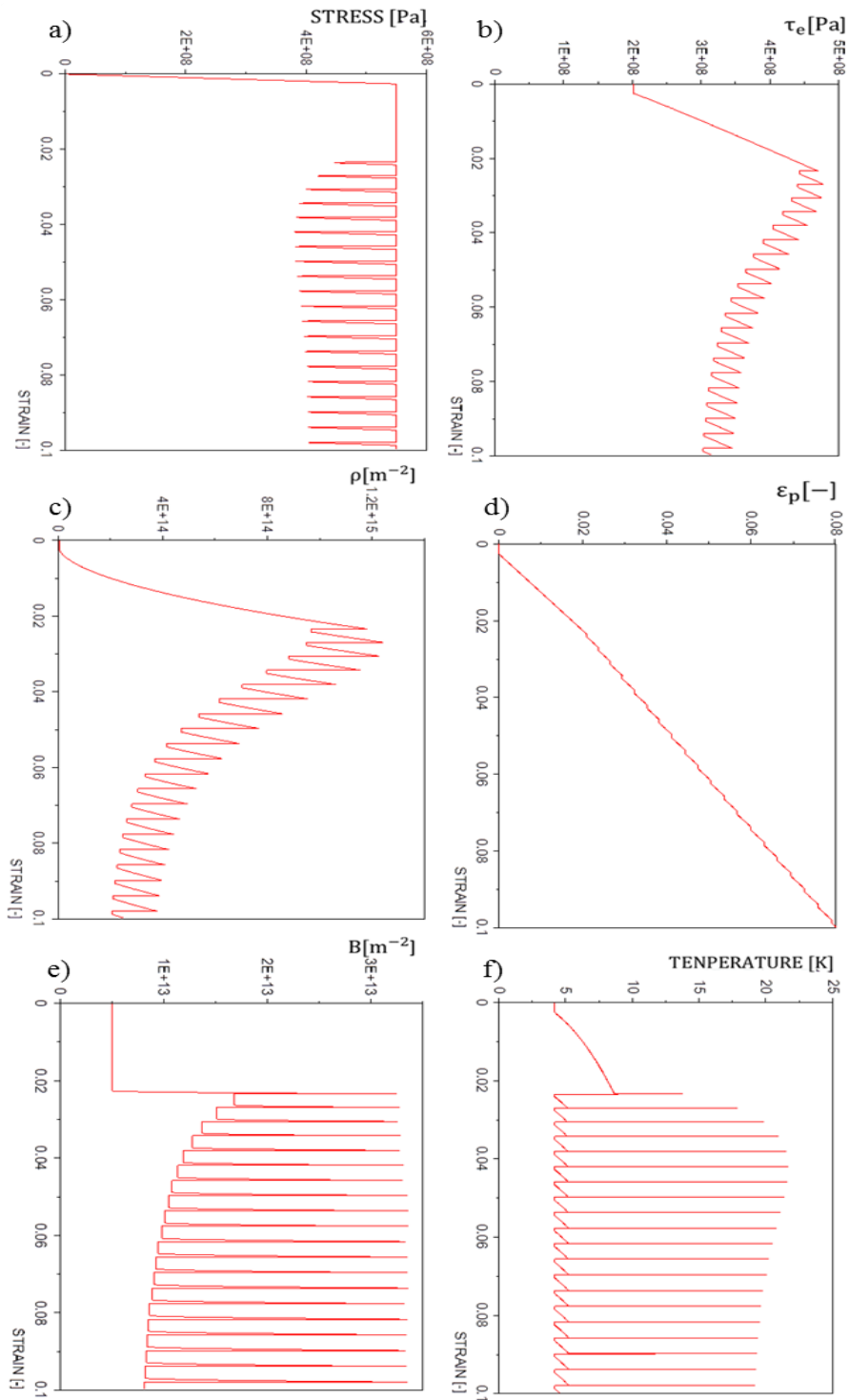


Fig. 54 The model of DPF without phase transformation- numerical results obtained for 304 stainless steel (as a function of strain): a) overall stress; b) shear stress at the head of dislocation pile-up; c) density of dislocations; d) plastic strain; e) density of dislocation pile-ups at lattice barriers; f) temperature

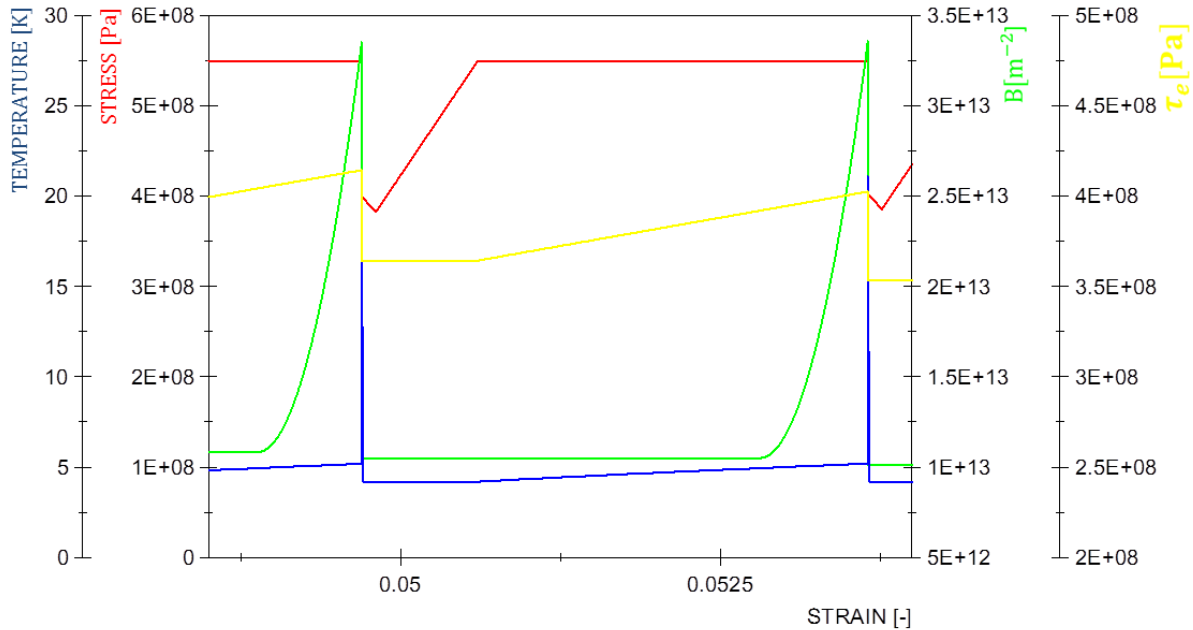


Fig. 55 DPF without phase transformation for 304 stainless steel - numerical results obtained for single serration (as a function of strain); stress (red curve); density of dislocation pile-ups at lattice barriers (green curve); shear stress at the head of dislocation pile-up (yellow curve); temperature (blue curve)

The experimental results presented in Section 4.3, indicate strong strain localisation in the form of shear bands propagating along the sample. The plastic power dissipated in the shear band is partially converted to heat, which results in drastic local increase of temperature, promoted by the so-called thermodynamic instability (nearly adiabatic process). The Dirac-like temperature function is measured by the thermometers located in the gauge length of the sample (Fig. 21). The spatio-temporal correlation indicates smooth shear band propagation, as long as the process of phase transformation remains on hold.

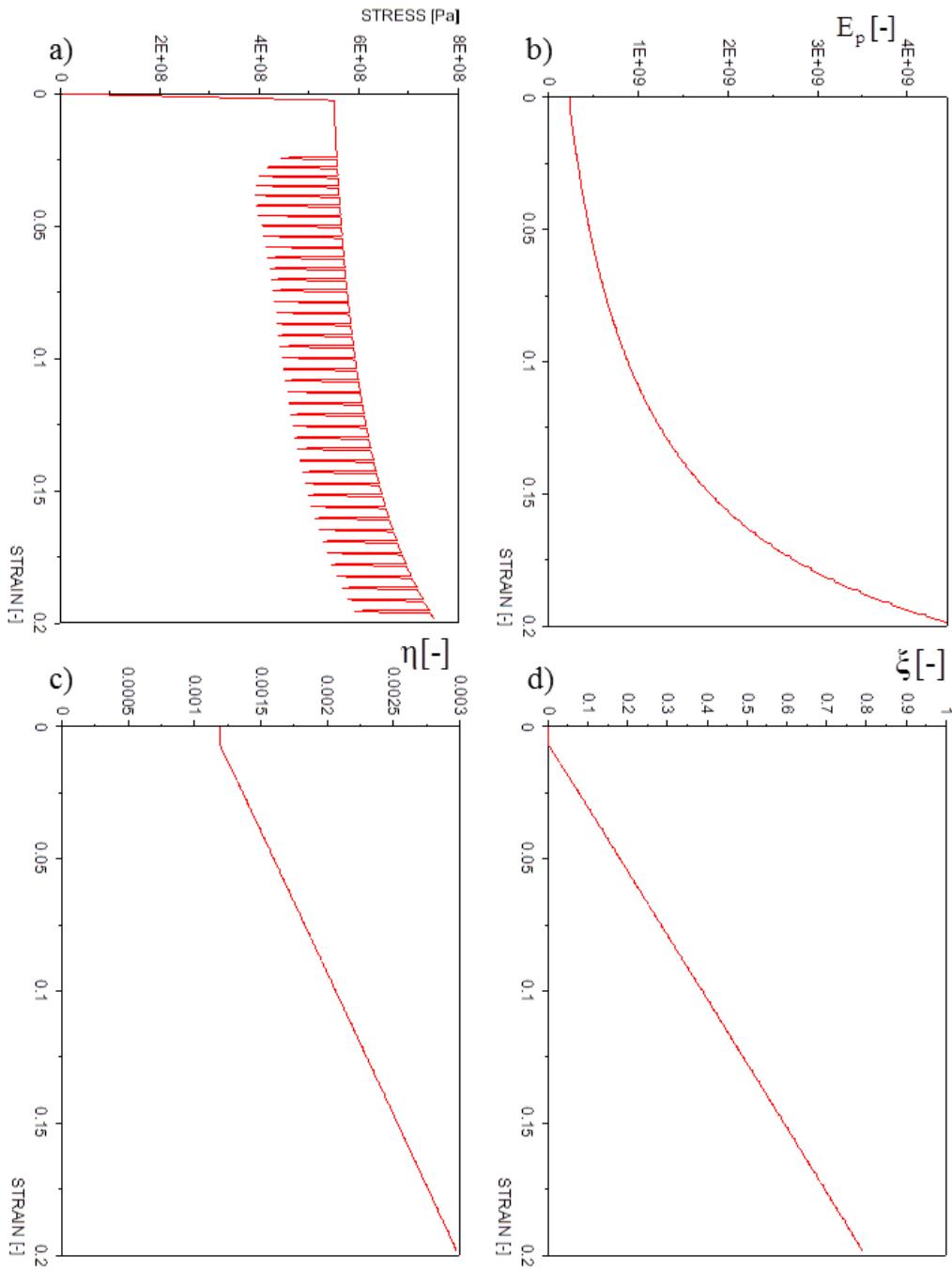


Fig. 56 DPF coexisting with phase transformation - numerical results obtained for 304 stainless steel (as a function of strain): a) stress; b) tangent modulus  $E_p$ ; c)  $\eta$  (relation between the hardening modulus  $E_{h\xi}$  and the elastic modulus  $E_0$  of pure austenite); d) volume fraction of  $\alpha'$  phase

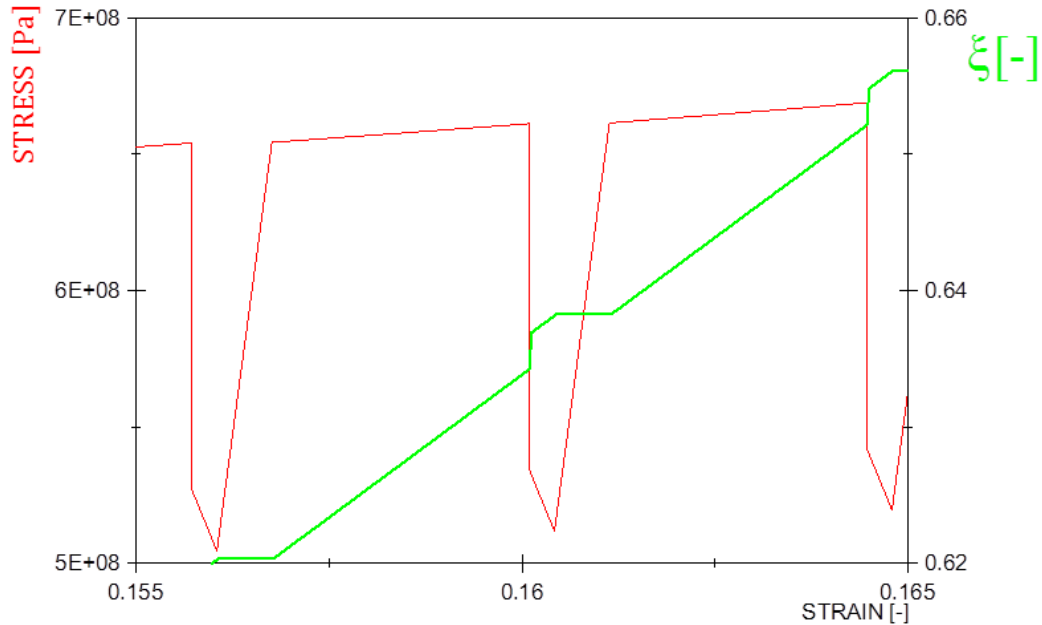


Fig. 57 DPF coexisting with phase transformation for 304 stainless steel; numerical results obtained for single serration (as a function of strain); a) stress; b) volume fraction of  $\alpha'$  phase

The difference between the numerical (Fig. 54d) and the experimental temperature distributions (Fig. 22) is related to the assumption, that in the numerical model the RVE travels together with the slip band. As regards the experiment, the thermometer is spatially oriented (mounted on the specimen surface) when the slip band propagates along the specimen (Fig. 58).

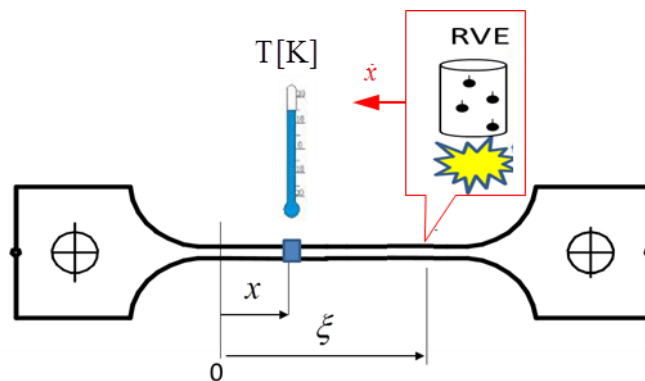


Fig. 58 Spatially oriented thermometer (attached to the sample), and “travelling” slip band (cf. Fig. 52)

In view of the foregoing, the Green-like solution of the heat diffusion equation can be used in the numerical description of the effect under consideration. For the time  $t > 0$ , the temperature function  $\theta(x, t)$  is given by (cf. Eq. (184), Section 5.3):

$$\theta(x, t_k) = \frac{Q}{c_v \cdot \rho \cdot \sqrt{4\pi\lambda t_k}} e^{-\frac{(x-x_0)^2}{4\lambda t_k}} \quad (232)$$

As the time runs, redistribution of temperature takes place and “smoothing” of the temperature distribution  $\theta(x, t)$  takes place. Fig. 59 is good illustration of the qualitative aspects of such smoothing for defined moments  $t_k$ . The physical properties of 304 stainless steel at liquid helium temperature are presented in Table 9.

Table 9 Properties of grade 304 stainless steel at liquid helium temperature and test parameters

Parameter	Equation	Value
$\lambda$ thermal conductivity	Eq. (232)	$0.23 \frac{\text{W}}{\text{m K}}$
$C_v$ specific heat	Eq. (232)	$2 \frac{\text{J}}{\text{kg K}}$
$Q$ intensity of internal heat source	Eq. (232)	$900 \frac{\text{W}}{\text{m}^3}$
$\alpha$ thermal diffusivity	-	$\frac{\lambda}{\rho_m C_v} = 0.0038 \frac{\text{m}^2}{\text{s}}$
$V_c$ cross-head velocity	-	$0.5 \frac{\text{mm}}{\text{min}}$
$V_{sb}$ slip band velocity	-	$48.5 \frac{\text{mm}}{\text{min}}$
$f_{serr}$ serration frequency	-	1 Hz

Fig. 59 shows the graph of temperature distribution that exhibits a concentration around the position  $x_0 = 0.5$ . At time  $t_k > 0$ , some of the heat has been transported from the region of the concentration to the points far away from  $x_0 = 0.5$ .

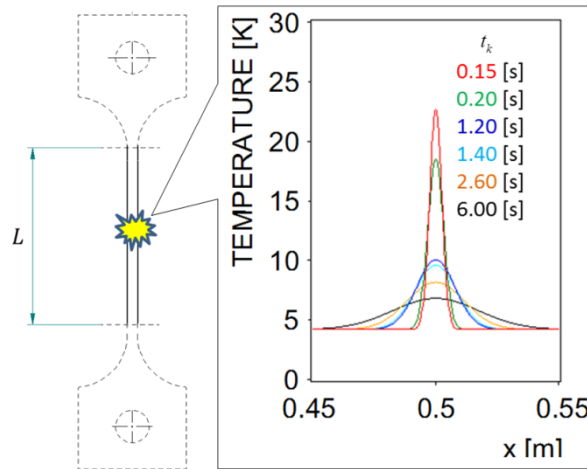


Fig. 59 Temperature distribution around the position  $x_0$  at predefined moments:

$$t_k = [0.15\text{s}, 0.20\text{s}, 1.20\text{s}, 1.40\text{s}, 2.60\text{s}, 6.00\text{s}]$$

The experimental results (time response of thermometer) indicate smooth shear band propagation, as long as the process of phase transformation remains on hold. For this range, the temperature distribution represented by Green-like solution of the heat diffusion equation (Eq.(184)) is presented in Fig. 60.

Moreover, taking into account the Green-like solution of the heat diffusion equation (Eq. (184)), the initial conditions of test, and the experimentally identified parameters (Table 9), it is possible to obtain numerically time response of the thermometer during a uniaxial tensile test at cryogenic temperatures in both ranges (Fig. 61).

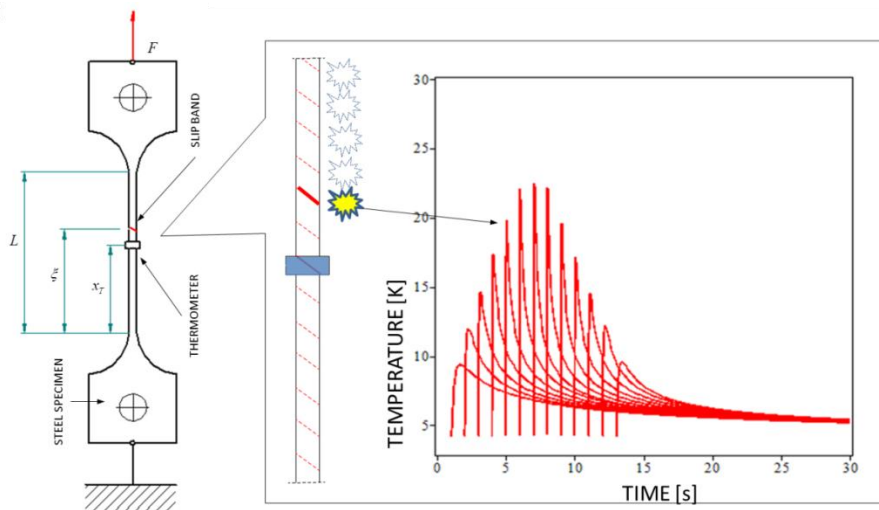


Fig. 60 Time response of “numerical thermometer”, based on the solution of heat diffusion equation

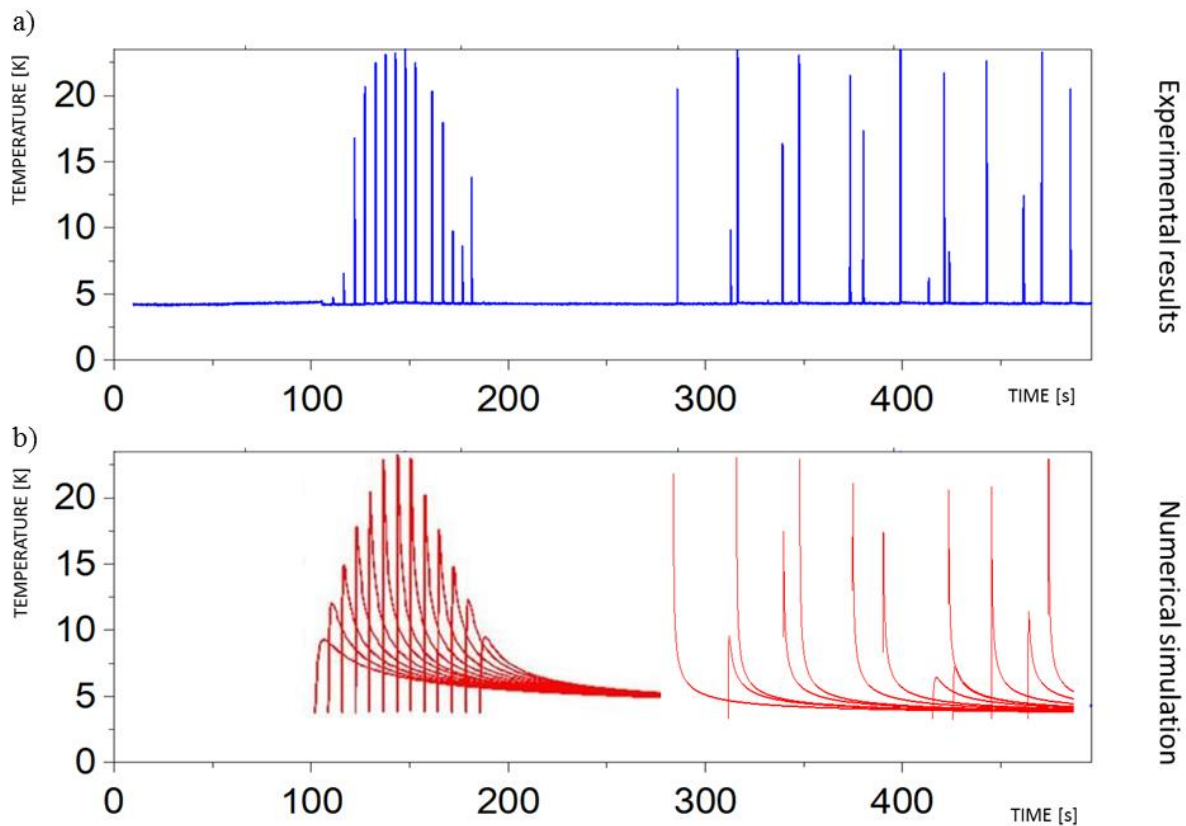


Fig. 61 a) Time response of thermometer (experimental results) during a uniaxial tensile test of 304 stainless steel at LHe temperature; b) time response of “numerical thermometer” based on the Green-like solution of the heat diffusion equation

The results of numerical analysis for the uniaxial tensile test of 304 stainless steel at 4.2 K are illustrated in Fig. 54 through Fig. 57, and Fig. 61. Good agreement with respect to the experimental data has been obtained, in particular for the strain range where the phase transformation is limited. The temperature evolution predicted by the model exhibits sudden increments and decrements, as well as the effect of “distant thermometer”.

## Chapter 7

# Discussion

Fairly limited group of engineering materials is suitable for use at extremely low temperatures. The most common materials are the fcc metals and alloys, such as copper, copper alloys, austenitic stainless steels (304 and 316 families), etc. Many of these materials undergo at cryogenics temperatures plastic flow oscillations, the so-called discontinuous plastic flow (DPF). The origin of DPF was first explained by Basinski (1957). He attributed the load drops to the thermodynamic properties of materials at very low temperatures, represented by the specific heat and the thermal conductivity tending to zero (thermodynamic instability). He assumed that any sufficiently fast dissipative process at extremely low temperatures leads to increase of local temperature (the plastic work is converted to heat) and, consequently, to rapid decrease of the flow stress. On the other hand, Seeger (1957) suggested that during the plastic deformation dislocations pile up at the lattice barriers, which cannot be overcome by thermo-activated cross slip since the temperature is very low, but by the shear force due to the stress concentration at the head of the pile-up. Obst and Nyilas (1991, 1998) pointed out, that the pile-ups of dislocations on the internal lattice barriers may give rise to stress concentrations of the order of magnitude of the theoretical shear strength. In their view, the load drops are due to a catastrophic process consisting in spontaneous generation of dislocations as soon as the internal barriers are broken. According to Seeger, and later on to Obst and Nyilas, the plastic flow instability has mechanical origin. Furthermore, Zaiser and Hähner (1997) attributed discontinuous nature of plastic flow at low temperatures to strain rate softening instabilities. They pointed out similarities between the low-temperature phenomena and the so-called Portevin–Le Chatelier (PLC) effect, that occurs at room temperature. The difference between both mechanisms consists in the fact, that in the case

of PLC the obstacles are created by diffusion, whereas, in the case of low temperature DPF they are “diffusionless”. Therefore, the PLC effect is qualified as a form of dynamic strain ageing (DSA), the diffusive mechanism, which causes that a glide dislocation segment may be subjected to an additional pinning due to the solute atoms migration towards the dislocation core.

In order to verify the origin of DPF, a unique experiment was prepared. A kinematically controlled uniaxial tensile test of steel specimen at 4.2 K was carried out. The test consisted of three stages: 1 - uniaxial tensile test with a constant speed of crosshead, 2 - halting the crosshead, 3 - continuation of the test with constant speed. The response of the force transducer after stage 2 has similar form like during the previous serration, despite the fact that the temperature of the specimen has been again reduced to the initial temperature (4.2 K). Moreover, based on the response of the temperature and the force transducers, it was shown that the abrupt drop of stress occurs first, and then the temperature increases rapidly. The mechanical approach to discontinuous plastic flow (DPF), with accompanying thermodynamic aspects is presented by Skoczeń et al. (2010, 2014), and Tabin et al. (2016, 2017).

Many of the fcc materials undergo other strain induced phenomena at cryogenics temperatures, namely: the plastic strain induced phase transformation, as well as the evolution of micro-damage. Each of these phenomena has been intensively studied (Garion and Skoczen, 2002; Garion and Skoczen, 2003; Skoczeń, 2004; Garion et al., 2006; Skoczeń, 2008; Sitko et al., 2010; Skoczeń et al., 2014; Egner et al., 2015; Ortwein et al., 2016). Nevertheless, the strain localisation effect during coexistence of the strain induced phase transformation and the DPF is a new approach, which has not been presented in the literature until now.

It is experimentally confirmed, that during the plastic deformation at higher temperatures, the intersections of shear bands can be very effective plastic strain induced nucleation sites of the martensitic embryos (Venables, 1964; Mangonon and Thomas, 1970; Suzuki et al., 1977; Brooks et al., 1979a; Fujita and Katayama, 1992; Roth et al., 2010). It appears, that the growth of the martensite occurs through the continuous nucleation and coalescence of  $\alpha'$  martensitic embryos during plastic deformation. In the light of experiments it is quite obvious, that a “travelling” slip band is pinned by martensitic embryos during the plastic deformation at cryogenic temperatures. It is worth pointing out, that the slip band propagation (the strain localisation effect) is reflected by temperature distribution during the tensile tests of steel specimens at LHe temperature (4.2 K). “Travelling” slip band generates during each serration some amount of heat, recorded by the

thermometer in the form of temperature spikes. Temperature distribution in the range without phase transformation has a regular form. It means, that the slip band propagates from one extremity of the specimen to the other, and from serration to serration. On the other hand, the temperature distribution in the form of spikes within the hardening range is random. Thus, the slip band is pinned by the martensitic phase. The place where a new slip band will be observed depends mostly on the materials imperfections.

A physically based constitutive model, presented in the Thesis, describes DPF coexisting with phase transformation. The main idea is based on the assumption, that the evolution of new martensitic phase in the austenite affects the strain hardening modulus during each serration. Furthermore, the strain localisation reflected by the temperature distribution is implemented. The experimentally measured profile of temperature spikes has been explained by building a model of “travelling” slip band, carrying the RVE, and a fixed thermometer located in the middle of the sample. Thus, based on the Green-like solution and the initial conditions of the test, as well as the experimentally identified test parameters, it is possible to obtain numerically time response of the thermometer during the uniaxial tensile test at liquid helium temperature (4.2 K). A comparison of the experimental stress-strain curve and the time response of the thermometer with the numerical results, indicates correct behaviour of the constitutive model of DPF including the effect of phase transformation, and the thermodynamic model of “travelling“ slip bands, in austenitic stainless steels. Nevertheless, the further work will be undertaken to describe complete coupling between plastic strain induced transformation and DPF in the fcc materials.

Another important and fundamental question, raised in the present Thesis, is the multi-axial feature of DPF. The initial tests were carried out successfully. The tubular specimens made of 304 stainless steel have been immersed in liquid helium (4.2 K) and subjected to kinematically controlled combined loads (Fig. 62), consisting of torsion ( $\omega = 0.058 \text{ RPM}$ ) and traction ( $V_T = 0.1 \text{ cm/min}$ ). The results of the test are presented in Fig. 63.

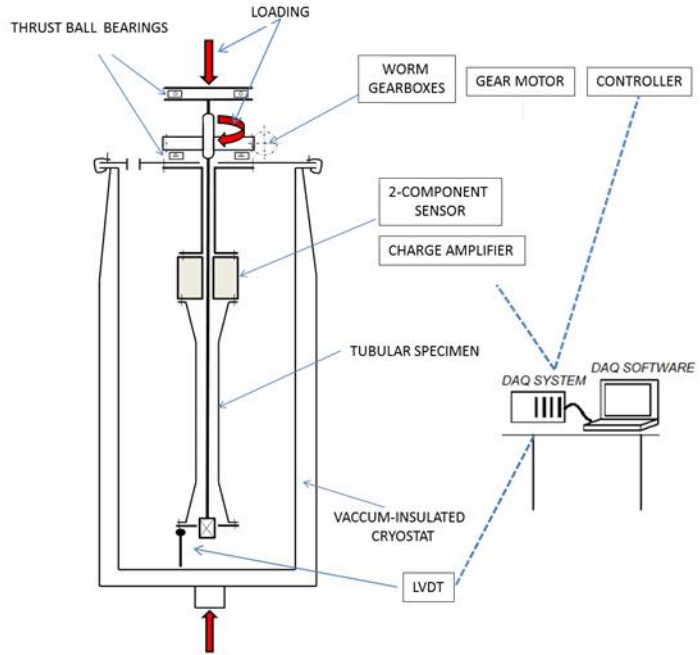


Fig. 62 Experimental set-up for combined loading

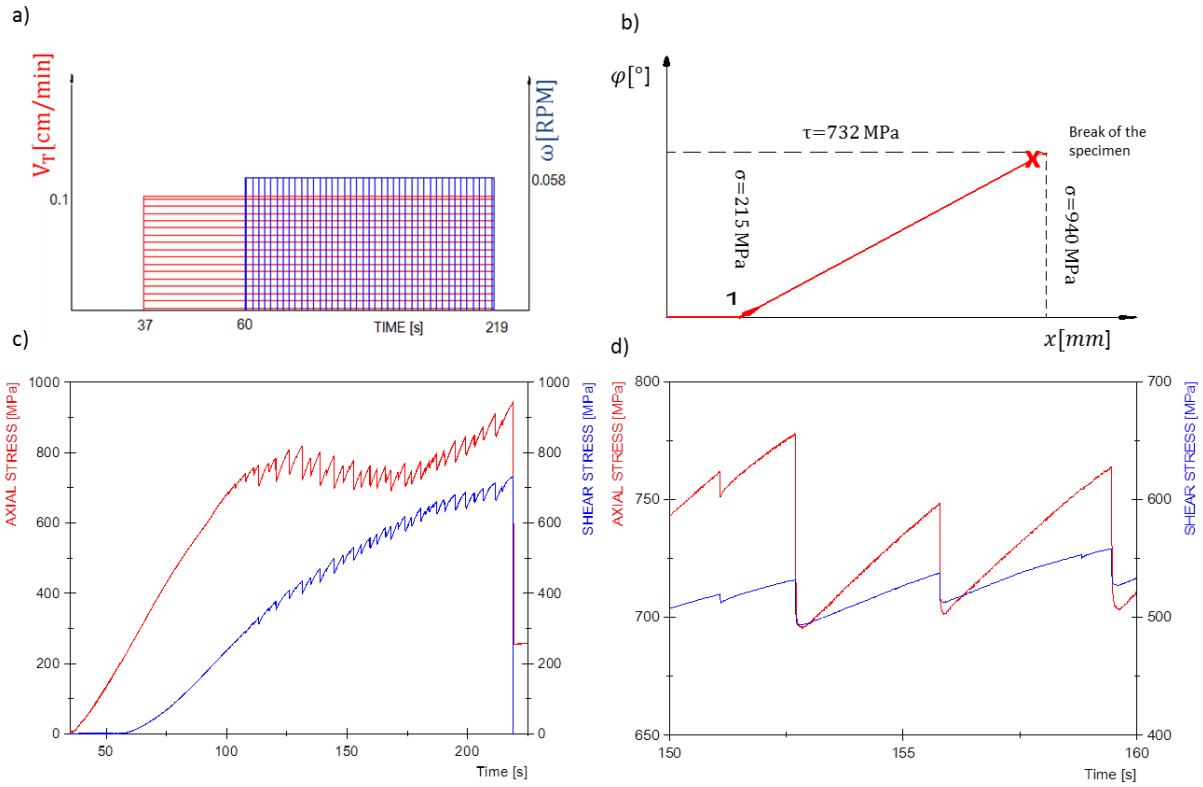


Fig. 63 DPF in the multiaxial regime: a) kinematically controlled combined loads; b) loading path; c); d) test results: combined torsion (red curve) and traction (blue curve) for 304ss

## Chapter 8

# Conclusion

The available studies of the plastic flow instability at extremely low temperatures were greatly insufficient from the experimental and the numerical point of view. Experimental identification of the strain localisation phenomenon during discontinuous plastic flow (DPF) at temperatures near 0 K has been carried out. It reveals an interesting feature of the plastic flow discontinuities, consisting in strong localisation in the form of slip bands “travelling” along the gauge length of the sample. Moreover, the phase transformation observed during DPF makes the nucleation of the slip bands, and their free glide, randomly redistributed over the gauge length of the specimen. Propagation of the slip bands is reflected by the Dirac-like temperature redistribution, recorded during the uniaxial tensile test. The measured profile of temperature spikes has been explained by building a model of “travelling” slip band, carrying the RVE, and a fixed thermometer located in the middle of the sample. A thermodynamic problem of heat diffusion in the sample has been solved, taking into account “travelling” source of a given heat generation rate. Numerically obtained profile of temperature spikes is similar to the profile measured during the experiment. Moreover, the physically based model of the phase transformation affected DPF allows to reproduce the serrations in the course of plastic deformation. It is crucial for its application in the design of components dedicated to extremely low temperatures. A typical example can be found in the domain of superconducting magnets. For instance, in the LHC (Large Hadron Collider, CERN), the magnets are separated by the so-called interconnections, containing the bellows expansion joints. Their principal function is to compensate for the thermal expansion/contraction of main components of the cryogenic system. Nevertheless, the plastic deformation may occur, hence, the DPF and the strain localisation

effect, reflected by the temperature distribution. It is worth pointing out, that inside the superconducting magnetic channels equipped with bellows, the protons are accelerated. The service temperature of the superconducting coils is equal to 1.9 K. Each heat dissipation process under such conditions can generate unexpected quench. It refers to the sudden loss of superconductivity. In the superconducting state, the resistance of the magnet coil windings tends to zero. Thus the current flow is lossless. If the temperature of superconductor exceeds a critical value, finite resistance is developed in the windings and hundreds of amperes of current pass through the coil and generate heat. This heat causes sudden boiling of liquid helium, and leads to catastrophic consequences. Such a disastrous effect occurred on 19 September 2008, during powering tests of the main dipole circuit in the LHC (CERN). A fault occurred in the electrical bus connection in the region between a dipole and a quadrupole, resulting in mechanical damage and release of six tonnes of liquid helium from the magnet cold mass into the tunnel. The escaping vapour expanded with explosive force, damaging superconducting magnets and their supports, and contaminating the vacuum pipe, which also lost vacuum conditions<sup>7</sup>.

The dissipative effect related to DPF is also observed in the superconducting materials, that consist of a copper matrix and filaments (e.g. Cu/NbTi, Cu/Nb<sub>3</sub>Sn, etc.). The DPF is observed independently in the matrix (e.g. copper alloys), and in the filaments (e.g. NbTi).

Experiments and constitutive description proposed in the Thesis, allow to better understand the strain localisation effect during DPF, affected by the phase transformation. The constitutive model and the numerical model of the phase transformation affected DPF, as well as the thermodynamic model of “travelling” slip bands will have an influence on the design process of the superconducting magnets for particle accelerators, the nuclear magnetic resonance spectrometers, the superconducting magnetic energy storage, the thermonuclear reactors, or the superconducting power lines.

---

<sup>7</sup><https://press.cern/press-releases/2008/10/cern-releases-analysis-lhc-incident>

# Bibliography

- Ahmet, Y., 2011. The Portevin–Le Chatelier effect: a review of experimental findings. *Science and Technology of Advanced Materials* 12, 063001.
- Ait-Amokhtar, H., Vacher, P., Boudrahem, S., 2006. Kinematics fields and spatial activity of Portevin–Le Chatelier bands using the digital image correlation method. *Acta Materialia* 54, 4365-4371.
- Basinski, Z.S., 1957. The instability of plastic flow of metals at very low temperatures. *Proceedings of the Royal Society of London Series A* 240, 229–242.
- Bayerlein, M., Mughrabi, H., Kesten, M., Meier, B., 1992. Improvement of the strength of a metastable austenitic stainless steel by cyclic deformation-induced martensitic transformation at 103 K. *Materials Science and Engineering: A* 159, 35-41.
- Bolling, G.F., Richman, R.H., 1970. The plastic deformation-transformation of paramagnetic f.c.c. FeNiC alloys. *Acta Metallurgica* 18, 673-681.
- Bouquerel, J., Verbeken, K., De Cooman, B.C., 2006. Microstructure-based model for the static mechanical behaviour of multiphase steels. *Acta Materialia* 54, 1443-1456.
- Boxall, T.D., Hundy, B.B., 1955. Photographing stretcher-strain markings with the Vickers projection. *Metallurgia* 51, 52-54.
- Brooks, J.W., Loretto, M.H., Smallman, R.E., 1979a. Direct Observations Of Martensite Nuclei In Stainless-Steel. *Acta Metallurgica* 27, 1839-1847.
- Brooks, J.W., Loretto, M.H., Smallman, R.E., 1979b. Insitu Observations Of The Formation Of Martensite In Stainless-Steel. *Acta Metallurgica* 27, 1829-1838.
- Bross, S., Hähner, P., Steck, E.A., 2003. Mesoscopic simulations of dislocation motion in dynamic strain ageing alloys. *Computational Materials Science* 26, 46-55.
- Bućko, S., Jodłowski, H., Trzebicki, M., 2014. An Experimental-Numerical Analysis of Plastic Zones Initiation Around Holes in Shields Made of Steel C45 Under Tension. *Archive of Mechanical Engineering LXI*, nr 1, 179-198.
- Burns, T.J., 1994. A simple criterion for the onset of discontinuous plastic deformation in metals at very low temperatures. *Journal of the Mechanics and Physics of Solids* 42, 797-811.
- Cáceres, C.H., Rodriguez, A.H., 1987. Acoustic emission and deformation bands in Al-2.5% Mg and Cu-30% Zn. *Acta Metallurgica* 35, 2851-2864.
- Chihab, K., Estrin, Y., Kubin, L.P., Vergnol, J., 1987. The kinetics of the Portevin-Le Chatelier bands in an Al-5at%Mg alloy. *Scripta Metallurgica* 21, 203-208.
- Chmelík, F., Klose, F.B., Dierke, H., Šachl, J., Neuhäuser, H., Lukáč, P., 2007. Investigating the Portevin–Le Châtelier effect in strain rate and stress rate controlled tests by the acoustic emission and laser extensometry techniques. *Materials Science and Engineering: A* 462, 53-60.
- Cottrell, A.H., Bilby, B.A., 1949. Dislocation theory of yielding and strain aging of iron. *Proc. Phys. Soc.* 62, 49–62.
- Davis, J., R., 2014. *Tensile Testing, Second Edition*. ASM International.
- Diani, J.M., Parks, D.M., 1998. Effects of strain state on the kinetics of strain-induced martensite in steels. *Journal of the Mechanics and Physics of Solids* 46, 1613-1635.

- Doghri, I., Ouaar, A., 2003. Homogenization of two-phase elasto-plastic composite materials and structures. *International Journal of Solids and Structures* 40, 1681-1712.
- Doghri, I., Tinel, L., 2005. Micromechanical modeling and computation of elasto-plastic materials reinforced with distributed-orientation fibers. *International Journal of Plasticity* 21, 1919-1940.
- Dolgin, A.M., Natsik, V.D., 1991. Criteria of Instability and Kinetics of Jumps under Unstable Low Temperature Plastic Flow. *Acta Universitatis Carolinae—Mathematica Et Physica* 32, 77-88.
- Dumoulin, S., Louche, H., Hopperstad, O.S., Børvik, T., 2010. Heat sources, energy storage and dissipation in high-strength steels: Experiments and modelling. *European Journal of Mechanics - A/Solids* 29, 461-474.
- Egner, H., Skoczeń, B., Ryś, M., 2015. Constitutive and numerical modeling of coupled dissipative phenomena in 316L stainless steel at cryogenic temperatures. *International Journal of Plasticity* 64, 113-133.
- Eshelby, J., D., 1951. The force on an elastic singularity. *Philosophical Transactions of the Royal Society of London. Series A, Mathematical and Physical Sciences* 244, 87-112.
- Estrin, Y., Kubin, L.P., 1980. Criterion for thermomechanical instability of low temperature plastic deformation. *Scripta Metallurgica* 14, 1359-1364.
- Estrin, Y., Tangri, K., 1981. Thermal mechanism of the anomalous temperature dependence of the flow stress. *Scripta Metallurgica* 15, 1323-1328.
- Ferreira, P.J., Vander Sande, J.B., Fortes, M.A., Kyrolainen, A., 2004. Microstructure development during high-velocity deformation. *Metallurgical and Materials Transactions A* 35, 3091-3101.
- Fischer, F.D., 1990. A micromechanical model for transformation plasticity in steels. *Acta Metallurgica et Materialia* 38, 1535-1546.
- Fischer, F.D., Oberaigner, E.R., Tanaka, K., Nishimura, F., 1998. Transformation induced plasticity revised an updated formulation. *International Journal of Solids and Structures* 35, 2209-2227.
- Fisher, J.C., Rogers, H.C., 1956. Propagation of Lüder's bands in steel wires. *Acta Metallurgica* 4, 180-185.
- Fujii, H., Ohmiya, S., Shibata, K., Ogata, T., 2006. Effect of specimen diameter on tensile properties of austenitic stainless steels in liquid hydrogen and gaseous helium at 20K, in: Engineering, A.i.C. (Ed.), *International Cryogenic Materials Conference*.
- Fujita, H., Katayama, T., 1992. In-situ observation of strain-induced gamma-epsilon-alpha prime and gamma-alpha prime martensitic transformation in Fe-Cr-Ni alloys. *Mater Trans JIM* 243-252.
- Fujita, H., Miyazaki, S., 1978. Lüders deformation in polycrystalline iron. *Acta Metallurgica* 26, 1273-1281.
- Galindo-Nava, E.I., Rivera-Díaz-del-Castillo, P.E.J., 2017. Understanding martensite and twin formation in austenitic steels: A model describing TRIP and TWIP effects. *Acta Materialia* 128, 120-134.
- Garion, C., 2003. Material and structural mechanical modelling and reliability of thin-walled bellows at cryogenic temperatures. Application to LHC compensation system. PhD Thesis, 156.
- Garion, C., Skoczen, B., 2002. Modeling of Plastic Strain-Induced Martensitic Transformation for Cryogenic Applications. *Journal of Applied Mechanics* 69, 755-762.
- Garion, C., Skoczen, B., 2003. Combined Model of Strain-Induced Phase Transformation and Orthotropic Damage in Ductile Materials at Cryogenic Temperatures. *International Journal of Damage Mechanics* 12, 331-356.
- Garion, C., Skoczeń, B., Sgobba, S., 2006. Constitutive modelling and identification of parameters of the plastic strain-induced martensitic transformation in 316L stainless steel at cryogenic temperatures. *International Journal of Plasticity* 22, 1234-1264.
- Grosse, M., Niffenegger, M., Kalkhof, D., 2001. Monitoring of low-cycle fatigue degradation in X6CrNiTi18-10 austenitic steel. *Journal of Nuclear Materials* 296, 305-311.
- Guan, Y., Chen, B., Zou, J., Britton, T.B., Jiang, J., Dunne, F.P.E., 2017. Crystal plasticity modelling and HR-DIC measurement of slip activation and strain localization in single and oligo-crystal Ni alloys under fatigue. *International Journal of Plasticity* 88, 70-88.
- Hall, E.O., 1951. The deformation and aging of mild steel: II. Characteristics of the Lüders deformation. III. Discussion of results. *Proc. Phys. Soc. B* 64, 742-753.
- Han, H.N., Lee, C.G., Oh, C.-S., Lee, T.-H., Kim, S.-J., 2004. A model for deformation behavior and mechanically induced martensitic transformation of metastable austenitic steel. *Acta Materialia* 52, 5203-5214.
- Hecker, S.S., Stout, M.G., Staudhammer, K.P., Smith, J.L., 1982. Effects of Strain State and Strain Rate on Deformation-Induced Transformation in 304 Stainless Steel: Part I. Magnetic Measurements and Mechanical Behavior. *Metallurgical Transactions A* 13, 619-626.
- Hill, R., 1950. *The Mathematical theory of plasticity*, by R. Hill. The Clarendon Press, Oxford.
- Hu, Q., Zhang, Q., Cao, P., Fu, S., 2012. Thermal analyses and simulations of the type A and type B Portevin–Le Chatelier effects in an Al–Mg alloy. *Acta Materialia* 60, 1647-1657.

- Hull, D., Bacon, D.J., 2011a. Chapter 5 - Dislocations in Face-centered Cubic Metals, Introduction to Dislocations (Fifth Edition). Butterworth-Heinemann, Oxford, pp. 85-107.
- Hull, D., Bacon, D.J., 2011b. Chapter 9 - Dislocation Arrays and Crystal Boundaries, Introduction to Dislocations (Fifth Edition). Butterworth-Heinemann, Oxford, pp. 171-204.
- Iricibar, R., Mazza, J., Cabo, A., 1977. On the Lüders band front in mild steel—I. *Acta Metallurgica* 25, 1163-1168.
- Ishikawa, K., Yuri, T., Umezawa, O., Nagai, K., Ogata, T., 1993. Fatigue testing and properties of structural materials at cryogenic temperatures. *Fusion Engineering and Design* 20, 429-435.
- Iwamoto, T., Tsuta, T., Tomita, Y., 1998. Investigation on deformation mode dependence of strain-induced martensitic transformation in trip steels and modelling of transformation kinetics. *International Journal of Mechanical Sciences* 40, 173-182.
- Jiang, H., Zhang, Q., Jiang, Z., Wu, X., 2007. Experimental investigations on kinetics of Portevin–Le Chatelier effect in Al–4 wt.%Cu alloys. *Journal of Alloys and Compounds* 428, 151-156.
- Jiang, J., Yang, J., Zhang, T., Dunne, F.P.E., Britton, T.B., 2015. On the mechanistic basis of fatigue crack nucleation in Ni superalloy containing inclusions using high resolution electron backscatter diffraction. *Acta Materialia* 97, 367-379.
- Jiang, J., Yang, J., Zhang, T., Zou, J., Wang, Y., Dunne, F.P.E., Britton, T.B., 2016. Microstructurally sensitive crack nucleation around inclusions in powder metallurgy nickel-based superalloys. *Acta Materialia* 117, 333-344.
- Komnik, S.N., Demirsky, V.V., Startsev, V.I., 1985. Low temperature instability of plastic flow of alloys. *Czechoslovak Journal of Physics B* 35, 230-234.
- Kosevič, A.d.M., Krukowski, S., Paszkiewicz, T., 2000. *Mechanika fizyczna nieidealnych krystalicznych ciał stałych*. Wydawnictwo Uniwersytetu Wrocławskiego, Wrocław.
- Kubin, L.P., Chihab, K., Estrin, Y., 1988. The rate dependence of the Portevin-Le Chatelier effect. *Acta Metallurgica* 36, 2707-2718.
- Labergere, C., Guelorget, B., Francois, M., 2014. Strain rate distribution and localization band width evolution during tensile test. *International Journal of Solids and Structures* 51, 3944-3961.
- Lebyodkin, M., Dunin-Barkovskii, L., Bréchet, Y., Kubin, L., Estrin, Y., 1997. Kinetics and statistics of jerky flow: experiments and computer simulations. *Materials Science and Engineering: A* 234–236, 115-118.
- Lloyd, D.J., Morris, L.R., 1977. Lüders band deformation in a fine grained aluminium alloy. *Acta Metallurgica* 25, 857-861.
- Louche, H., Chrysochoos, A., 2001. Thermal and dissipative effects accompanying Lüders band propagation. *Materials Science and Engineering: A* 307, 15-22.
- Louche, H., Vacher, P., Arrieux, R., 2005. Thermal observations associated with the Portevin–Le Chatelier effect in an Al–Mg alloy. *Materials Science and Engineering: A* 404, 188-196.
- Mangonon, P.L., Thomas, G., 1970. The martensite phases in 304 stainless steel. *Metallurgical Transactions* 1, 1577-1586.
- Marcinek, D., 2009. Experimental study of discontinuous plastic flow, phase transformation and micro-damage evolution in ductile materials at cryogenic temperatures, MSc Thesis. Cracow University of Technology.
- Marcinek, D., 2016. Model of discontinuous plastic flow at temperature close to absolute zero, PhD Thesis. Cracow University of Technology.
- Marquardt, E.D., Le, J.P., Radebaugh, R., 2000. Cryogenic material properties database, the 11th International Cryocooler Conference, Keystone, Co.
- Mecking, H., Kocks, U.F., 1981. Kinetics of flow and strain-hardening. *Acta Metallurgica* 29, 1865-1875.
- Moon, D.W., 1971. Considerations on the present state of Lüders band studies. *Materials Science and Engineering* 8, 235-243.
- Mori, T., Tanaka, K., 1973. Average stress in matrix and average elastic energy of materials with misfitting inclusions. *Acta Metallurgica* 21, 571-574.
- Murr, L.E., Staudhammer, K.P., Hecker, S.S., 1982. Effects of Strain State and Strain Rate on Deformation-Induced Transformation in 304 Stainless Steel: Part II. Microstructural Study. *Metallurgical Transactions A* 13, 627-635.
- Narutani, T., Olson, G.B., Cohen, M., 1982. Constitutive flow relations for austenitic steels during strain-induced martensitic transformation. *Journal de Physique* 43.
- Nielsen, K.L., Pardo, T., Tvergaard, V., de Meester, B., Simar, A., 2010. Modelling of plastic flow localisation and damage development in friction stir welded 6005A aluminium alloy using physics based strain hardening law. *International Journal of Solids and Structures* 47, 2359-2370.
- Obst, B., Nyilas, A., 1991. Experimental evidence on the dislocation mechanism of serrated yielding in f.c.c. metals and alloys at low temperatures. *Materials Science and Engineering: A* 137, 141-150.

- Obst, B., Nyilas, A., 1998. Time-resolved flow stress behavior of structural materials at low temperatures. *Advances in Cryogenic Engineering*, Plenum Press, New York 44, 331-338.
- Ogata, T., Ishikawa, K., Umezawa, O., 1990. Low temperature creep behavior of stainless steels. *Adv. Cryogenic Engineering* 36.
- Ogata, T., Nagai, K., Ishikawa, K., 1994. Vamas tests of structural materials at liquid helium temperature. *Advances in Cryogenic Engineering*, Plenum Press, New York 40, 1191-1198.
- Olson, G.B., Cohen, M., 1972. A mechanism for the strain-induced nucleation of martensitic transformations. *Journal of the Less Common Metals* 28, 107-118.
- Olson, G.B., Cohen, M., 1975. Kinetics of strain-induced martensitic nucleation. *Metallurgical Transactions A* 6, 791.
- Ortwein, R., 2015. Constitutive model of graded micro-structure obtained via strain induced phase transformation. PhD Thesis, 363.
- Ortwein, R., Ryś, M., Skoczeń, B., 2016. Damage evolution in a stainless steel bar undergoing phase transformation under torsion at cryogenic temperatures. *International Journal of Damage Mechanics* 25, 967-1016.
- Patel, J.R., Cohen, M., 1953. Criterion for the action of applied stress in the martensitic transformation. *Acta Metallurgica* 1, 531-538.
- Petit, J., Montay, G., François, M., 2014. Strain rate measurements by speckle interferometry for necking investigation in stainless steel. *International Journal of Solids and Structures* 51, 540-550.
- Pustovalov, V.V., 2008. Serrated deformation of metals and alloys at low temperatures (Review). *Low Temperature Physics* 34, 683-723.
- Reed, R.P., McCowan, C.N., Walsh, R.P., Delgado, L.A., McColskey, J.D., 1988. Tensile strength and ductility of indium. *Materials Science and Engineering: A* 102, 227-236.
- Reed, R.P., Mikesell, R.P., 1967. Low-temperature (295 to 4 K) mechanical properties of selected copper alloys. *Journal of Materials* 2, 373-374.
- Reed, R.P., Simon, N.J., Walsh, R.P., 1991. Creep of copper: 4–300 K. *Materials Science and Engineering: A* 147, 23-32.
- Reed, R.P., Walsh, R.P., 1988. Tensile strain rate effect in liquid helium. *Adv. Cryogenic Engineering Materials* 34, 199-208.
- Roth, I., Kübbeler, M., Krupp, U., Christ, H.J., Fritzen, C.P., 2010. Crack initiation and short crack growth in metastable austenitic stainless steel in the high cycle fatigue regime. *Procedia Engineering* 2, 941-948.
- Seeger, A., 1957. *Dislocations and mechanical properties of crystals*. Wiley, New York.
- Shibata, K., 1988. Discussion about Basinski's model for serration at very low temperatures *Cryogenic Materials* 88, 865-872.
- Shibata, K., Ogata, T., Yuri, T., 2006. Effect of martensitic transformation on serration of 304L steel at cryogenic temperature. *Advances in Cryogenic Engineering: Transaction of the International Cryogenic Materials Conference* 52.
- Shin, H.C., Ha, T.K., Chang, Y.W., 2001. Kinetics of deformation induced martensitic transformation in a 304 stainless steel. *Scripta Materialia* 45, 823-829.
- Shrinivas, V., Varma, S.K., Murr, L.E., 1995. Deformation-induced martensitic characteristics in 304 and 316 stainless steels during room-temperature rolling. *Metallurgical and Materials Transactions A* 26, 661-671.
- Sitko, M., Skoczeń, B., 2012. Effect of  $\gamma$ - $\alpha'$  phase transformation on plastic adaptation to cyclic loads at cryogenic temperatures. *International Journal of Solids and Structures* 49, 613-634.
- Sitko, M., Skoczeń, B., Wróblewski, A., 2010. FCC–BCC phase transformation in rectangular beams subjected to plastic straining at cryogenic temperatures. *International Journal of Mechanical Sciences* 52, 993-1007.
- Skoczeń, B., 2004. *Compensation systems for low temperature application*. Springer-Verlag, Berlin.
- Skoczeń, B., 2007. Functionally graded structural members obtained via the low temperature strain induced phase transformation. *International Journal of Solids and Structures* 44, 5182-5207.
- Skoczeń, B., 2008. Constitutive model of plastic strain induced phenomena at cryogenic temperatures.
- Skoczeń, B., Bielski, J., Sgobba, S., Marcinek, D., 2010. Constitutive model of discontinuous plastic flow at cryogenic temperatures. *International Journal of Plasticity* 26, 1659-1679.
- Skoczeń, B., Bielski, J., Tabin, J., 2014. Multiaxial constitutive model of discontinuous plastic flow at cryogenic temperatures. *International Journal of Plasticity* 55, 198-218.
- Staudhammer, K.P., Murr, L.E., Hecker, S.S., 1983. Nucleation and evolution of strain-induced martensitic (b.c.c.) embryos and substructure in stainless steel: A transmission electron microscope study. *Acta Metallurgica* 31, 267-274.

- Stringfellow, R.G., Parks, D.M., Olson, G.B., 1992. A constitutive model for transformation plasticity accompanying strain-induced martensitic transformations in metastable austenitic steels. *Acta Metallurgica et Materialia* 40, 1703-1716.
- Suzuki, K., Fukakura, J., Kashiwaya, H., 1988. Cryogenic Fatigue Properties of 304L and 316L Stainless Steels Compared to Mechanical Strength and Increasing Magnetic Permeability.
- Suzuki, T., Kojima, H., Suzuki, K., Hashimoto, T., Ichihara, M., 1977. An experimental study of the martensite nucleation and growth in 18/8 stainless steel. *Acta Metallurgica* 25, 1151-1162.
- Sylwestrowicz, W., Hall, E.O., 1951. The deformation and aging of mild steel. *Proc. Phys. Soc. B* 64, 495– 502.
- Tabin, J., Prącik, M., 2015. Methods for identifying dynamic parameters of clip-on extensometer–specimen structure in tensile tests. *Measurement* 63, 176-186.
- Tabin, J., Skoczen, B., Bielski, J., 2016. Strain localization during discontinuous plastic flow at extremely low temperatures. *International Journal of Solids and Structures* 97–98, 593-612.
- Tabin, J., Skoczen, B., Bielski, J., 2017. Damage affected discontinuous plastic flow (DPF). *Mechanics of Materials* 110, 44-58.
- Tabin, J., Skoczeń, B., Bielski, J., 2015. Strain localization during discontinuous plastic flow at extremely low temperatures IJP.
- Talonen, J., 2007. Effect of strain-induced  $\alpha'$ -martensite transformation on mechanical properties of metastable austenitic stainless steels. Phd Thesis, 127.
- Taylor, G., I., 1938. Plastic Strain in Metals. *Journal of the Institute of Metals* 62, 307-324.
- Tichonow, A.N., Samarski, A.A., 1963. *Równania fizyki matematycznej*, Państwowe wydawnictwo Naukowe-PWN, Warszawa, 765.
- Tomita, Y., Iwamoto, T., 2001. Computational prediction of deformation behavior of TRIP steels under cyclic loading. *International Journal of Mechanical Sciences* 43, 2017-2034.
- Umezawa, O., Ogata, T., Yuri, T., Nagai, K., Ishikawa, K., 1994. Review of high cycle fatigue properties of structural materials at cryogenic temperatures. *Advances in Cryogenic Engineering*, Plenum Press, New York 40, 1231-1238.
- Venables, J.A., 1964. The nucleation and propagation of deformation twins. *Journal of Physics and Chemistry of Solids* 25, 693-700.
- Verel, D.J., Sleswyk, A.W., 1973. Lüders band propagation at low velocities. *Acta Metallurgica* 21, 1087-1098.
- Vinogradov, A., Lazarev, A., 2012. Continuous acoustic emission during intermittent plastic flow in  $\alpha$ -brass. *Scripta Materialia* 66, 745-748.
- Wayman, C.M., Bhadeshia, H.K.D.H., 1996. Chapter 16 - Phase Transformations, Nondiffusive A2 - Cahn, Robert W, in: Haasen†, P. (Ed.), *Physical Metallurgy* (Fourth, Revised and Enhanced Edition). North-Holland, Oxford, pp. 1507-1554.
- Wessel, E.T., 1957. Metals at Low Temperatures. *Trans. ASM* 49, 149.
- Zaiser, M., Hähner, P., 1997. Oscillatory Modes of Plastic Deformation: Theoretical Concepts. *physica status solidi* (b) 199, 267-330.
- Zhang, J., Jiang, Y., 2005. Lüders bands propagation of 1045 steel under multiaxial stress state. *International Journal of Plasticity* 21, 651-670.
- Zhang, Q., Jiang, Z., Jiang, H., Chen, Z., Wu, X., 2005. On the propagation and pulsation of Portevin-Le Chatelier deformation bands: An experimental study with digital speckle pattern metrology. *International Journal of Plasticity* 21, 2150-2173.
- Zhang, T., Jiang, J., Shollock, B.A., Britton, T.B., Dunne, F.P.E., 2015. Slip localization and fatigue crack nucleation near a non-metallic inclusion in polycrystalline nickel-based superalloy. *Materials Science and Engineering: A* 641, 328-339.
- Ziegenbein, A., Hähner, P., Neuhäuser, H., 2001. Propagating Portevin–LeChatelier deformation bands in Cu-15 at.% Al polycrystals: experiments and theoretical description. *Materials Science and Engineering: A* 309–310, 336-339.
- Życzkowski, M., 1967. Combined loadings in the theory of plasticity. *International Journal of Non-Linear Mechanics* 2, 173-205.

